Dynamical phenomena in stratified solar coronal plasma

BENIAMIN ORZA

Submitted for the degree of Doctor of Philosophy

School of Mathematics and Statistics

August 2013

Supervisors: Dr. Istvan Ballai & Dr. Rekha Jain

University of Sheffield

Acknowledgements

I would like to thank my supervisors, Dr. Istvan Ballai and Dr. Rekha Jain for their help and support throughout my PhD. It has been a great period of my life but this wouldn't be possible without the chance to do this PhD. Chance that was given to me by Dr. Istvan and Dr. Alexandru Marcu who initiated me in solar physics, for this I'm deeply grateful to you both.

I would also like to thank the University of Sheffield, Faculty of Science for the funding provided. Without it I would not have been able to complete my PhD. Thanks goes to Professor Tony Arber for giving me access to LARE2D Lagrangian remap code for MHD simulations.

Thanks to my Sheffield friends and colleagues as they helped me throughout my time spent here making my PhD life less stressful and more fun.

Last but not the least I would like say a huge thank you to my family and to my wife for her support throughout ups and downs of my PhD life, who provided essential emotional support and whose love and enthusiasm has made this final year much easier to sail through.

Abstract

Different dynamical phenomena in the solar corona are investigated in the present Thesis. We aim to investigate using a semi-analytical approach of the effect of the surrounding environment on the period ratio of the fundamental to first harmonic of a thin coronal loop. Investigation of geometrical effects are taken into account, namely asymmetry of the coronal loop, i.e. its deviation from a semi-circular shape.

It is found that if we are to obtain more accurate estimates on the effect of the environment on the transversal oscillations of a coronal loop, we have to take into account that in reality a coronal loop depends on more than one coordinate, secondly, isothermal supposition of the loop and its environment also need refinement, as observations show that the loops are not always in hydrostatic equilibrium. The study on the expansion of a coronal loop indicates that in order to have more realistic results one would need to include damping processes, resonant absorption and cooling processes. Further in an expanding loop, the growth of the amplitude due to emergence and decay of amplitude due to resonant damping or cooling will be competing processes. When it expands, a loop can also have accelerated motion upwards in the corona with cross section modification of the flux tube.

The final piece of work in this thesis is a numerical investigation into a 2D magnetic reconnection process, where we study reconnection rates and how different parameters such as resistivity and Hall term affect the process of field line reconnection. The Hall effect does speed up the reconnection process, but it depends significantly on the initial conditions of the problem. These initial conditions, i.e. different magnetic field configuration, density stratification, gravity play an important role in the reconnection process.

Contents

List of Figures

List of Figures

Chapter 1

Introduction

1.1 Our Sun

Our Sun was formed around 4.5 billion years ago in a cloud of interstellar gas that slowly collapsed under its own gravity rotating faster and faster until the cloud shrunk into a flat disc with a very hot core where, through thermonuclear processes over a few million years, a heated star began to shine. Our Sun is an ordinary GeV-type star estimated to live for an extra 5 billion years.

In the last twenty years we have seen exciting insight into our Sun. High resolution ground-based instruments and space satellites such as the Transition Region and Coronal Explorer (TRACE), Solar and Heliospheric Observatory (SOHO), Hinode and Solar Dynamic Observatory (SDO) have revealed a highly complex and dynamic nature of our star. Traditionally, the Sun is structured in two main parts: inner layers (core, radiative zone, tachocline, convective zone) and outer layers (photosphere, chromosphere, transition layer, corona, solar wind) as shown in Figure 1.1.

The dynamical and thermal state as well as the stability of outer atmosphere is driven and controlled by the magnetic field which is generated in the solar interior by the dynamo effect. Magnetic fields in the solar atmosphere can form distinctive features with varied dimensions from a few kilometers to hundreds of Megameters with intensities varying from a few gauss (G) in the quiet Sun to kilogauss (kG) in sunspots.

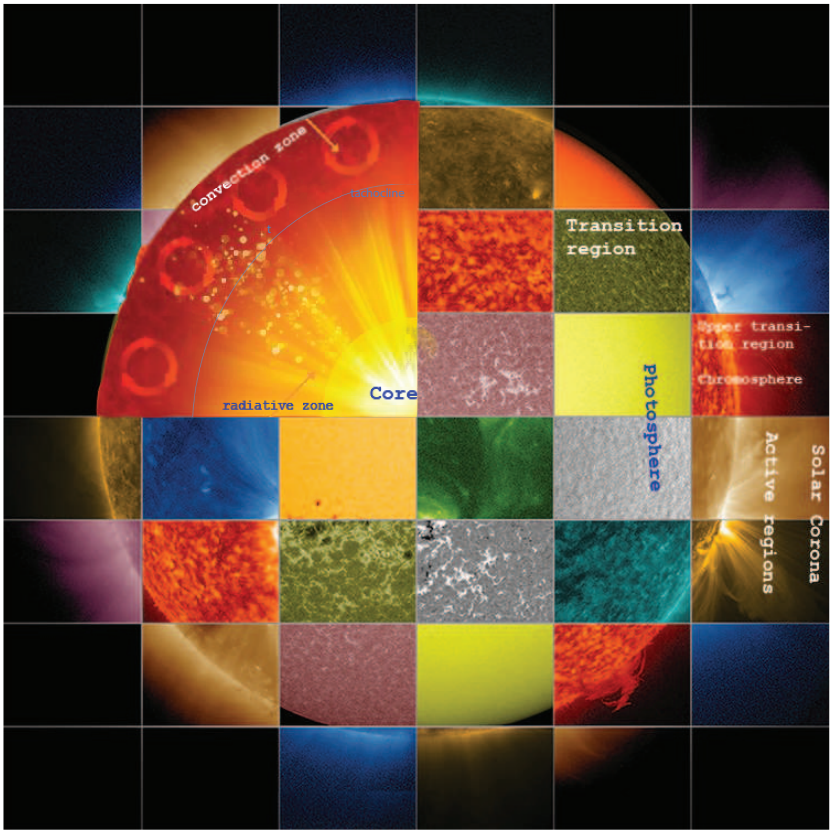

Figure 1.1: A composite image of the solar structure highlighting the solar exterior: photosphere, transition region, chromosphere, solar corona and solar interior: core, radiative zone, tahocline, convective zone (background image credits to NASA (SDO))

1.1.1 The Solar interior

The Solar interior is separated in four regions according to the dominant processes that occur here. The core generates through nuclear fusion 99% of the Sun's energy. In the solar core the temperatures reach $14 - 15$ million Kelvin (K) and densities are of the order of 1.6×10^6 kg m^{-3}, 10 times the density of gold.

The radiative zone is characterized by the energy being transported by radiation. Energy produced in the core is carried by photons that bounce from particle to particle through the radiative zone through ionisation/recombination processes. A photon will take around 10^7 years to reach the surface. Density

will drop from 2×10^4 kg m^{-3} (approx. density of gold) to only 0.2×10^4 kg m^{-3} (close to water density) from 0.25 to 0.75 solar radia.

Just above the radiative zone is the tachocline region where Sun's magnetic field is believed to be generated by a magnetic dynamo. The convection zone extends from a depth of 2×10^4 km up to the visible surface. Temperatures in this region decrease from 2 MK to 6000 K. The plasma in this layer is more opaque due to heavy ions (carbon, nitrogen, calcium, iron, oxygen) holding onto their electrons. Hence the heat is trapped here making the fluid unstable and convective. Convection will occur when the temperature gradient becomes larger than the adiabatic gradient or ratio of specific heats, i.e. the ratio of the heat capacity at constant pressure to heat capacity at constant volume. This convective motion will carry heat rapidly to the surface expanding the fluid as it rises. At the surface these convective cells are visible and called granules and supergranules with typical diameters of 10^3 km to 3×10^4 km, respectively.

1.1.2 The Solar exterior

At the top of the convection zone lies a dense and thin (500 km) layer of plasma, the photosphere. The temperature in this region decreases with height from 6000 K at the base of this layer to a minimum of 4300 K near the chromosphere. The magnetic field is not dispersed uniformly, instead it tends to accumulate in entities known as flux tubes. The process of emergence of flux tubes is believed to be caused by massive convective motions and instabilities below photosphere. In this region one of the most obvious magnetic features is the sunspot (dark cool region) with strong magnetic field strengths ($\sim$ 3 kG), with typical diameters of 10^4 km and an average temperature of 4000 K. These entities are not homogeneous and exhibit an irregular pattern of bright points (umbral dots). More details can be found in the reviews of umbral fine structure by, e.g Bray and Loughhead (1964), Parker (1979), Knobloch and Weiss (1984), Grossmann-Doerth et al. (1986), Garcia de la Rosa (1987), Weiss et al. (1990, 2002), Lites et al (1991), Solanki (2003), Sobotka (2006) and Bharti (2007). In addition to sunspots the rest of the photosphere is far from being homogeneous, magnetic field is concentrated in structures ranging from small flux tubes ($\approx$ 100 km, 1 kG) to knots and pores (500-1000 km, 1-2kG).

Above the photosphere, the pressure and density begin to decrease while the temperature increases to approximate 5×10^4 K. Emission at chromospheric region temperatures reveals the existence of numerous spatial inhomogeneities along the solar limb, named spicules. These features were discovered first by Secchi (1877). Spicules are seen in strong chromospheric lines as columns of gas protruding out of the solar limb with a typical height of 10^4 km and width of 10^3 km (see e.g. Roberts 1945). The base of spicules lies above the photosphere and so, their roots are apparently seen disconnected from the solar surface (see, e.g. Lorrain and Koutchmy 1996). These features consist of chromospheric plasma (relatively cool plasma with typical temperature of $\sim 10^4$ K) which is ejected upwards towards the corona. The material is accelerated in less than 30 seconds over the first 10^3 km to a speed of $\sim$ 25 km s^{-1}. Afterwards, ejected plasma is slowed down, reaching its maximum height in about 5 min (see, e.g. Wilhem 2000). From this point on, material either falls back towards the chromosphere

or disappears from the visible part of the spectra. The life time average of these features is 5-10 min. There are variations in these observed velocities along spicules which occur almost instantaneously within their volume (see, e.g. Beckers 1972). Spicules are not necessarily straight or vertical. In most cases, they are associated with magnetic elements (fibrils and threads) of the chromospheric network, and tend to cluster in either 'bushes' (Pikel′ner 1969), or 'rosettes' (Uchida 1969). They also exhibit very irregular shapes near the edges of coronal hole (see, e.g. Wilhelm 2000). With regard to the relevant physical interpretation, it is thought that the spicules are formed by the interaction of the plasma with the strongly concentrated magnetic fields at the granular boundaries, however, there is still no satisfactory theoretical models of spicule formation (see Porter et al. 1987, Ballegooijen & Nilsen 1999, Wilhem 2000, Takeuchi & Shibata 2001, De Pontieu & Erdélyi, 2006, Zaqarashvili, 2009 for reviews).

Above chromosphere, in the very thin transition region the density drops to around 10^{-10} kg m^{-3} and the temperature rises very fast to 10^6K. Long lasting upflows were observed in the upper transition region (see, e.g. De Pontieu et al. 2009, Tian et al. 2009), which is a direct signature of mass supply to coronal loops that extend to solar corona.

Finally, the solar corona is the extended region characterized by a myriad of open and closed magnetic structures with temperatures in excess of 10^6 K. One of the most intriguing problems of solar physics is the existence and maintenance of very high temperature in the corona. It is widely recognized that the heating of this important solar layer is of magnetic nature, regions of high emissivity in Extreme Ultraviolet (EUV) are associated with considerable accumulations of magnetic fields in the lower regions of the atmosphere.

The solar corona exhibits a variety of magnetic features such as loops, plumes, coronal holes, coronal mass ejections (CMEs) and others. Using high-resolution satellites (e.g. SOHO, TRACE, Hinode, SDO) solar physicists identified several manifestations of the coronal magnetic field from small patches covering the entire Sun to bright and large magnetic field loops in active regions. More active magnetic regions appear during periods of solar maxima and almost disappear when the cycle goes towards solar minima. Coronal loops

populate both active and quiet regions of the solar surface. They can extend to heights up to $100 - 200$ Mm in length with densities of $10^{-10} - 10^{-12}$ kg m^{-3} (Vernazza et al. 1981) and temperatures 10^7 K. A coronal loop is a magnetic flux tube fixed at both ends, threading through the solar body, protruding into the solar atmosphere. They are ideal structures to observe when trying to understand the transfer of energy from the solar body through the transition region, chromosphere and into the solar corona. Coronal loops, and in general coronal magnetic structures, are the focus of extended theoretical and observational studies. Despite significant progress in coronal physics over several decades, a number of fundamental questions, for instance, what are the physical mechanisms responsible for the coronal heating, the solar wind acceleration, and solar flares, remain to be answered. All these questions, however, require detailed knowledge of physical conditions and parameters in the corona, which cannot yet be measured accurately enough. In particular, the exact value of the coronal magnetic field remains unknown, because of a number of intrinsic difficulties with applications of direct methods (e.g. based upon the Zeeman splitting and gyroresonant emission), as well as indirect (e.g. based upon extrapolation of chromospheric magnetic sources). Also, the coronal transport coefficients, such as volume and shear viscosity, resistivity, and thermal conduction, which play a crucial role in coronal physics, are not measured even within an order of magnitude and are usually obtained from theoretical estimations. Other obscured parameters are the heating function and filling factors. The detection of coronal waves provides us with a new tool for the determination of the unknown parameters of the corona - Magnetohydrodinamics (MHD) seismology of the corona. Oscillations of magnetic structures were and are used as a basic ingredient in coronal seismology, where observations of wavelength, propagation speed, damping time, amplitude, etc. are corroborated with theoretical modeling (MHD) to derive different quantities that cannot be directly measured (e.g. magnetic field, heating functions, stratification parameters, etc.). Further details of research on oscillations of coronal loops and the impact of solar environment on them will be discussed in Chapter 3.

The problem of coronal heating comprises a number of sub-questions, some of them being already answered (where and how is the energy generated, how

is it transported to the corona, how it is converted into heat and how it is dissipated). One of the most viable mechanisms to convert energy is the magnetic reconnection (see Chapter 6). Through magnetic reconnection process the magnetic energy stored in magnetic field lines is converted into heat and kinetic energy, thus providing the high temperature of the corona. Large scale disturbances generated by coronal mass ejections (CMEs) and flares can interact with coronal loops as seen by many (e.g. Ramsey and Smith 1966, Eto et al. 2002, Jing et al. 2003, Okamoto et al. 2007, Isobe and Tripathi 2007, Pintér 2008), generating oscillations that exhibit periodic movement about the loop's symmetry axis (kink modes), see representation of kink oscillations in Figure 1.2.

Global waves are generated by powerful energy releases (flares/CMEs). We still do not fully understand how exactly these global waves are generated, however it is widely accepted that these disturbances are similar to the circular expanding bubble-like shocks after atomic bomb explosions. Thanks to the available observational facilities, global waves were observed in a range of wavelengths in different layers of the solar atmosphere. A pressure pulse can generate seismic waves in the solar photosphere propagating with speeds of 200 - 300 km s^{-1} (Kosovichev and Zharkova 1998; Donea et al. 2006). Higher up in the atmosphere, a flare generates very fast super-Alfvénic shock waves known as Moreton waves (Moreton and Ramsey, 1960), best seen in the wings of H_α images, propagating with speeds of 1000 - 2000 km s^{-1} . In the corona, a flare or CME can generate an Extreme-ultraviolet Imaging Telescope (EIT) wave (Thompson et al. 1999), first seen by the SOHO/EIT instrument or an X-ray wave seen in soft X-ray telescope SXT (see, e.g. Narukage et al. 2002). There is still a vigorous debate how this variety of global waves are connected (if they are, at all). Co-spatial and co-temporal investigations of various global waves have been carried out but without the final consent.

Unambiguous evidence for large-scale coronal impulses initiated during the early stage of a flare and/or CME has been provided by the EIT observations on-board SOHO and by TRACE/EUV see Figure 1.2. EIT waves propagate in the quiet Sun with speeds of 250 - 400 km s^{-1} at an almost constant altitude. At a later stage in their propagation EIT waves can be considered as a freely

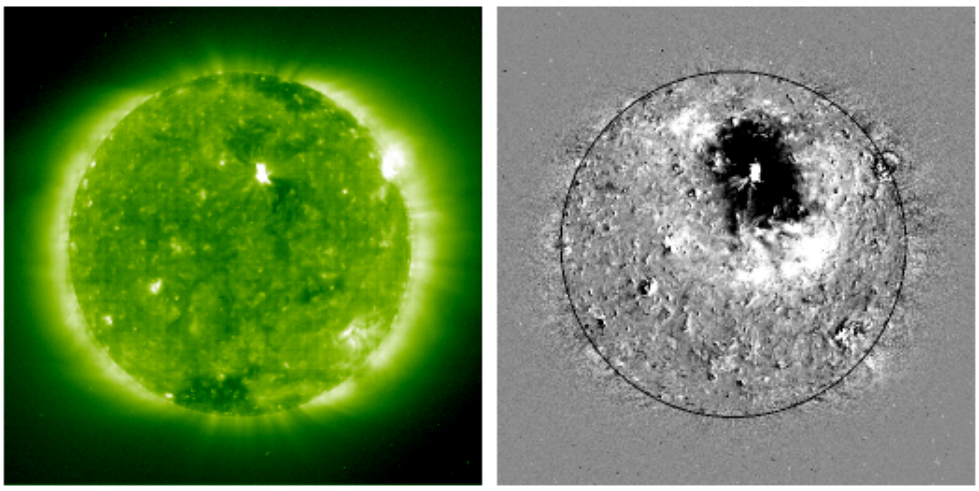

Figure 1.2: Left: SOHO/EIT 195 image of the Sun on 12 May 1997 at 05:24 0 UT. Right: SOHO/EIT image at 05:07 UT with the pre-event image at 04:34 UT digitally subtracted from it. White (black) regions denote increase (decrease) in emission. The dark regions near the active region visible in both images are darkened regions associated with a coronal mass ejection. The bright circular ring of emission outside the darkened regions in the right image corresponds to an increase in emission propagating at 250 km s^{-1}.

propagating wavefront which is observed to interact with coronal loops (see, e.g. Wills-Davey and Thompson 1999). Using TRACE/EUV, Ballai et al. (2005) have shown that EIT waves (seen in this wavelength) are waves with average periods of the order of 400 s. Since at this height, the magnetic field in the quiet Sun can be considered vertical, EIT waves were interpreted as fast MHD waves. This conclusion is further supported by other observations (see, e.g. Long et al. 2008, Patsourakos et al. 2009).

1.2 Main features in the solar corona

1.2.1 Coronal loop oscillations

Our knowledge about the dynamics of the solar atmosphere was shaped to a large extent by the observational results provided by the high-resolution satellites of the last two decades (SOHO, TRACE, Hinode, STEREO and later SDO).

Energy releases in the solar atmosphere are known to generate large scale global waves that propagate over long distances (see, e.g. Moreton and Ramsey 1960, Uchida 1970, Thompson et al. 1999, Ballai et al. 2005) and can interact with magnetic structures such as coronal loops, prominence fibrils as observed by e.g. Eto et al. (2002), Jing et al. (2003), Isobe and Tripathi (2007), Pintér et al. (2008), etc. The energy stored in these global waves can be released by dissipative mechanisms or can be transferred to coronal loops generating periodic movement about the symmetry axis, i.e. kink oscillations (see e.g. Wills-Davey and Thompson 1999, Ballai et al. 2005, Jess et al. 2008). Hasan et al. (2003) argued that horizontal motion of magnetic elements in the

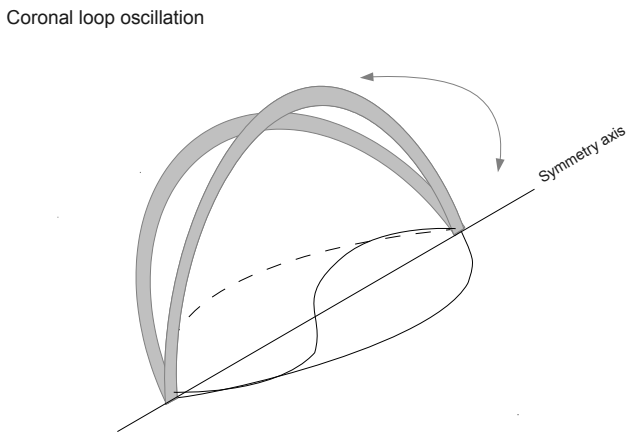

Figure 1.3: Periodic movement about the loop's symmetry axis, first two modes i.e. kink modes

photosphere can generate enough energy to heat the magnetized chromosphere. They found, based on numerical modeling, that granular buffeting generates kink oscillations and, through mode coupling, longitudinal oscillations. This

was confirmed by Musielak and Ulmschneider (2003b). From the observational point-of-view, Volkmer et al. (1995), using high spatial and temporal resolution spectropolarimetric data, detected short-period longitudinal waves (P $\sim$ 100 s) in small magnetic elements in the solar photosphere and estimated the energy flux they carried to be sufficient for the heating of the bright structures observed in the chromospheric network. Martínez González et al. (2011) have found, using SUNRISE/IMaX data, magnetic flux density oscillations in internetwork magnetic elements, which they interpreted to be due to granular forcing.

Recent CoMP observations (Tomczyk et al. 2007) showed that the predominant motion of coronal loops is the transverse kink oscillation and that this is the easiest to generate. Based on Hinode data, Ofman and Wang (2008) showed the first evidence on transverse waves in coronal multi-threaded loops with cool plasma ejected from chromosphere flowing along the threads. STEREO data was used to determine the 3-D geometry of the loop (see, e.g. Verwichte et al. 2009) and SDO/AIA was used to prove coupling of the kink mode and cross-sectional oscillations explained as a consequence for the loop length variation in the vertically polarized mode (see e.g. Aschwanden and Schrijver 2011).

The first theoretical models used to describe a coronal loop considered a straight homogeneous magnetic cylinder where the magnetic field lines are considered frozen in a dense photospheric plasma. Since then, considerable advances were made in representing a coronal loop (see, e.g. Roberts et al. 1984, Nakariakov et al. 1999, Nakariakov et al. 2001, Ruderman and Roberts 2002, Andries et al. 2995,2009, Ballai et al. 2005, 2011, Verth et al. 2007, 2008, Ruderman et al. 2008, Van Doorsselaere et al. 2008, Morton and Erdélyi 2009, Ruderman and Erdélyi 2009, Morton and Ruderman 2011). The dispersion relations for plasma waves under the assumptions of ideal magnetohydrodynamics (MHD) were derived long before EUV observations (see, e.g. Edwin and Roberts 1983, Roberts et al. 1984).

The realistic interpretation of many observations is often made difficult by the poor spatial and temporal resolution of present satellites. Even so, considerable amount of direct and indirect information about dynamical and thermodynamical state of plasma, and the structure of coronal magnetic field, can still be obtained.

1.2

The waves and oscillations in the solar atmosphere are strongly influenced by magnetic fields. Waves are generated, in general, by buoyancy forces (gravity, magnetic field, pressure gradients, etc.) but also due to the convection motion in the sub-surface region and due to energetic phenomena occurring at different heights in the solar atmosphere. Depending on interaction with the magnetic structure we can distinguish between local and global waves. Even though they may seem separate phenomena, they are very much related in the sense that often global waves can generate local waves and oscillations.

Given the complex structure of coronal loops it is expected that these magnetic entities will support a rich variety of waves and oscillations. Pure magnetic waves (Alvén waves) are transversal waves which propagate along magnetic field lines and are very little influenced by non-ideal effects such as ohmic resistivity and Hall effect. The second class is magnetoacoustic waves and they are the most studied type of waves: the so-called kink wave which propagates along a magnetic flux tube so that the symmetry axis of the tube is distorted (see, e.g. Aschwanden et al. 1999, Nakariakov et al. 1999) and sausage modes (i.e. oscillations that occur such that the symmetry axis of loops is not dislocated), observed by Aschwanden et al. (2003a), Taroyan (2008). It is believed that kink waves and oscillations are the result of the interaction between an external driver (a global wave or CME) and the coronal loop (Selwa et al. 2006, Ogrodowczyk and Murawski 2007, Hindman and Jain 2008, Ballai et al. 2009). Kink oscillations in coronal loops and their very rapid damping allowed the estimations of magnetic fields, density scale-heights, sub-resolution structure, etc. (see, e.g. Nakariakov et al. 1999, Andries et al. 2005; Verth et al. 2008).

A very powerful diagnostic of the coronal field and plasma procedure is the so-called P_1/P_2 seismology which has its roots in the realization that in an inhomogeneous medium the ratio of periods of overtones differs from their canonical values.

Within the context of coronal physics Andries et al. (2005) showed that the longitudinal stratification (i.e. along the longitudinal symmetry axis of the magnetic field) modifies the periods of kink oscillations of coronal loops (kink waves). These authors showed that the deviation of P_1/P_2 (where P_1 refers to the period of the fundamental transverse oscillation, while P_2 describes the pe-

riod of the first overtone of the same oscillation) can differ considerably from the canonical value of 2 (that would be recovered if the loops were homogeneous). They also showed that the deviation of P_1/P_2 from 2 is proportional to the degree of stratification. This problem was also discussed in other studies such as Dymova and Ruderman (2006), Diaz et al. (2007), McEwan et al. (2008), Ballai et al. (2011). Recently Ballai et al. (2011) discussed the ambiguity of the period ratio seismology, as some other effects could result in the observation of multiple periods and each interpretation results in different value for the magnetic field and degree of stratification. The period ratio other than 2 was already observed in coronal loops by, e.g. Verwichte et al. (2004), De Moortel and Brady (2007), Pintér et al. (2008), Van Doorsselaere et al. (2009).

Jain and Hindman (2012) found that direct sensitivity of its eigenfrequencies to density is rather weak. They proved that through the waves speed, we can determine the mode frequencies. Due to the fact that individual coronal loops with identical speed but different densities are seismically indistinguishable, coronal seismology is an insufficient tool for differentiating between coronal loops with the same magnetic field strengths, densities and kink speed but with different flaring rates. Combined with independent observations of loop properties e.g. temperature and field strength, MHD seismology can be used to constrain density. Jain and Hindman (2012) pointed out that from the measurement of only two frequencies, one deduce more than two broad spatial averages of the kink speed along the loop (around apex and footpoints).

1.2.2 Alternative mechanisms for loop oscillations

The idea that a coronal loop is twisted and then carries an electric current gave rise to several alternative mechanisms for the loop oscillations. An inductance, capacitance, resistance (LRC)-circuit model developed by Zaitsev et al. (1998) explains the loop oscillations in terms of eigen-oscillations of an equivalent electric circuit, where the current is associated with the loop twist. As one of the physical quantities perturbed by this effect is the current (or the twist), its periodic pulsations would be observed through the direct modulation of the gyrosynchrotron emission by the period change of the angle between the line of

sight (LOS) and the magnetic field in the emitting region. They also showed that the periodic twist is accompanied by perturbations of density, the oscillations would modulate thermal emission as well. The decay of oscillations is normally estimated by this model to be very small. Khodachenko et al. (2003) applied the idea of inductive interaction of electric currents in a group of neighbouring loops to an alternative interpretation of kink oscillations, suggesting that they are caused by the ponderomotoric interaction of currents in groups of inductively coupled current-carrying loops. More specifically, the ponderomotoric interaction of current-carrying magnetic loops can lead to the oscillatory change of the loops inclination. The efficiency of coupling, the period of oscillations and the decay time are connected with mutual inductance of different loops in the active region analysed. It was pointed out that the interaction of the oscillating loop with neighbouring loops can lead to strong damping of the oscillations.

1.2.3 Magnetic reconnection

One of the questions still left to answer is coronal heating: how does the temperature increase as you go further up in the solar atmosphere?. As we previously discussed the coronal loop oscillations can occur due to the fact that EIT waves or other large scale perturbations could interact with coronal loops. These EIT waves are generated by coronal mass ejections (CMEs) and/or flares in active regions of the Sun. It is believed that the dissipation of waves in the solar corona must contribute to localised heating. In addition the field lines in active regions in opposite polarity in the presence of resistivity, may reconnect and release magnetic energy, providing another source of localised heating in the corona. We still don't have an answer to the coronal heating problem but magnetic reconnection and waves all together might give us a broader perspective, of what's really happening up there.

Magnetic reconnection is considered to be at the very core of solar flares, coronal mass ejection, and interaction of solar winds with the Earth's magnetosphere (see, e.g. Parker, 1979, Kulsrud 1998, Biskamp, 2000, Priest and Forbes, 2000). Magnetic reconnection involves a topology change of a set of field lines,

which leads to a new equilibrium configuration of lower magnetic energy.

Magnetic reconnection provides an elegant, and so far the only, explanation for the motion of chromospheric ribbons and flare loops during solar flares. At the same time, it also accounts for the enormous energy release in solar flares (see, e.g. Shibata et al 1997). To date, there are extensive numerical studies of phenomena associated with active regions (such as solar flares, X-ray jets, etc.), involving magnetic reconnection (see Ugain & Tsuda 1977, Forbes & Priest 1984; Yokoyama & Shibata 1996; Chen et al. 1999, Forbes 2000, Birn et al. 2001, Huba, 2003 Birn and Priest, 2007, Priest and Horning 2009, Baty et al. 2009a,b, Priest and Pontin 2009,).

These models successfully predict most of the observational signatures of violent flare events found in recent X-ray observations by Hinode. Observed Doppler shifts indicate bulk motions with velocities comparable to the local Alfvén speed (see, e.g. Dere et al. 1991, Innes et al. 1997, and later Wilhelm et al. 1998) suggested that the spatial and temporal evolution of observed line profiles during solar explosive events is consistent with physical interpretation involving *bi-directional* plasma flows. Thus, magnetic reconnection has become the strongest candidate capable of explaining the observational signatures of these events.

In an ideal medium plasma elements preserve their magnetic connections, but the presence of a localised region of length ($\ll L_e$) (see Figure 1.4), where nonideal effects are important, can lead to a change of connectivity of plasma elements -i.e., to magnetic reconnection (see Figure 1.4). The reconnection may be fast or slow (as we are going to describe in the next few paragraphs), although in many astrophysical situations fast magnetic reconnection is believed to occur such as in solar flares where resistive reconnection time-scales are too slow to explain the observed energy release times.

The main effects of magnetic reconnection are: to convert some of the magnetic energy into heat by ohmic dissipation; to accelerate plasma by converting magnetic energy into bulk kinetic energy; to generate strong electric currents and electric fields, as well as shock waves and current filamentation, all of which may accelerate fast particles; to change the global connections of the field lines and so affect the paths of fast particles and heat, which are directed mainly

along the magnetic field.

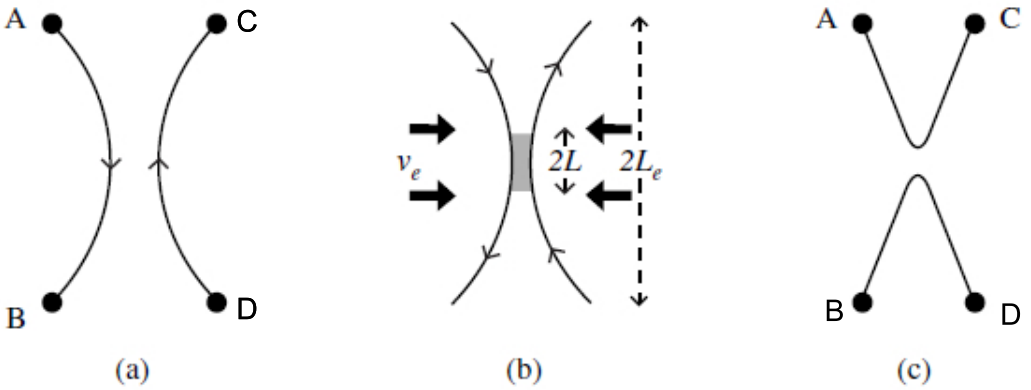

Figure 1.4: Breaking and reconnection of magnetic field lines when a localised diffusion region (shaded) leads to a change of connectivity of plasma elements (AB to AC).

In the low solar atmosphere, reconnection is generally modeled by resistive MHD with classical ohmic dissipation. However, in the outer corona, Hall MHD with a two-fluid approach or a kinetic model are more appropriate (see Birn and Priest, 2007).

Dungey (1953) was the first to suggest that *lines of force can be broken and rejoined* was. In 1958, Sweet presented a model of a current sheet at an X-type neutral point when two bipolar regions come together. The magnetic field squeezes out the plasma between them in a process of steady-state reconnection. Parker (1957) came up with scaling laws for the model and coined the phrase *reconnection of field lines*.

The Sweet-Parker model (Sweet 1958, Parker 1957, 1963) yields a reconnection rate (or inflow plasma speed) of $v_i = v_{Ai}/R_m^{1/2}$, proportional to the inflow Alfvén speed v_{Ai}. The magnetic Reynolds number, $R_m = Lv_{Ai}/\eta$, is based on the length L of the current sheet and resistivity parameter η. This rate of reconnection is a small fraction of the Alfvén speed if the Reynolds number is much greater than 1 and is much too slow for solar flares so that it is referred to as slow reconnection.

Furthermore, Petschek (1964) realised that slow-mode shock waves also convert magnetic energy into heat and kinetic energy and are naturally generated

by a tiny diffusion region. His (steady) mechanism (at typically 0.01-0.1 v_A) is indeed rapid enough for a flare. It possesses four standing slow-mode shock waves extending from a tiny central Sweet-Parker current sheet and is the first to discuss regimes of fast reconnection.

Petschek′s mechanism was widely accepted as the answer to fast flare energy release, especially when self-similar solutions for the external region were discovered (Soward and Priest, 1977). Numerical experiments (Biskamp, 1986) revealed solutions that are very different from Petschek′s and so, at first, they seemed to cast doubt on the validity of the Petschek mechanism. However, Priest and Forbes (1986) realised that the reason for the discrepancy, was the different boundary conditions being imposed by Biskamp. Priest and Forbes (1986), also discovered a whole family of Almost-Uniform solutions for fast reconnection, including the solutions of both Petschek and Biskamp as special cases. It is now well established that, when the magnetic diffusivity is enhanced at the X-point, Petschek′s mechanism and the other Almost-Uniform reconnection regimes can indeed occur, and that an enhancement of diffusivity is a common effect in practice. However, what happens when the magnetic diffusivity is spatially uniform is not yet clear. The suspicion from high-resolution numerical experiments (see, e.g. Baty et al. 2009a,b) is that the case of uniform diffusivity is neutrally stable such that fast reconnection is stable when the diffusion region diffusivity is enhanced and is unstable (to some, as yet unidentified, instability) when it is reduced.

Fast collisionless reconnection may be assisted by the Hall effect (Shay and Drake, 1998; Huba, 2003). Numerical studies show that the Hall term in the generalized Ohm's law may play a key role in the process of rapid magnetic reconnection. It was shown by Cowling (1975) that when the strength of the magnetic field is very large, Ohm's law must be modified to include Hall currents. The mechanism of conduction in ionized gases in the presence of strong magnetic field is different from that in metallic substance. The electric current in ionized gases is generally carried by electrons, which undergo successive collisions with other charged or neutral particles. In the ionized gases the current is not proportional to the applied potential except when the field is very weak. In an ionized gas where the density is low and the magnetic field is very strong, the

conductivity normal to the magnetic field is reduced due to the free spiraling of electrons and ions about the magnetic lines of force before suffering collisions and a current is induced in a direction normal to both electric and magnetic fields. This phenomenon, well known in the literature, is called the Hall effect.

As long as the Hall effect is taken into consideration, simulations predict enhanced reconnection rates that appear to be virtually independent of other model assumptions and the codes employed (Birn et al. 2001, 2005). Recent numerical studies focus on the dynamics and energetics of Hall MHD reconnection in various magnetic geometries (see, e.g. Bhattacharjee et al. 2005; Cassak et al. 2006; Craig & Litvinenko 2008). Analytical models can help in developing some insight into how fast reconnection occurs in weakly collisional plasmas. Of particular interest would be the interpretation of space and laboratory observations that have already revealed distinct features of Hall magnetic reconnection (Mozer et al. 2002; Ren et al. 2005). Although exact steady solutions for Hall MHD reconnection are available, they are limited to one-dimensional current sheets (Dorelli 2003; Craig & Watson 2003, 2005).

Most of the attention is now focussed on 3D reconnnection, which is completely different from 2D reconnection in ways identified by Priest et al. (2003). A landmark paper by Schindler et al. (1988) proposed a concept of General Magnetic Reconnection, in which reconnection can occur either at null points (locations where magnetic field vanishes) or in the absence of null points whenever a parallel electric field, $E_{||}$, is produced by any localised non-ideal region. The condition for reconnection to occur is simply that the integral of parallel electric field, $E_{||}$, evaluated along a magnetic field line that passes through the region of local nonidealness (integral different from value of zero): indeed, the maximum value of this integral gives the rate of reconnection.

1.3 Outline

The focus of this Thesis is to study the main features observed in the solar corona namely, how transversal oscillations are affected by temperature of the environment and differences in the coronal loop, geometrical effects (expansions of coronal loops and asymmetrical loops), and also to study 2D magnetic reconnection in a stratified plasma using this Lagrangian code Lare2D. Although these two physical phenomena seem distinct, in reality they are very much connected. A magnetic reconnection in the solar corona can generate global coronal waves that can interact with coronal loops, eventually leading to oscillations in loops.

Chapter 2 introduces a tool, for studying coronal seismology using the framework of Magnetohydrodynamics (MHD).

Chapter 3 aims to investigate the P_1/P_2 period ratio of transversal loop oscillations for the diagnostics of longitudinal structuring of coronal loops. So far, all the studies considered that the density stratification (related to scale-height) is identical inside and outside the magnetic structure. However, the scale-height is directly linked to the temperature through the sound speed. Thus, in chapter 3, the effects of different scale heights are considered and following the derivation of the governing equations the period ratio of fundamental to the first overtone is investigated. These are also discussed in the context of relevant observational measurements.

It is likely that the asymmetric behavior of plasma dynamics is connected to the deviation of coronal loop from a perfect semi-circular shape. In Chapter 4 we aim to investigate this geometrical effect and present our findings related to the effect of loop asymmetry on the P_1/P_2 period ratio.

Studies by Verth et al. (2007), showed that the loop's cross section area has also an effect on the period ratio. If density stratification tends to decrease the period ratio, the modification of the tubes cross section (magnetic field opening as we approach the apex) will increase the P_1/P_2 value. Morton and Erdélyi (2009) and Morton et al. (2010) studied the effect of cooling (plasma temperature depends on time) on the dynamics of kink oscillations and traveling waves. These authors found that the cooling of the plasma results in period decrease

and that energy stored in waves propagating in an unbounded plasma can be dissipated. Morton et al. (2011) used the same idea to study the properties of torsional Alfvén waves in coronal loops. Ruderman (2011a,b) examined this cooling and found that it generates an amplification of kink oscillations that appears to compete with the damping due to resonant absorption. In Chapter 5 we investigate the effect of the loop expansion through the solar corona on the period ratio P_1/P_2 and the the consequences of the inclusion of the length of the loop as a dynamical parameter on the estimations of the degree of density stratification.

Chapter 6 presents 2D magnetic reconnection in a stratified atmosphere using a Lagrangian code Lare2D. Following a model proposed by Roussev et al. (2002) we study magnetic reconnection in a 2D environment, focusing on the aspects of how different intial conditions, resitive terms and the inclusion of Hall term impact on the actual reconnection process.

In Chapter 7 we will summarize our conclusions and suggest new paths along which the present study can be expanded.

Chapter 2

Magnetohydrodynamics

In what follows we will present the mathematical equations and the approximations used in this thesis for modelling various physical mechanisms. All waves of interest can be described using the framework of magnetohydrodynamics (MHD), which describes the dynamics of magnetized fluids through a set of highly nonlinear equations combining the fluid equations, the continuity equations with Maxwell system of equations (interaction between electrically conducting fluid and magnetic field) where plasma is considered a continuous medium.

2.1 Derivation of MHD equations

We start by presenting the hydrodynamic equations, continuing with Maxwell's equations that describe the change in electric field, $\mathbf{E}$, magnetic field, $\mathbf{B}$, with current density, $\mathbf{J}$, and electric charge density, e combined with equations of mass continuity, motion, Ohm's law and ideal gas law. The combination of hydrodynamics and electromagnetism has formulated a theory that describes the motion of plasma permeated by magnetic field. There are two approaches when deriving the equations of MHD for the solar plasma. First, plasma can be described by its macroscopic properties, e.g. magnetic field, pressure, density, temperature, called single fluid approach. The second is using two-fluid model approach, where ions and electrons as charged particles are treated as two separate fluids which results into two sets of equations similar to the ones in the

single fluid approach. However, the present Thesis will assume the plasma to be electrically neutral with the temperature of different species equal, so the plasma will be treated as a single fluid, also the relative velocity of electrons and ions is considered small.

2.1.1 Equation of mass conservation

The stream of water is fatter near the mouth of the faucet, and skinnier lower down. This observational fact can be understood using conservation of mass. Since water is being neither created nor destroyed, the mass of the water that leaves the faucet in one second must be the same as the amount that flows past a lower point in the same time interval. The water speeds up as it falls, so the two quantities of water can only be equal if the stream is narrower at the bottom.
In mathematical terms the equation of mass conservation becomes

$$\frac{\partial \rho}{\partial t} + \nabla \cdot (\rho \mathbf{u}) = 0, \tag{2.1}$$

where ρ is the mass density and $\mathbf{u}$ is the velocity. Using Lagrangian time-derivate we can rewrite equation (2.1) in a equivalent form

$$\frac{D\rho}{Dt} = -\rho \nabla \cdot \mathbf{u}, \tag{2.2}$$

where

$$\frac{D}{Dt} = \frac{\partial}{\partial t} + \mathbf{u} \cdot \nabla.$$

is the material (total) time derivative.

2.1.2 Energy conservation

Suppose that a drop of water falls the faucet, at the beginning it has only potential energy, however, as it falls, it gains kinetic energy and its velocity increases. When it hits the sink the drop has only kinetic energy. Through its motion the initial potential energy is totally converted into kinetic energy, i.e. the energy of the system is always constant. The drop of water can change its

form but the amount of total energy does not change.

For an ideal fluid with no pressure perturbation the energy (entropy) equation has the form (Priest, 1982)

$$\frac{\rho^\gamma}{\gamma - 1}\frac{D}{Dt}\left(\frac{p}{\rho^\gamma}\right) = -L, \tag{2.3}$$

with ρ density and γ the ratio of the specific heats at constant pressure and volume (also known as the adiabatic index) and L, the energy loss function due to thermal conduction, radiation, viscosity, etc. If this loss function (heat losses/gains, radiative loss, and other heating sources) is zero (i.e. energy is conserved) then equation (2.3) can be written as (adiabatic limit)

$$\frac{Dp}{Dt} = \frac{\gamma p}{\rho}\frac{D\rho}{Dt} = -\gamma p \nabla \cdot \mathbf{u}. \tag{2.4}$$

An incompressible fluid leads to $D\rho/Dt = 0$, implying $\nabla \cdot \mathbf{u} = 0$. This approximation eliminates acoustic phenomena from the dynamics.

2.1.3 Ideal gas law

An ideal gas can be characterized by three variables that can fully describe the thermodynamic state of the gas: pressure (p), volume per unit mass ($V = 1/\rho$), and absolute temperature (T). The relationship between them may be deduced from kinetic gas theory and it constitute the ideal gas law, expressed as

$$P = \frac{R}{\mu}\rho T = \frac{k_B \rho T}{m} \tag{2.5}$$

where R is the universal gas constant, μ is the mean atomic weight, k_B is the Boltzmann constant, m is the mean particle mass.

2.1.4 Lorentz forces

The Lorentz force is the force exerted on a particle with charge q moving with velocity $\mathbf{u}$ through an electric field, $\mathbf{E}$, and magnetic field, $\mathbf{B}$. The total electromagnetic force, $\mathbf{F}$, acting upon the charged particle is called the Lorentz force

(after the Dutch physicist Hendrik A. Lorentz) and is given by

$$\mathbf{F} = q\mathbf{E} + q(\mathbf{u} \times \mathbf{B}). \tag{2.6}$$

The first term is contributed by the electric field while the second term is the magnetic force and has a direction perpendicular to both the velocity and the magnetic field.
A fluid carrying a current density $\mathbf{J}$ in a magnetic field, $\mathbf{B}$, experiences a bulk Lorentz force per unit volume

$$\mathbf{F} = \mathbf{J} \times \mathbf{B} = \frac{1}{\mu_0}(\nabla \times \mathbf{B}) \times \mathbf{B} \tag{2.7}$$

where μ_0 represents the magnetic permeability of free space. Using the vector identity

$$\nabla\left(\frac{1}{2}\mathbf{B} \cdot \mathbf{B}\right) = \mathbf{B} \times (\nabla \times \mathbf{B}) + (\mathbf{B} \cdot \nabla)\mathbf{B}$$

we can rearrange equation (2.7) as

$$\mathbf{F} = \mathbf{j} \times \mathbf{B} = \frac{1}{\mu_0}(\mathbf{B} \cdot \nabla)\mathbf{B} - \nabla\left(\frac{B^2}{2\mu_0}\right). \tag{2.8}$$

The first term represents the effect of a tension of magnitude B^2/μ_0 parallel to $\mathbf{B}$ and appears whenever the magnetic field lines are curved. The second term is due to the effect of a magnetic pressure of magnitude $B^2/2\mu_0$ per unit area. This force will be present when magnetic field, $\mathbf{B}$, varies from position to position. The interpretation of the first term $\mu_0^{-1}(\mathbf{B} \cdot \nabla)\mathbf{B}$ is more tricky. Let us write $\mathbf{B} = B\hat{s}$ where $\hat{s}$ is the unit vector in the direction of $\mathbf{B}$. Hence we can write

$$(\mathbf{B} \cdot \nabla)\mathbf{B} = (B\hat{s} \cdot \nabla)(B\hat{s}) = B\frac{d}{ds}(B\hat{s}) = B\frac{dB}{ds}\hat{s} + B^2\frac{d\hat{s}}{ds}$$

with s representing the coordinate measured along $\mathbf{B}$. Now $|\hat{s}| = 1$ so

$$0 = \frac{d}{ds}(\hat{s} \cdot \hat{s}) = 2\hat{s} \cdot \frac{d\hat{s}}{ds}.$$

Hence $d\hat{s}/ds$ is perpendicular to $\hat{s}$, which means we can write

$$\frac{d\hat{s}}{ds} = \frac{1}{R_c}\mathbf{n},$$

where $\mathbf{n}$ is perpendicular to $\hat{s}$ and R_c represents the radius of curvature (which is constant).

We can then write

$$\frac{1}{\mu}(\mathbf{B}\cdot\nabla)\mathbf{B} = \frac{d}{ds}\left(\frac{B^2}{2\mu_0}\right)\hat{s} + \frac{B^2}{\mu_0}\frac{1}{R_c}\mathbf{n}.$$

This is what we interpret as a *magnetic tension*. There is a net tension force when the field lines are curved.

2.1.5 Equation of motion

The fundamental law used to determine motion in magnetic fluids is Newton's second Law. The equation of motion derives from this law states that

$$\rho\frac{D\mathbf{u}}{Dt} = -\nabla p + \frac{1}{\mu_0}(\nabla\times\mathbf{B})\times\mathbf{B} + \mathbf{F}, \tag{2.9}$$

where

$$\mathbf{F} = \rho\mathbf{g} + F_e + F_u.$$

represents external forces that act on the plasma, $\rho\mathbf{g}$ is the gravitational force, F_e and F_u are the electrostatic and viscous forces respectively. The first term of equation (2.9) is due to pressure gradients and the second one represents the Lorentz force.

2.1.6 Induction equation

In MHD, the evolution and connection of electromagnetic fields, $\mathbf{E}$ and $\mathbf{B}$, are governed by Maxwell's equations, were we neglect the displacement current (we neglect electromagnetic waves of classical electrodynamics).

$$\frac{\partial\mathbf{B}}{\partial t} = -\nabla\times\mathbf{E}, \tag{2.10}$$

2.1

$$\nabla \cdot \mathbf{B} = 0, \tag{2.11}$$

$$\nabla \times \mathbf{B} = \mu_0 \mathbf{J}. \tag{2.12}$$

Taken in conjunction with Ohm's law which states that the current is proportional to the total electric field, neglecting, in the first instance Hall term, the current can be written as

$$\mathbf{J} = \sigma(\mathbf{E} + \mathbf{u} \times \mathbf{B}), \tag{2.13}$$

were the $\mathbf{u} \times \mathbf{B}$ term is due to the current induced by the Lorentz force on the charge carriers and σ representing the electrical conductivity. A more general form of this equation could include: the Hall term ($\mathbf{j} \times \mathbf{B}/en$), (electron) pressure term and inertial terms. We can rewrite equation (2.10) using $\nabla \times \mathbf{E} = -\partial \mathbf{B}/\partial t$ with Ohm's law (2.13) to obtain the induction equation as

$$\frac{\partial \mathbf{B}}{\partial t} = \nabla \times (\mathbf{u} \times \mathbf{B}) - \nabla \times (\eta \nabla \times \mathbf{B}), \tag{2.14}$$

where $\eta = 1/(\mu_0 \sigma)$ is the magnetic diffusivity. Assuming η constant and using the identity $\nabla \times (\nabla \times \mathbf{B}) = \nabla(\nabla \cdot \mathbf{B}) - (\nabla \cdot \nabla)\mathbf{B}$, together with the solenoidal condition (2.11), we transform the induction equation into

$$\frac{\partial \mathbf{B}}{\partial t} = \nabla \times (\mathbf{u} \times \mathbf{B}) + \eta \nabla^2 \mathbf{B}. \tag{2.15}$$

If V_0, L_0 are typical velocity and length-scales, the ratio of the first to the second term on the RHS of equation (2.15) is, in order of magnitude, the magnetic Reynolds number defined as

$$R_m = \frac{V_0 L_0}{\eta}. \tag{2.16}$$

The importance of resistivity (and in general all dissipative coefficients) depend on the location of physical mechanism under investigation and the mechanism itself. After all, transport coefficients depend on the density and temperature of the plasma. While for, e.g. the purpose of effective wave damping, the magnetic resistivity is far too small, for physical effects requiring the dissipation over short length scales (phase mixing, reconnection), magnetic resistivity is crucial. For

example in the solar corona above active region, where $T \approx 10^6$K, we find $R_m \approx 10^9$, and so the second term on the RHS of equation (2.15) is completely negligible.

Further neglecting magnetic resistivity (i.e. $\eta = 0$) we obtain the ideal induction equation

$$\frac{\partial \mathbf{B}}{\partial t} = \nabla \times (\mathbf{u} \times \mathbf{B}). \tag{2.17}$$

In this limit Alfvén frozen flux theorem holds, which states that magnetic field lines are frozen in the plasma. Plasma motion along the field line does not affect the magnetic field but transverse motions tend to drag the field lines with it. Equal lateral movement of field lines may push the plasma. This theorem breaks down when small length scales are considered.

2.2 Summary of ideal MHD equations and assumptions

The basic equations of MHD used for the work presented in this thesis are the equations of mass continuity, energy, ideal gas law, momentum equation, Ampere's law in the MHD limit and the induction equation (see equations (2.18-2.24). In order to employ the equations of hydrodynamics we must treat plasma as a continuum which requires typical length scales to be much greater that the internal plasma scales (gyro radii, electron inertia length, skin depth). Typical time scales are much larger than kinetic time scales. Plasma motion and characteristic speeds are much smaller than the speed of light, c, leading to relativistic effects being ignored. For the work in Chapter 3, Hall effects were ignored using a simplified Ohm's law (wave frequency much lower than ion cyclotron frequency).

We consider a fully neutral plasma, assuming that electron and ion number density are identical. Magnetic permeability, μ_0 and diffusivity, η, are taken as constant functions.

In the light of the above assumptions, we are going to deal with slow processes on a very large scale, described within the framework of ideal MHD theory that gives a good qualitative description of dynamics of the solar processes (see,

e.g. Priest 1982).

$$\frac{D\rho}{Dt} = -\rho\nabla\cdot\mathbf{u}, \tag{2.18}$$

$$\frac{Dp}{Dt} = \frac{\gamma p}{\rho}\frac{D\rho}{Dt} = -\gamma p\nabla\cdot\mathbf{u}, \tag{2.19}$$

$$p = \frac{R}{\mu_0}\rho T = \frac{k_B\rho T}{m}, \tag{2.20}$$

$$\rho\frac{D\mathbf{u}}{Dt} = -\nabla p + \frac{1}{\mu_0}(\nabla\times\mathbf{B})\times\mathbf{B} + \mathbf{F}, \tag{2.21}$$

$$\mathbf{j} = \frac{\nabla\times\mathbf{B}}{\mu_0}, \tag{2.22}$$

$$\frac{\partial\mathbf{B}}{\partial t} = \nabla\times(\mathbf{u}\times\mathbf{B}), \tag{2.23}$$

$$\nabla\cdot\mathbf{B} = 0. \tag{2.24}$$

In the following chapters we will also use one important parameter, *plasma beta*, denoted by (β), that represents the gas pressure of the plasma, p, divided by the magnetic pressure, $B^2/2\mu_0$, i.e.

$$\beta = \frac{2\mu_0 p}{B^2} \tag{2.25}$$

In the solar corona, the magnetic pressure $B^2/(2\mu_0)$ greatly dominates the gas pressure, so we can consider the plasma to be 'cold'. Typical plasma β in the solar corona with magnetic field of $B \approx 10$G, electron number $n_e \approx 1\times10^9\text{cm}^{-3}$ and temperature $T = 10^6$K, is of the order of $\beta \approx 0.07$.

To a good approximation the magnetic field in the solar corona is force-free since the plasma beta is much smaller than unity. This is not the case in the convection zone and photosphere where the plasma beta is usually much larger than unity ($\beta \gg 1$) and gas pressure dominates over magnetic pressure. When $\beta \ll 1$, magnetic forces dominate over pressure gradients, while in the $\beta \gg 1$ case the dynamics is driven by the force created by pressure gradient (Gary et. al 2001).

2.3 MHD wave modes in structured atmosphere

2.3.1 Ideal MHD solution

Using the ideal MHD equations described in the previous section we derive the governing equations of fundamental MHD waves modes propagating in a cylindrical tube of plasma (approximation made to represent a coronal loop). In the first instance we neglect gravity and viscous effects, i.e. in equation (2.21) we consider $\mathbf{F} = 0$. The equilibrium magnetic field, $\mathbf{B}_0$, density, ρ_0, pressure, p_0, are assumed uniform, with the magnetic field along z-axis ($\mathbf{B}_0 = B_0\hat{\mathbf{z}}$), $\hat{\mathbf{z}}$ representing the unit vector in the z-direction.

We examine the wave-like properties of the above mentioned atmosphere by using linear perturbation theory. Waves and oscillations can arise due to a perturbation of the equilibrium. Physical quantities are written as a sum of the equilibrium and their Eulerian perturbation i.e.

$$\mathbf{B} = \mathbf{B}_0 + \mathbf{B}_1(\mathbf{r}, t),$$

$$p = p_0 + p_1(\mathbf{r}, t),$$

$$\rho = \rho_0 + \rho_1(\mathbf{r}, t),$$

$$\mathbf{u} = 0 + \mathbf{u}_1(\mathbf{r}, t).$$

where $\mathbf{r}$ represents the coordinate. In a cartesian reference system, $\mathbf{r} = \mathbf{f}(x, y, z)$. Since we assume that amplitudes of the waves are small, we can neglect the products of perturbed quantities in the MHD equations.

By substituting these forms into the equations for mass continuity, induction, energy and momentum, using also the solenoidal condition, yields the following linearised equations

$$\frac{\partial \rho_1}{\partial t} + \rho_0 \nabla \cdot \mathbf{u}_1 = 0, \tag{2.26}$$

$$\frac{\partial \mathbf{B}_1}{\partial t} = \nabla \times (\mathbf{u}_1 \times \mathbf{B}_0), \tag{2.27}$$

$$\frac{\partial p_1}{\partial t} = c_s^2 \frac{\partial \rho_1}{\partial t}, \tag{2.28}$$

2.3

$$\rho_0 \frac{\partial \mathbf{u}_1}{\partial t} = -\nabla p_1 + \frac{1}{\mu}(\nabla \times \mathbf{B}_1) \times \mathbf{B}_0, \tag{2.29}$$

with $c_s = \sqrt{\gamma p_0/\rho_0}$ representing the sound speed.

Differentiating (2.29) with respect to time and eliminating perturbed quantities of magnetic field and pressure using equations (2.26), (2.27) and (2.28), we obtain a single equation for the velocity perturbation $u_1 = (u_x, u_y, u_z)$, given by (see, e.g. Lighthill 1960, Roberts 1981)

$$\frac{\partial^4 \Delta}{\partial t^4} - (c_s^2 + v_A^2)\frac{\partial^2}{\partial t^2}\nabla^2\Delta + c_s^2 v_A^2 \frac{\partial^2}{\partial z^2}\nabla^2\Delta = 0. \tag{2.30}$$

where $v_A^2 = B_0^2/(\mu_0\rho_0)$ is the Alfvén speed (see, e.g. Alfvén 1942), $\Delta = \nabla \cdot \mathbf{u}_1$, and ∇^2 is the Laplacian operator in Cartesian coordinates.

In the last sub-section, the MHD theory of a homogeneous plasma and magnetic field was discussed. However, in the solar corona the plasma fine structure is highly inhomogeneous. The plasma is confined to large structures such as loops, prominences and streamers which can be grouped into open and closed magnetic structures. The inhomogeneity and structuring arise from temperature gradients, density variations, a complicated magnetic field, gravitational forces and other effects. It is necessary to consider how these effects alter wave propagation. Further we are going to concentrate on particular type of magnetic structuring and ignoring the other effects.

2.3.2 Waves in a magnetic cylinder

The magnetic structuring takes the form of a uniform cylindrical tube of plasma with internal magnetic field $\mathbf{B}_i$, density ρ_i, pressure p_i confined to a region of radius a embedded in an external magnetic field $\mathbf{B}_e$, density ρ_e and pressure p_e (see Figure 2.1). Due to the requirement that stresses (Maxwell-Reynolds) must be continuous across the boundary, the total pressure, P_T, (kinetic and magnetic) is conserved. In order to relate the two media (internal/external) across the discontinuity, the solution of MHD equations need to satisfy the continuity conditions for the velocity normal to the magnetic surface (i.e. $[u_r] =$

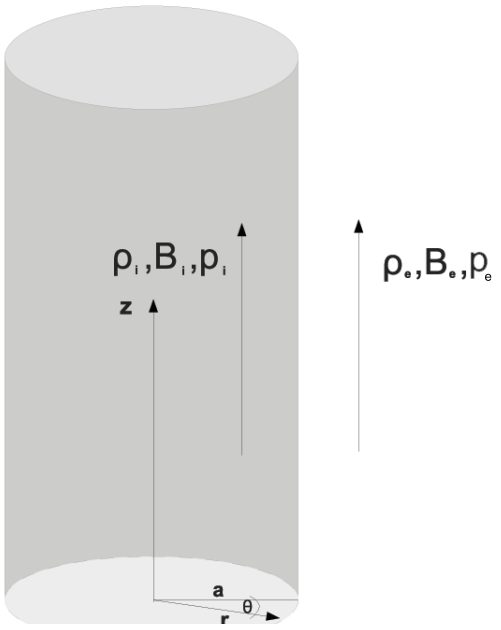

Figure 2.1: Equilibrium configuration for the magnetic cylinder with polar coordinates.

0) and total pressure ($[P_T] = 0$) across the discontinuity, i.e.

$$u_{ri} = u_{re},$$

and

$$p_i + \frac{B_i^2}{2\mu} = p_e + \frac{B_e^2}{2\mu}, \tag{2.31}$$

at the boundary $r = a$. (Note the brackets [ ] denotes the jump of quantity at $r = a$).

In the absence of a magnetic field, i.e. setting $v_A = 0$, equation (2.30) becomes a one-dimensional wave equation describing purely acoustic waves

$$\frac{\partial^2 u_z}{\partial t^2} = c_s^2 \frac{\partial^2 u_z}{\partial z^2}. \tag{2.32}$$

Equation (2.30) describes the propagation of fundamental MHD modes. De-

coupling Alfvén waves from equation (2.30) we obtain

$$\left(\frac{\partial^2}{\partial t^2} - v_A^2 \frac{\partial^2}{\partial z^2}\right)(\hat{\mathbf{z}} \cdot \nabla \times \mathbf{u}_1) = 0. \tag{2.33}$$

Equation (2.30), has been solved in various contexts (see, e.g. Spruit, 1982 and Edwin & Roberts, 1983) and yields

$$\rho_i(k^2 v_{Ai}^2 - \omega^2) m_e \frac{K_n'(m_e a)}{K_n(m_e a)} = \rho_e(k^2 v_{Ae}^2 - \omega^2) m_i \frac{I_n'(m_i a)}{I_n(m_i a)}, \tag{2.34}$$

where equation (2.34) constitutes the dispersion relation for surface waves ($m_i^2 > 0$), with (k,n,ω) representing the longitudinal wave number, the azimuthal wave number, and frequency, respectively. If $m_i \leq 0$, (so that $m_i^2 = -n_i^2 \leq 0$) the dispersion relation transforms into

$$\rho_i(k^2 v_{Ai}^2 - \omega^2) m_e \frac{K_n'(m_e a)}{K_n(m_e a)} = \rho_e(k^2 v_{Ae}^2 - \omega^2) n_i \frac{J_n'(n_i a)}{J_n(n_i a)}, \tag{2.35}$$

describing the propagation of body waves.

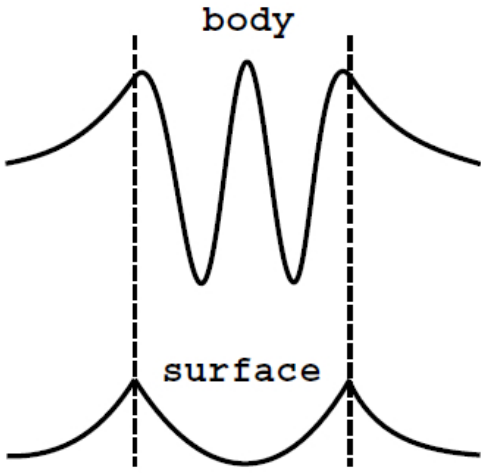

Figure 2.2: Body and surface waves in a flux tube. The body waves occupy the whole of the tube, whereas surface waves are largely confined to the region near the boundary of the tube.

Body modes are of oscillatory nature inside the tube and evanescent outside, while surface modes are evanescent both inside and outside of the tube. Here $J_n(x)$ is the Bessel function, $I_n(x)$ is the modified Bessel function of the first kind, with $K_n(x)$ the modified Bessel function of the second kind. I'_n represent the derivative of Bessel function with respect to its argument i.e. $I'_n(x) = (d/dx)I_n(x)$. The quantities m_i and m_e are defined as (Roberts, 1981a)

$$m_i^2 = \frac{(k^2c_i^2 - \omega^2)(k^2v_{Ai}^2 - \omega^2)}{(c_i^2 + v_{Ai}^2)(k^2c_T^2 - \omega^2)}; \qquad m_e^2 = \frac{(k^2c_e^2 - \omega^2)(k^2v_{Ae}^2 - \omega^2)}{(c_e^2 + v_{Ae}^2)(k^2c_{Te}^2 - \omega^2)},$$

where $c_T = c_i v_A/(c_i^2+v_{Ai}^2)^{1/2}$ is the internal tube speed, v_{Ai} is the internal Alfvén speed, c_i is the internal sound speed for $r < a$ and $c_{Te} = c_e v_{Ae}/(c_e^2 + v_{Ae}^2)^{1/2}$ the external tube speed, v_{Ae} is the Alfvén speed outside the tube, c_e is the external sound speed for $r > a$.

The azimuthal wave number, n, describes the shape of the tube. The $n = 0$ case refers to symmetrical pulsations where the central axis of the tube is undisturbed (sausage modes), $n = 1$ corresponds to anti-symmetric pulsation such that the tube supports lateral snake-like displacements from the axis of the tube (kink-modes), see Figure 2.3. For $n \geq 2$ we have the fluting modes which ripple the tube's boundary.

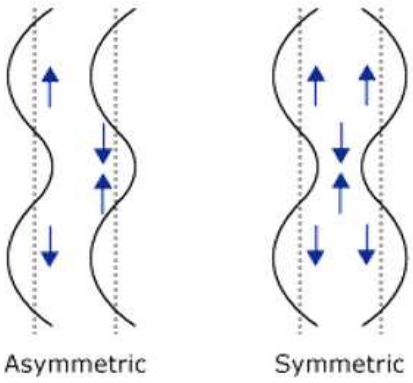

Figure 2.3: Asymmetric ($n = 1$) and symmetric ($n = 0$) mode.

Figure 2.4 presents the solutions for the dispersion relations (2.35) and (2.34) in the solar corona with speeds ordered as $v_{Ae} > v_A > c_s > c_T > c_e > c_{Te}$.

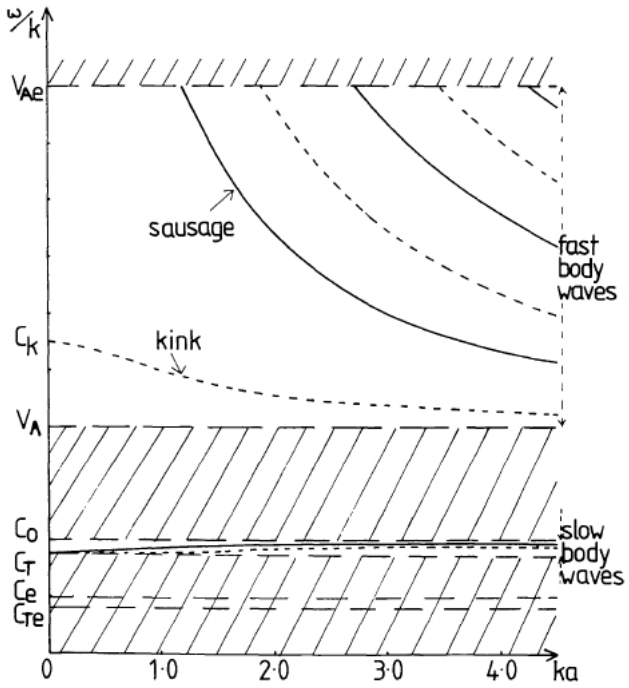

Figure 2.4: Solutions to Equations (2.35 and (2.34) under coronal conditions (adopted from Edwin and Roberts 1983)

Notice that under coronal conditions there are no surface waves. We can observe that the phase speeds of these modes split into fast and slow waves.

Fast modes are strongly dispersive and will exist if $v_{Ae} > v_{Ai}$. In the long wavelength limit ($ka \ll 1$) a cut-off frequency will trap the sausage modes with the kink and flute modes tending to c_k, the kink speed (see Edwin and Roberts 1983).

As Figure 2.4 shows, the solar corona is able to support a large number of different wave types. In the next section we are going to discuss about these fast and slow waves.

2.3.3 Fast waves

The sausage mode does not perturb the wave guide axis (in our case the cylinder axis), so no spatial displacement of the axis occurs. The cross section of the cylinder does experience an expansion and contraction (see Figure 2.3 symmet-

ric) due to the sausage mode. This leads to a number of different observational signatures.
If the loop cross section is perpendicular or almost perpendicular to the line of sight a periodic variation in the cross sectional area will be seen.
If the loop cross section is not perpendicular to the line of sight, then a periodic broadening of the line profile due to Doppler shifts can occur.

Periodic variation in the magnetic field leads to periodic patterns in synchrotron emission and can be detected in, e.g. radio waves or x-rays (Aschwanden, 1987).

The fast sausage mode has the cut-off which is dependent upon the radius, length and density of the magnetic cylinder (see, e.g. Nakariakov et al. 2003). Below this cut-off value, the sausage oscillations are classed as leaky. From equation (2.35) when $n = 0$ the condition for the cut-off of the sausage modes is given by

$$k_c a = j_0 \left[\frac{(c_s^2 + v_A^2)(v_{Ae}^2 - c_T^2)}{(v_{Ae}^2 - v_A^2)(v_{Ae}^2 - c_s^2)} \right]^{1/2} \tag{2.36}$$

with k_c representing the cut-off wavenumber and $j_0 \approx 2.40$ is the first zero of the Bessel Function of the first kind. If $\rho_i \gg \rho_e$ then equation (2.36) reduces to

$$k_c a \approx j_0 \frac{v_A}{v_{Ae}}. \tag{2.37}$$

with period of the sausage mode in the corona as

$$P_{sm} < \frac{2\pi}{k_c v_{Ae}} \approx \frac{2\pi a}{j_0 v_A}. \tag{2.38}$$

The period of the global sausage mode (also known as standing mode) when $k \to k_c$ is given by $P = 2L/v_{Ae}$, where L is the loop length. Substituting this into equation (2.38) we obtain the final condition for the existence of sausage modes

$$\frac{L}{2a} < \frac{\pi v_{Ae}}{2 j_0 v_A} \approx 0.65 \sqrt{\frac{\rho_i}{\rho_e}}. \tag{2.39}$$

The above equation shows that most likely candidates to observe fast sausage wave in the solar atmosphere will be magnetic structures with large radii, large density contrast with the exterior plasma and structures with short lengths.

The fast kink mode in the long wavelength is highly incompressible (unlike the sausage mode) and displaces the magnetic cylinder axis (wave guide). A consequence of this is that fast kink oscillations are best identified by instruments that can observe spatial displacement of the loop axis. Due to incompressibility of this mode no variation in the intensity of the loop emission can be detected. It will cause modulation in the intensity emission if there is a component of the loop displacement in the line of sight of the observing instrument (Cooper et al. 2003). Also signatures in the Doppler shift can be detected if the motion of the magnetic structure is in the line of sight.

2.3.4 Slow waves

These slow waves waves are polarised parallel to the magnetic field and are acoustic in nature (they are still modified by the magnetic field). Slow waves are difficult to detected with current imagers available due to the longitudinal nature (the modulation of structure cross section due to the sausage mode and displacement of the loop axis due to the kink mode will be small wehn $c_s \ll v_A$). The phase speed for the mode also needs to be close to the local sound speed. It is possible to distinguish observationally between the slow propagating and standing modes. The propagating mode will cause the intensity variations to move along the supporting magnetic structure with a velocity close to the sound speed of the local plasma. On the other hand, for the standing mode the density and velocity perturbations should be out of phase by a quarter of the wave period (see, e.g. Sakurai et al. 2002). Owen et al. (2009) found that the value of the phase shift was also dependent on local plasma properties and thermal conduction.

2.3.5 Transverse oscillations in a magnetic cylinder

Transverse waves transfer energy in a direction perpendicular to the direction of the disturbance in the medium. A vibrating string is an example of a transverse wave. Although all points on the string itself are constrained to move only up and down, wave pulses move perpendicularly along the length of the string. The wave speed is the speed with which a pulse moves along the string. When

the motion of the masses is in a direction perpendicular to the direction of the springs in the equilibrium state, the oscillations are said to be transverse.

Let us derive the dispersion relation of these waves for a kink mode in a slender tube (a different method can be found in Ryutov and Ryutova 1976). By slender tube we refer here to a thin flux tube. We take the total pressure $P_T = P$ for simplicity.

In the following derivation we choose to work with the plasma displacement perturbation $\boldsymbol{\xi} = (\xi_r, \xi_\phi, \xi_z)$, instead of the velocity $\mathbf{u}_1 = (u_r, u_\phi, u_z)$, since it simplifies the algebra involved (see, e.g. Goossens et al. 1992). First we introduce the Lagrangian displacement $\boldsymbol{\xi}_0 + \boldsymbol{\xi}$, where ξ_0 is the Lagrangian displacement in the unperturbed state as in (Ruderman 2010). The quantity $\boldsymbol{\xi}$ represents the perturbation of the Lagrangian displacement. In the initial position the Lagrangian description is used to label a plasma element. Following Goossens et al. (1992) the plasma element is labeled by the position where it would be if the flow had not been perturbed (quasi-Lagrangian). In this description $\boldsymbol{\xi}$ is called the plasma displacement. An invariant representation of the relation between $\boldsymbol{\xi}$ and $\mathbf{u}_1$ is

$$\mathbf{u}_1 = \frac{\partial \boldsymbol{\xi}}{\partial t} + \nabla \times (\boldsymbol{\xi} \times \mathbf{u}_0) - \boldsymbol{\xi} \nabla \cdot \mathbf{u}_0 + \mathbf{u}_0 \nabla \times \boldsymbol{\xi}. \tag{2.40}$$

If the equilibrium flow is incompressible, the third term in the right-hand side of equation (2.40) vanishes. The components of the Eulerian perturbation of velocity are then related to the components of Lagrangian displacement as

$$u_r = \frac{\partial \xi_r}{\partial t} \tag{2.41}$$

$$u_\phi = \frac{\partial \xi_\phi}{\partial t} - \xi_r r \frac{d}{dr}\left(\frac{u_z}{r}\right) \tag{2.42}$$

$$u_z = \frac{\partial \xi_z}{\partial t} - \xi_r \frac{du_z}{dr} \tag{2.43}$$

2.3

Equations (2.26)-(2.29), then can be reduced to

$$\frac{\partial^4 P}{\partial t^4} - (c_s^2 + v_A^2)\nabla^2 \frac{\partial^2 P}{\partial t^2} + c_s^2 v_A^2 \nabla^2 \frac{\partial^2 P}{\partial z^2} = 0, \tag{2.44}$$

$$\frac{\partial^2 \xi_r}{\partial t^2} - v_A^2 \frac{\partial^2 \xi_r}{\partial z^2} = -\frac{1}{\rho_0}\frac{\partial P}{\partial r}, \tag{2.45}$$

$$\frac{\partial^2 \xi_\phi}{\partial t^2} - v_A^2 \frac{\partial^2 \xi_\phi}{\partial z^2} = -\frac{1}{r\rho_0}\frac{\partial P}{\partial \phi}, \tag{2.46}$$

$$\frac{\partial^2 \xi_z}{\partial t^2} - c_T^2 \frac{\partial^2 \xi_z}{\partial z^2} = -\frac{c_T^2}{\rho v_A^2}\frac{\partial P}{\partial z}, \tag{2.47}$$

$$b_r = B_0 \frac{\partial \xi_r}{\partial z}, \;\; b_\phi = B_0 \frac{\partial \xi_\phi}{\partial z}, \;\; b_z = -\frac{B_0}{r}\left(\frac{\partial (r\xi_r)}{\partial r} + \frac{\partial \xi_\phi}{\partial \phi}\right), \tag{2.48}$$

$$\rho = -\rho_0 \left(\frac{\partial (r\xi_r)}{\partial r} + \frac{1}{r}\frac{\partial \xi_\phi}{\partial \phi} + \frac{\partial \xi_z}{\partial z}\right), \;\; p = c_s^2 \rho, \tag{2.49}$$

with ∇^2 representing the Laplacian operator in cylindrical coordinates

$$\nabla^2 = \frac{1}{r}\frac{\partial}{\partial r}\left(r\frac{\partial}{\partial r}\right) + \frac{1}{r^2}\frac{\partial^2}{\partial \phi^2} + \frac{\partial^2}{\partial z^2}. \tag{2.50}$$

Taking variables proportional to $exp(i(n\phi + kz - \omega t))$, equations (2.44-2.49) transform into

$$\frac{d^2 P}{dr^2} + \frac{1}{r}\frac{dP}{dr} - \left(m^2 + \frac{n^2}{r^2}\right) P = 0, \tag{2.51}$$

$$(\omega^2 - v_A^2 k^2)\xi_r = \frac{1}{\rho_0}\frac{dP}{dr}, \tag{2.52}$$

$$(\omega^2 - v_A^2 k^2)\xi_\phi = \frac{inP}{r\rho_0}, \tag{2.53}$$

$$(\omega^2 - v_A^2 k^2)\xi_z = \frac{ic_T^2 kP}{\rho_0 v_A^2} \tag{2.54}$$

with

$$m^2 = \frac{(c_s^2 k^2 - \omega^2)(v_A^2 k^2 - \omega^2)}{(c_s^2 + v_A^2)(c_T^2 k^2 - \omega^2)} \tag{2.55}$$

We work in cold plasma approximation with plasma pressure much smaller than the magnetic pressure, i.e. Alfvén speed is much larger than the sound

speed. For $n = 1$ mode, and for $c_s = c_T = 0$ and equation (2.55) reduces to

$$m^2 = k^2 - \frac{\omega^2}{v_A^2}. \tag{2.56}$$

Assuming that the loop length, L, is much larger than the size of the system in the transverse direction, we can introduce the parameter $\epsilon = a/L \ll 1$, where a represents the width of the loop. The other components of the wave-number (k, ω) are proportional to $(1/\lambda, \lambda)$, which leads to $ka \sim a/\lambda$. If this is true, then ka is of order of ϵ which leads to $\omega(a/v_A) \sim \epsilon$. The quantity a/v_A is the Alfvénic time in the transverse direction.

For the system configuration as provided in the early Figure 2.1 we solve the problem in the internal and external regions and then match the solutions asymptotically together in a narrow intermediate region where both expansions are valid.

In the outer region we take the pressure to be

$$P_e = A_e K_1(m_e \epsilon r), \tag{2.57}$$

with

$$m_e^2 = \frac{k^2}{\epsilon^2} - \frac{\omega^2}{\epsilon^2 v_{Ae}^2} \tag{2.58}$$

Since $m_e R \sim 1$, we can expand the modified Bessel function $K_1(z)$ in (Abramowitz and Stegun 1964)

$$K_1(z) = \frac{1}{z} + ln\left(\frac{z}{2}\right) I_1(z) - \frac{1}{4}\sum_{k=0}^{\infty}[\psi(k+1) + \psi(k+2)]\frac{(1/4)^k z^{2k}}{k!(1+k)!}, \tag{2.59}$$

where the expansion form of $I_1(z)$ is given by

$$I_1(z) = \frac{1}{2} z \sum_{k=0}^{\infty} \frac{(1/4)^k z^{2k}}{k!\Gamma(k+2)}, \tag{2.60}$$

with $\Gamma(z) = \int_0^\infty t^{z-1} e^{-t} dt$ and $\psi(z)$ representing the Digamma function defined

2.3

as

$$\psi(z) = \frac{d}{dz} ln\Gamma(z) = \frac{\Gamma'(z)}{\Gamma(z)}.$$

With $z = m_e \epsilon r$, since $r \sim a$ and ϵ is small, we can neglect terms of the order of ϵ^2 or higher, i.e. neglect terms $O(z^2)$, K_1 therefore becomes

$$K_1(z) = \frac{1}{z} + \frac{1}{2} z \ln\left(\frac{z}{2}\right) - \frac{1}{4}[\psi(1) + \psi(2)]z, \tag{2.61}$$

where $\psi(1) + \psi(2) = 0.0386$.
The pressure in the outer region for $r \sim R$, to order ϵ is

$$P_e = \hat{A}_e \left[\frac{1}{m_e r} + \frac{1}{2} m_e \epsilon^2 \ln(\epsilon) r + \frac{1}{2} m_e \epsilon^2 r \ln(m_e r/2) - \psi m_e \epsilon^2 r\right]. \tag{2.62}$$

where $\hat{A}_e = \frac{A_e}{\epsilon}$ and $\psi = 1/4[\psi(1) + \psi(2)]$. Next we solve the problem in the

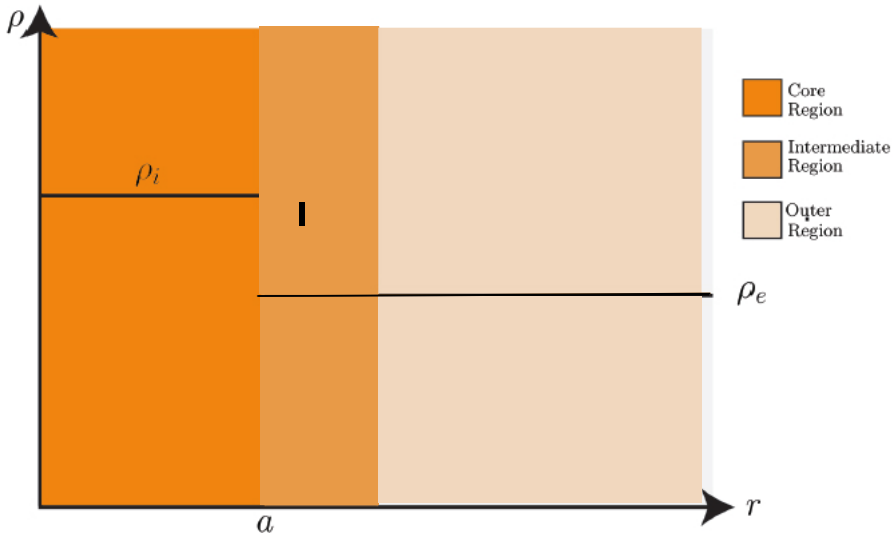

Figure 2.5: A graph showing the three regions, the core, intermediate and outer regions.

intermediate region, neglecting terms in $O(\epsilon^2 ln(\epsilon))$ or greater. Using equation (2.51) we obtain

$$\frac{d^2 P}{dr^2} + \frac{1}{r}\frac{dP}{dr} - \frac{P}{r^2} = 0 \tag{2.63}$$

with the solution

$$P = Ar + \frac{B}{r} \tag{2.64}$$

where A and B are constants.
Matching the inner and outer solution we find that $A = 0$ so the solution of the intermediate pressure, P_I, is given by

$$P_I = \frac{B}{r}. \tag{2.65}$$

We now turn our attention to internal pressure, P_i. Inside the loop the $1/r$ term is neglected to avoid singularities, hence we can write

$$P_i = A_i r \tag{2.66}$$

In order to find the frequency, ω, at the tube boundary we use the previously discussed jump conditions for pressure and plasma displacement $\xi = (\xi_r, \xi_\phi, \xi_z)$ i.e.

$$[P] = 0, \quad [\xi_r] = 0, \tag{2.67}$$

where the jump condition can be expressed generally as

$$[f] = \lim_{\epsilon \leftarrow +0} f(a+\epsilon) - f(a-\epsilon). \tag{2.68}$$

From equation (2.52), we obtain that

$$\xi_r = \frac{1}{\rho(\omega^2 - v_A^2 k^2)} \frac{dP}{dr}. \tag{2.69}$$

Using the jump condition for the total pressure at $r = R$, yields

$$\frac{B_I}{R} = RA_i. \tag{2.70}$$

Imposing the continuity of the radial displacement for the pressure term using

jump conditions at the tube boundary we derive

$$-\frac{B_I}{R^2\rho_e(\omega^2 - v_{Ae}^2k^2)} = \frac{A_i}{\rho_i(\omega^2 - v_{Ai}^2k^2)} \tag{2.71}$$

The system of equation has a non-trivial solution only when its denominator is zero. Hence we derive the dispersion relation,

$$\omega = kc_k, \tag{2.72}$$

with c_k the kink speed given by

$$c_k^2 = \frac{\rho_e v_{Ae}^2 + \rho_i v_{Ai}^2}{\rho_e + \rho_i}. \tag{2.73}$$

This speed represents the phase speed of a fast kink mode in a slender tube of cylindrical geometry, result first obtained by Ryutov and Ryutova (1976), valid only in the lowest order approximations in ϵ. The kink speed can also be interpreted as a density weighted Alfvén speed. This expression also tells us that the kink speed is situated between the internal and external Alfvén speed.

2.4 Magnetic reconnection

In what follows we will present the mathematical formalism used in magnetic reconnection theory, emphasizing the approximations usually employed in the analysis of the magnetic reconnection. MHD equations are represented by equations (2.18)-(2.24), which are now extended so that the induction equation includes a resistive term and for the energy conservation we use the equation for internal energy, which includes non-ideal terms.
The requirement for induction equation is

$$\frac{\partial \mathbf{B}}{\partial t} = \nabla \times (\mathbf{v} \times \mathbf{B}) + \eta \nabla^2 \mathbf{B}, \tag{2.74}$$

$$\nabla \cdot \mathbf{B} = 0, \tag{2.75}$$

while internal energy conservation requires

$$\rho\frac{de}{dt} + p\nabla\cdot\mathbf{v} = \nabla\cdot(\mathbf{K}\cdot\nabla\mathbf{T}) + (\eta_e\cdot\mathbf{j})\cdot\mathbf{j} + Q_v - Q_r. \tag{2.76}$$

In the above equations, η is the electrical resistivity. In equation (2.76) e is the internal energy per unit mass, $\mathbf{K}$ is the thermal conductivity tensor, η_e is the electrical resistivity tensor, Q_v is the heating by viscous dissipation and Q_r is the radiative energy loss.

There are several different ways one can classify magnetic reconnection, the primary way being the classification in terms of its rate, while other aspects, such as the collisional or collisionless character of the plasma, can be viewed in terms of their effect on the reconnection rate. There are also other subtle issues to be considered here as to: how do the different terms in the energy equation affect reconnection, what are the properties of turbulent or impulsive bursty reconnection and how does reconnection occur in a collisionless plasma?

During the process of reconnection, pairs of magnetic field lines are brought in towards the X-point, they then lie along the separatrices (curved surfaces in space that divide different bundles of flux) and are broken and reconnected. A schematic picture of reconnecting magnetic field lines is given in Figure 2.6.

2.4.1 Sweet-Parker approximation

The Sweet-Parker model consists of a simple diffusion region of length L and width 2l, lying between oppositely directed magnetic fields (see Figure 2.6), for which an order-of-magnitude analysis may be easily conducted. For a steady state, the plasma must carry the field lines inward at the same speed as they are trying to diffuse outward, so that

$$v_i = \frac{\eta}{l}, \tag{2.77}$$

where v_i represents the internal flow. Since the electric field is uniform for a steady state, its value may be found by evaluating the expression $\mathbf{E}+\mathbf{v}\times\mathbf{B} = \mathbf{j}/\sigma$

where $Ampère's$ Law states that

$$\mathbf{j} = \nabla \times \mathbf{B}/\mu_0. \tag{2.78}$$

The conservation of mass implies that the rate $(4\rho L v_i)$ at which mass is entering the sheet from both sides must equal the rate $(4\rho l v_0)$ at which it is leaving through both ends, so that

$$L v_i = l v_A, \tag{2.79}$$

where $v_0 = v_A$ is the outflow speed. The half width (l) may now be eliminated between our two basic Sweet-Parker equations, (2.77) and (2.79), to give the square of the inflow speed as :

$$v_i^2 = \frac{\eta v_A}{L}. \tag{2.80}$$

In dimensionless variable equation (2.80) may be rewritten as

$$M_i = \frac{(v_A/v_{Ai})^{1/2}}{(R_{mi})^{1/2}}, \tag{2.81}$$

where v_{Ai} is the Alfvén speed at the inflow and

$$M_i = \frac{v_i}{v_{Ai}}, \tag{2.82}$$

is the inflow Alfvén Mach number (or dimensionless reconnection rate) and

$$R_{mi} = \frac{L v_{Ai}}{\eta}, \tag{2.83}$$

is the magnetic Reynolds number based on the inflow Alfvén speed. Once v_A and v_i are known for a given L, the sheet half width can be obtained using

$$l = L\frac{v_i}{v_A}, \tag{2.84}$$

and the outflow magnetic field strength (B_a) is determined from flux conservation

$$v_i B_i = v_A B_a, \tag{2.85}$$

as

$$B_a = B_i \frac{v_i}{v_A}. \tag{2.86}$$

From equation (2.78) the order-of-magnitude electric current is $j \approx B_i/(\mu_0 l)$ and so the Lorentz force along the sheet is $(\mathbf{j} \times \mathbf{B})_x \approx jB_a{=}B_i B_a/(\mu_0 l)$. This force accelerates the plasma from rest at the neutral point to v_A over a distance L and so, by equating the magnitude of the inertial term $\rho(\mathbf{v}\cdot\nabla)v_x$ to the above Lorentz force and neglecting the plasma pressure gradient, we have

$$\rho \frac{v_A^2}{L} \approx \frac{B_i B_a}{\mu l}. \tag{2.87}$$

However, from the condition $\nabla \cdot \mathbf{B} = 0$ we obtain

$$\frac{B_a}{l} \approx \frac{B_i}{L}, \tag{2.88}$$

and so the right-hand side of equation (2.87) may be rewritten as $B_i^2/(\mu L)$ and we have

$$v_A = \frac{B_i}{(\mu\rho)^{1/2}} \equiv v_{Ai}. \tag{2.89}$$

Not surprisingly, we have found that the magnetic forces accelerate the plasma to the Alvén speed.

The fields therefore reconnect for this basic model at a speed given by equation (2.81) as

$$v_i = \frac{v_{Ai}}{R_{mi}^{1/2}}. \tag{2.90}$$

in terms of the (inflow) Alfvén speed (v_{Ai}) and magnetic Reynolds number ($R_{mi} = Lv_{Ai}/\eta$). The plasma is ejected from the sheet of half width

$$l = \frac{L}{R_{mi}^{1/2}}, \tag{2.91}$$

at speed $v_A = v_{Ai}$ and with a magnetic field strength

$$B_a = \frac{B_i}{R_{mi}^{1/2}}. \tag{2.92}$$

Since $R_{mi} \gg 1$, we therefore have $v_i \ll v_{Ai}$, $B_a \ll B_i$ and $l \ll L$, the reconnection rate is very small, the fields reconnect at 10^{-3} to 10^{-6} of the Alfvén speed - much too slow for a solar or stellar flare. One way to improve this situation is to take into account other mechanisms in order to have a more realistic reconnection rate (see Petschesk′s model) and also take into account the effect of Hall term which may act towards accelerating the process.

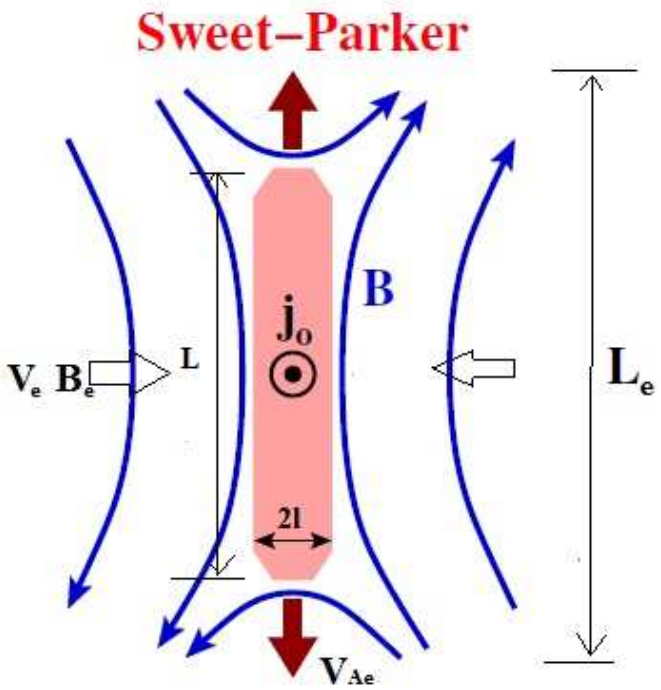

Figure 2.6: A simple diffusion region of length L and width $2l$, lying between oppositely directed magnetic fields in which a Sweet-Parker type reconnection takes place.

For a steady-state two-dimensional configuration with a zero-gradient ($\partial/\partial_x = \partial/\partial_y = 0$) with flow and field components (v_x, v_y) and (B_x, B_y) depending on x

and y, the electric field (E_0) has only a z-component.

It can be calculated how reconnection can be expressed in terms of the plasma flow at any point in the plane as

$$E_0 = v_y B_x - v_x B_y + \frac{j}{\sigma},$$

where E_0 is the uniform electric field and σ is the electrical conductivity.

The following three characteristic speeds are therefore important in the steady two-dimensional reconnection: the *external flow speed*, v_e, at a fixed global distance from the neutral point; the *Alfvén speed*, $v_{Ae} = B_e/(\mu\rho)^{1/2}$, in terms of the corresponding magnetic field B_e; and the global magnetic diffusion speed ($v_{de} = \eta/L_e$). Using these three characteristic speeds we may construct two independent dimensionless parameters which characterize steady, two-dimensional magnetic reconnection, namely the *external Alfvén Mach number*

$$M_e = \frac{v_e}{v_{Ae}}, \tag{2.93}$$

and the global *magnetic Reynolds number*,

$$R_{me} = v_{Ae}/v_{de}. \tag{2.94}$$

based on the Alfvén speed.

Now for a simple X-line (see Figure 2.6) in which the current density is very small outside the diffusion region, the reconnection rate can be expressed in terms of the velocity (v_e) of the plasma flowing towards the neutral line as

$$E_0 = v_e B_e = M_e v_{Ae} B_e.$$

at the distance L_e from the X-point, where $v_y = v_e$, $B_x = B_e$, $v_x = 0$, j=0, and v_{Ae} and B_e are regarded as fixed. Thus, for a steady-state system, the Alfvén Mach number (M_e) at the boundary of the system is a dimensionless measure of the rate of reconnection.

In a steady-state system the reconnection is super-slow, slow, or fast depending on the magnitude of the reconnection rate (M_e) relative to the magnetic

Reynolds number (R_{me}). The magnetic Reynolds number is the key parameter, because it measures the ability of magnetic field lines to diffuse through the plasma.

Chapter 3

Environment effect on the P_1/P_2 kink oscillations period ratio

The aim of this Chapter is to investigate, using a semi-analytical approach, the effect of the surrounding environment on the period ratio P_1/P_2 and the consequences of including a distinct environment on estimations of the density stratification. This work has also been published in A&A by Orza et al. (2012).

3.1

3.1 Introduction

The P_1/P_2 period ratio of transversal loop oscillations is currently used for the diagnostics of longitudinal structuring of coronal loops as its deviation from 2 is intrinsically connected to the density scale-height along coronal loops and/or the sub-resolution structure of the magnetic field. The same technique can be applied not only to coronal structures, but also to other oscillating magnetic structures. The oscillations in magnetic structures are described by differential equations whose coefficients depend on the longitudinal structure of the plasma. Using the method developed by McEwan et al. (2008), we investigate how the temperature of the environment compared to the temperature of the magnetic structure influences the P_1/P_2 ratio for coronal and prominence conditions.

Reviews by Patsourakos & Vial (2002), Labrosse et al. (2010), and Mackay et al. (2010) provide a detailed information about the physics of solar prominences. Although prominences are located in the corona, they possess temperatures a hundred times lower and densities a hundred or a thousand times larger than typical coronal values. The fact that their physical conditions are akin to those in the chromosphere suggests one possible scenario for prominence formation, in which prominences are made of chromospheric material which has been lifted up into the corona. Although the processes that lead to prominence formation are still under investigation, another proposed scenario to explain how prominences acquire their mass is condensation and cooling of plasma from the surrounding corona. In eclipse or coronagraph pictures, prominences appear as bright (in emission) structures at the limb, but in H_α-images of the disc they show up as dark (in absorption) ribbons, which are called filaments. One must bear in mind that both structures, prominences and filaments, are the same phenomenon observed from two different points of view, the two names remaining because of historical reasons. In this work, we indistinctly use both names to refer to such magnetic structures. The possible changes of P_1/P_2 are translated into quantities that are used in the process of remote plasma diagnostics in the solar atmosphere.

We will restrict our attention only to the effect of density stratification (see Figure 3.1). All previous studies (see e.g. Andries et al. 2005 McEwan et

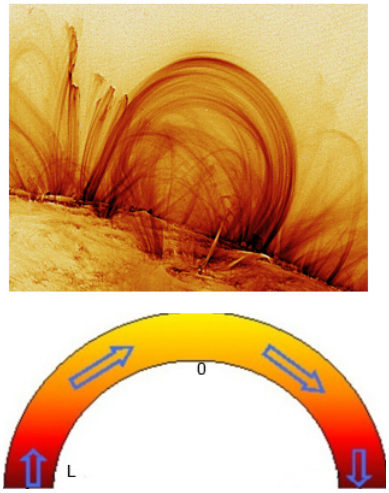

Figure 3.1: Temperature difference between inside and outside of a coronal loop, image from Hinode SDO (upper image). Density stratification for our coronal loop of length 2L with 0 representing the apex and L the footpoint of the loop.

al. 2006, Van Doorsselaere et al. 2007, Verth et al. 2007, Ballai et al. 2011), considered that the density stratification (indirectly the scale-height) is identical inside and outside the magnetic structure. However, the scale-height is directly linked to the temperature (via the sound speed) and an equal scale-height would mean an equal temperature, clearly not applicable for, e.g. coronal loops and/or prominence fibrils. EUV observations made by the recent high-resolution space satellites (SOHO, TRACE, STEREO, Hinode, SDO) showed that, after all, coronal loops are enhancements of plasma and the density of a typical loop can be as much as 10 times larger than the density of its environment (see e.g. Warren et al. 2002; Winebarger et al. 2003; Winebarger and Warren 2005; Ugarte-Urra et al. 2006, 2009; Mulu-Moore et al. 2011; Viall & Klimchuk 2011). The heating of these coronal structures - according to accepted theories (see, e.g. Klimchuk 2006, Erdélyi and Ballai 2007 and references therein)- occurs at the footpoints, while thermal conduction, flows, waves, instabilities and turbulences will help the heat to propagate along the full length of the loop. It is also obvious (as seen in X-ray by, e.g. Hinode/XRT) that the temperature of the loop exceeds the temperature of the environment. The typical length of a coronal loop is 20-200 Mm (see e.g. Reale 2002a, 2003), which means that

the density inside the loop (seen in EUV) can vary by an order of magnitude, leading to the necessity of studying the effect of density stratification on the oscillations of coronal loops.

As pointed out for the first time by Dymova and Ruderman (2005, 2006), the propagation of kink waves in a straight tube in the thin tube approximation can be described by

$$\frac{\partial^2 v_r}{\partial t^2} - c_k^2(z)\frac{\partial^2 v_r}{\partial z^2} = 0, \tag{3.1}$$

where v_r denotes the radial (transversal) component of the velocity vector and the quantity c_k is the propagation speed of kink waves defined by equation (2.73)

For identical magnetic field inside and outside the tube, the fact that $\rho_i > \rho_e$ means that $v_{Ae} > v_{Ai}$ since $v_A = B/(\sqrt{\mu_0 \rho})$ with μ_0 representing the magnetic permeability. If we lift the thin flux tube restriction, then equation (3.1) must be complemented by terms that would describe dispersion. As we specified, our approach is using the cold plasma approximation in which the dynamics of kink oscillations in a coronal loop is described by equation (3.1).

3.2 Mathematical method

Assuming that all temporal changes occur with the same frequency, ω, we can consider that the temporal dependence of variables (including v_r) has the form $\sim \exp(i\omega t)$, which means that the PDE given by equation (3.1) transforms into

$$\frac{d^2 v_r}{dz^2} + \frac{\omega^2}{c_k^2(z)} v_r = 0. \tag{3.2}$$

In reality the kink speed does not depend only on the longitudinal coordinate, z, but on radial coordinate too. It is known that the dependence on the transversal coordinate, r, leads to the phenomena requiring the development of short transversal length scales (resonant absorption, phase mixing, turbulence, wave leakage), possibly responsible for the rapid damping of kink oscillations (see, e.g. Ofman and Aschwanden 2002, Ruderman and Roberts 2002, Dymova and Ruderman 2006, etc). Equation (3.2) implies that the eigenfunctions, v_r, are driven

by certain forms of $c_k(z)$, through the particular profile of the quantities that make up the kink speed (density, magnetic field). Inspired by the eigenvalue problem of Rayleigh-Ritz procedure, McEwan et al. (2008) used a variational principle that allows the calculation of eigenvalues, ω, a method we will also employ in our analysis. Let us multiply equation (3.2) by v_r and integrate from the apex ($z = 0$) to the footpoint ($z = L$) of the loop as

$$\int_0^L v_r \frac{d^2 v_r}{dz^2} dz + \omega^2 \int_0^L \frac{v_r^2}{c_k^2(z)} dz = 0. \tag{3.3}$$

where L is the half-length of the loop. Using integration by parts in the first integral we obtain

$$\int_0^L v_r \frac{d^2 v_r}{dz^2} dz = v_r \frac{dv_r}{dz}\bigg|_0^L - \int_0^L \frac{dv_r}{dz}\frac{dv_r}{dz} dz \tag{3.4}$$

Taking into account only the fundamental mode, we need to satisfy the boundary conditions

$$v_r(L) = \frac{dv_r(0)}{dz} = 0,$$

while for the first harmonic we have

$$v_r(0) = v_r(L) = 0.$$

As a consequence, the first term on the RHS of equation (3.4) disappears and equation (3.3) simplifies to

$$\omega^2 \int_0^L \frac{v_r^2}{c_k^2(z)} dz = \int_0^L \left(\frac{dv_r}{dz}\right)^2 dz. \tag{3.5}$$

This equation is similar to the equation derived by McEwan et al. (2008), and we can write

$$\omega^2 = \frac{\Psi_1}{\Psi_2}, \tag{3.6}$$

where

$$\Psi_1 = \int_0^L \left(\frac{dv_r}{dz}\right)^2 dz, \quad \Psi_2 = \int_0^L \frac{v_r^2}{c_k^2(z)} dz.$$

3.2

In order to express the eigenvalues of such problem, we consider some trial functions for v_r that satisfy the boundary conditions imposed at the footpoints and the apex of the loop. Since we are interested only in the characteristics of the fundamental mode of kink oscillations and its first harmonic, we will assume that $v_r(z)$ will be proportional to $\cos(\pi z/2L)$ for the fundamental mode and $\sin(\pi z/L)$ for the first harmonic. These choices for eigenfunctions correspond to the homogeneous plasma, however - as we show in the Appendix - the corrections to the eigenfunction due to density stratification are small.

3.3 Density profile

The problem of how the kink speed depends on the longitudinal coordinate, z, is a rather interesting problem and only simplified cases can be solved analytically. For simplicity, let us consider that the magnetic field inside and outside of the coronal loop are identical and homogeneous, while the density varies exponentially according to

$$\rho_i(z) = \rho_i(0) \exp\left(\frac{2L}{\pi H_i} \sin\frac{\pi z}{2L}\right),$$

$$\rho_e(z) = \rho_e(0) \exp\left(\frac{2L}{\pi H_e} \sin\frac{\pi z}{2L}\right), \tag{3.7}$$

where $\rho_i(0)$ and $\rho_e(0)$ are the densities inside and outside the loop at $z = 0$, i.e. at the the loop apex and H_i and H_e are the density scale-heights inside and outside the loop. Obviously the choice of density reflects a simplified description of the coronal loop model where plasma is isothermal and other further effects such as gravity and magnetic field dependence on cartesian coordinates (instead of a constant) are neglected. A realistic description would require taking into account that the plasma is not isothermal (inside and outside the loop), the loop is curved and the density can depend on other coordinates, as well. This form of density dependence on the z coordinate was earlier used by, e.g. Verth et al. 2007, McEwan et al. 2008, Morton and Erdélyi 2009, Morton and Ruderman 2011, Morton et al. 2011. With our chosen density profiles, the kink speed as in (3.1) becomes

$$c_k^2(z) = \frac{\rho_i \frac{B_0^2}{\mu_0^2 \rho_i} + \rho_e \frac{B_0^2}{\mu_0^2 \rho_e}}{\mu)0^2[\rho_i(z) + \rho_e(z)]} = \frac{2B_0^2}{\mu_0^2[\rho_i(z) + \rho_e(z)]} =$$

$$= \frac{2v_{Ai}^2(0)}{\exp\left(\frac{2L}{\pi H_i} \sin\frac{\pi z}{2L}\right) + \xi^{-1} \exp\left(\frac{2L}{\pi H_{i\chi}} \sin\frac{\pi z}{2L}\right)}, \tag{3.8}$$

where B_0 is the magnitude of the magnetic field, $v_{Ai}(0)$ is the Alfvén speed at the apex of the loop (0), and ξ is the density ratio, i.e. $\rho_i(0)/\rho_e(0)$. Since the density outside the coronal loop is smaller than inside, we will consider that

$\xi \geq 1$. The quantities H_i and H_e are the density scale-heights and they are proportional to the temperature of the plasma. Here we denoted $\chi = H_e/H_i$. Since the temperature of the loop is larger than its environment, we will take $\chi \leq 1$; the value $\chi = 1$ corresponds to an identical density variation with height inside and outside the loop and identical temperatures. The limit $\chi \to \infty$ indicates a constant density in the environment of the loop, while the limit $\chi \to 0$ represents a case when the plasma inside the loop is homogeneous.

3.4 Solutions

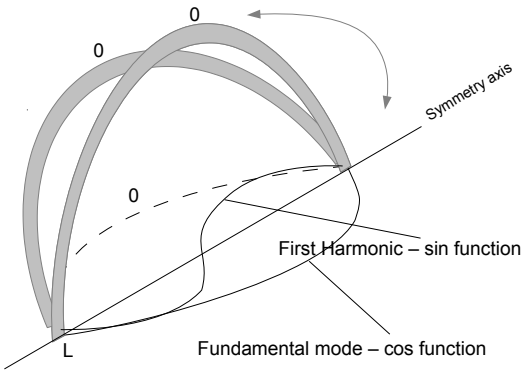

Figure 3.2: Fundamental and First harmonic modes of oscillations.

Using the particular form of $v_r \sim \cos(\pi z/2L)$ for the fundamental mode and $v_r \sim \sin(\pi z/2L)$ for first harmonic (see Figure 3.2), we obtain that in the case of the fundamental mode

$$\Psi_1^f = \int_0^L \left(\frac{d\cos(\pi z/2L)}{dz}\right)^2 dz = \frac{\pi^2}{8L},$$

$$\Psi_2^f = \int_0^L \cos^2\left(\frac{\pi z}{2L}\right) \cdot \frac{\exp\left(\frac{2L}{\pi H_i}\sin\frac{\pi z}{2L}\right) + \xi^{-1}\exp\left(\frac{2L}{\pi H_i \chi}\sin\frac{\pi z}{2L}\right)}{2v_{Ai}^2(0)} dz = \frac{\pi}{8yv_{Ai}^2(0)} \times$$
$$\times \left\{ I_1(2y) + L_1(2y) + \xi^{-1}\chi\left[I_1\left(\frac{2y}{\chi}\right) + L_1\left(\frac{2y}{\chi}\right)\right]\right\}, \qquad (3.9)$$

where we introduced the dimensionless variable $y = L/\pi H_i$, $I_\nu(x)$ is the modified Bessel function of order ν, $L_\nu(x)$ is the modified Struve function of order ν, and the index f stands for the fundamental mode. For the first harmonic we obtain that

$$\Psi_1^1 = \int_0^L \left(\frac{d\sin(\pi z/2L)}{dz}\right)^2 dz \frac{\pi^2}{2L},$$

$$\Psi_2^1 = \frac{\pi}{4y^2 v_{Ai}^2(0)} \left\{ \frac{3+2y^2}{y} \left[I_1(2y) + L_1(2y)\right] - 3\left[I_0(2y) + \right] \right.$$

$$+L_0(2y) + \frac{4y}{\pi} + \xi^{-1}\chi^2 \left[\frac{\chi}{y}\left(3 + \frac{2y^2}{\chi^2}\right)\left(I_1\left(\frac{2y}{\chi}\right) + L_1\left(\frac{2y}{\chi}\right)\right) \right.$$

$$\left. \left. -3\left(I_0\left(\frac{2y}{\chi}\right) + L_0\left(\frac{2y}{\chi}\right)\right) + \frac{4y}{\pi\chi}\right]\right\}, \tag{3.10}$$

where the superscript 1 in the expressions of Ψ_1^1 and Ψ_2^1 stands for the first harmonic. Now using equation (3.6) for both modes,

$$\frac{P_1}{P_2} = \sqrt{\frac{\Psi_2^f \Psi_1^1}{\Psi_1^f \Psi_2^1}}. \tag{3.11}$$

Inspecting the above relations, we can see that the period ratio P_1/P_2 does not depend on Alfvén speed or loop length (they cancel out when calculating equation 3.11). The above approximation for $P_1/P2$ is valid only when the density is almost constant. For coronal conditions we plot the period ratio given by equation (3.11) for $\xi = 2$ with the variable y varying between 0 and 10, although the larger values of y are rather unrealistic since $y = 10$ would correspond to a scale-height of 30 times shorter than the loop length (the scale-height corresponding to a typical temperature of 1 MK is 47 Mm). Another variable in our problem is the ratio of scale-heights (i.e. temperature ratio), χ. This will be varied in the interval 0 to 1.

The dependence of the P_1/P_2 period ratio on χ and the ratio $L/\pi H_i$, for coronal conditions ($\xi = 2$) is shown in Figure 3.3 with the case discussed earlier by, e.g. Andries et al. (2005) corresponding to the value $\chi = 1$. In addition to the ratio $L/\pi H_i$, our model prescribes a possible diagnostic of the temperature difference between the loop and its environment. The importance of changes

3.4

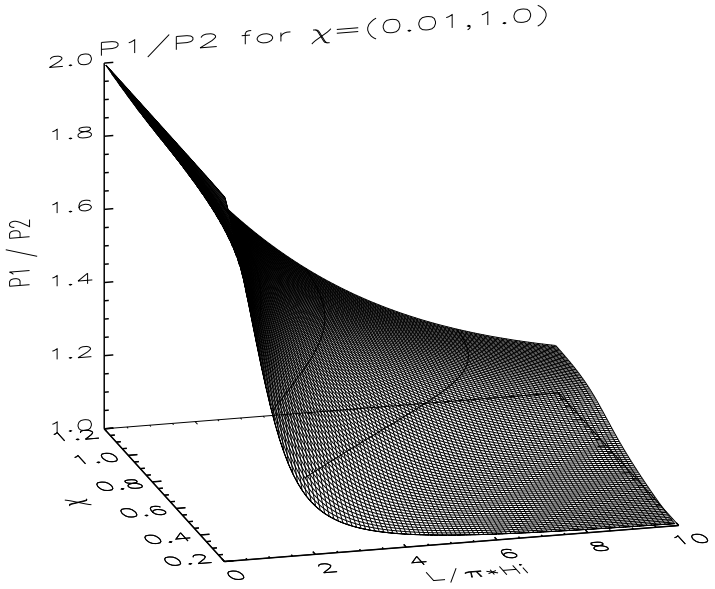

Figure 3.3: The variation of the P_1/P_2 period ratio with the temperature parameter, χ, and the ratio, $L/\pi H_i$, for the case of a typical coronal loop (here the density ratio, ξ, is 2).

when the different temperature of the environment is taken into account can be shown in a relative percentage plot shown in Figure 3.4. The relative change was calculated as the percentage change of the results of our investigation compared to the case when $\chi = 1$. As we can see, the changes in the domain corresponding to values of χ close to 1 are not significant. However, as the temperature of the environment becomes lower than the temperature inside the loop, this difference shows changes of the order of 10-20 % for values of χ of up to 0.5, while for the cases with χ near zero, the difference can be even 40 % (for $\chi = 0.2$ and $L/\pi H_i = 2$). Since the relative change is negative, it means that for the same value of P_1/P_2 calculated assuming the same temperature the ratio, $L/\pi H_i$ is overestimated. A change of 25% in the period ratio occurring at approximate values of $L/\pi H_i = 0.8$ and $\chi = 0.65$ would mean that for environment temperature is 35 % less than the loop temperature, the scale-height is underestimated by about 25%. It is important to note that the density ratio, ξ, has an important effect on the variation of period ratio. An increase

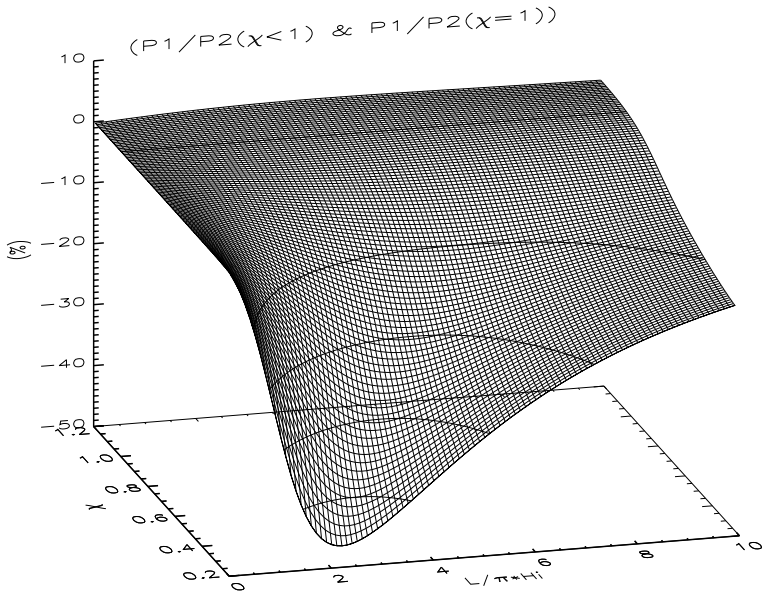

Figure 3.4: The relative variation of the P_1/P_2 period ratio with the temperature parameter, χ, and the ratio $L/\pi H_i$ for the case of a typical coronal loop (the density ratio, ξ, is taken to be 2).

in ξ to the value of 10 would result in relative percentage change reduction and the maximum value of the change is attaining its maximum value at 33 % (for $\chi \approx 0.2$ and $L/\pi H_i = 1$).

The same analysis was repeated for prominence structures. These structures are known to be of chromospheric origin and show rather long stability. Prominence fibrils are surrounded by much hotter and less denser corona. For these structures we suppose that the density of the prominence is two orders of magnitude higher, i.e. we take $\xi = 100$. The typical temperature of prominences varies between 5×10^3 and 10^4 K (see, e.g. Lin et al. 2003), while the temperature of the surrounding corona can be even two orders of magnitude higher. Thus, the value of χ is chosen to change in the interval 50-150. As we can see in Figure 3.5, the changes of the period ratio P_1/P_2 for prominences does not show large variation with χ and an analysis of the relative change (compared to the case corresponding to $\chi = 50$) would reveal that these changes are of the order of 0.1 %.

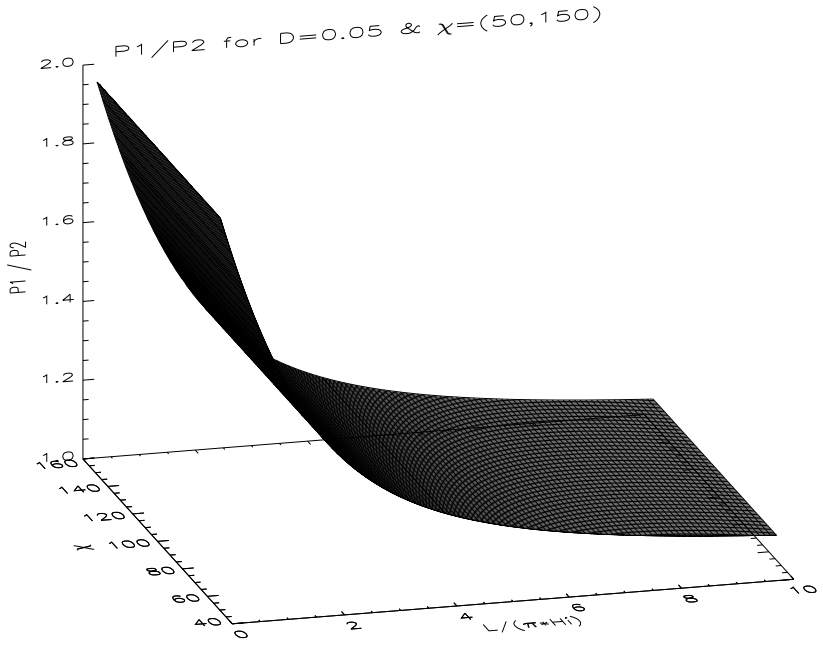

Figure 3.5: The same as in Figure 3.3 but we plot the variation of P_1/P_2 for prominences where $\xi = 100$ and χ varies between 50 and 150.

3.5 Implications for magneto-seismology

The immediate implication upon magneto-seismology of the solar corona of our calculations is that the P_1/P_2 period ratio has no one-to-one correspondence with the internal stratification of the magnetic structure, but depends also on the temperature ratio between the interior and exterior of the magnetic structure, i.e. an observed period ratio allows the diagnostics of the temperature ratio, too. Our analysis shows that the effect of temperature difference is more pronounced for those cases where the temperature inside the waveguide is larger than outside (e.g. coronal loops) and, in general, negligible in prominence cases. For coronal loops it is also evident that noticeable effects of the temperature difference on the P_1/P_2 ratio are encountered for relative small values of $L/\pi H_i$ (say, below 5) and temperature ratio that are smaller than 70%.

Our analysis also opens a new way of diagnosing the multi-temperature loops and their environment. The relations derived in the present study show that the physical parameters entering the problem are the density ratio, temperature

ratio and the ratio of loop length to the scale-height. Out of these quantities, the density is the parameter that can be determined (although with errors) from emission measurements, so we will suppose that the value of ξ is known. The diagnostics of the loop in the light of the new introduced parameter becomes possible once we specify an additional relation connecting the temperature ratio and the density scale-height measured against the length of the loop. As a possibility we investigate the case when for the same loop we can determine not only the period of the fundamental mode (P_1) and its first harmonic (P_2) but also the period of the second harmonic, here denoted by P_3. Now we can form a new ratio, P_1/P_3, which can be determined in a similar way as above. Since the measurement of the three periods refer to the same loop we can estimate the value of χ and $L/\pi H_i$ in a relatively easy way.

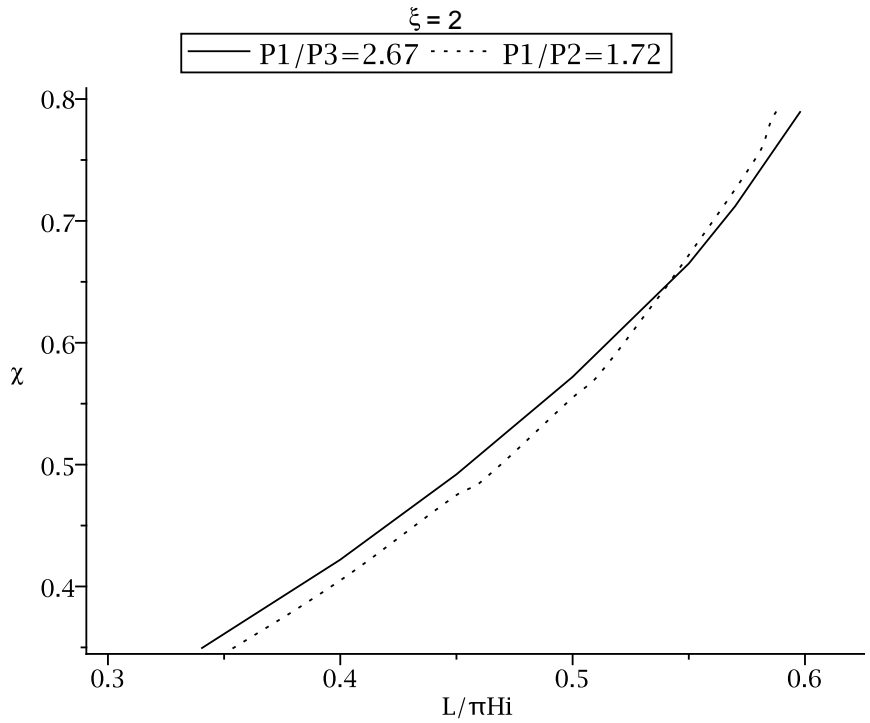

Figure 3.6: An example on how the period ratio of the first three harmonics of a coronal loop kink oscillations can be used to diagnose the density scale-height of the loop and the temperature difference between the coronal loop and its environment. Here the P_1/P_2 dependence is shown by the dotted line while the solid line stands for the value of P_1/P_3.

In Figure 3.6 we illustrate such a case. We suppose that for a loop of half-length of 150 Mm with an Alfvén speed at the apex of the loop of 1000 km s^{-1} we measure the period ratio of 1.72 for P_1/P_2 and 2.67 for P_1/P_3 (two arbitrary values for this study). By specifying the value of the period measurement means that in a dependence similar to the one shown in Figure 3.3 we obtain an arc which in a $(L/\pi H_i, \chi)$ coordinate system will look like the dotted line curve in Figure 3.6. In a similar way, for the value of $P_1/P_3 = 2.67$ we would obtain another curve, here shown by the solid line (here the curves are the projections of the intersection of similar surfaces as in Fig 3.3 with the horizontal surface corresponding to the specified period ratio). Since the two measurements correspond to the same loop, their intersection point will give us the exact value of $L/\pi H_i$ and χ. For the particular example used here we obtain $L/\pi H_i = 0.57$ and $\chi = 0.67$. Our results show very little sensitivity with the density ratio, for example, if the ratio would be 10 then the intersection point would change to $L/\pi H_i = 0.54$ and $\chi = 0.66$.

3.6 Summary

In order to carry out coronal seismology it is imperative to know the relationship between the composition of a plasma structure and the oscillations supported by the coronal loop. High resolution observations may allow an accurate diagnostic of not only the magnetic field strength, but also the thermodynamical state of the plasma.

The period ratio P_1/P_2 (and its deviation for the canonical value of 2) belonging to the period of transversal fundamental kink mode and its first harmonic is a useful tool for diagnosing the longitudinal structure of magnetic regions. In our study we investigated the effect of the environment on the period ratio assuming that the density scale-heights (implicitly the temperature) inside and outside magnetic structures are different.

Using a simple mathematical method first applied in the context of loop oscillations by McEwan et al. (2008), we derived for the first time an analytical expression that connects the value of the period of kink oscillations and parameters of the loop. We showed that in the case of coronal loops, the effect

of temperature difference between the loop interior and exterior can lead to changes of the order of 30-40% that could have significant implications on the diagnosis of longitudinal density structuring of the coronal loop. In the case of prominences, given the very large density and temperature difference between the prominence and coronal plasma, the changes in P_1/P_2 due to the different temperature are very small.

Since our model introduces a new variable in the process of plasma diagnostic a new relation is needed that connects the parameters of interest. To illustrate the possibilities hidden in our analysis we have chosen the case when the same loop shows the presence of the additional second harmonic. Superimposing the dependencies of the P_1/P_2 and P_1/P_3 ratios with respect to the temperature ratio factor, χ and $L/\pi H_i$ we could find the set of the values that satisfies a hypothetical measurement.

Finally we need to emphasize that our approach supposes a certain degree of simplification, therefore our results do not provide an absolute qualitative and quantitative conclusion. First we assumed that the loop is thin, and equation (3.1) can be applied to describe the dynamics of kink oscillations in coronal loops. It is obvious that this statement is not true for very short loops (the ratio of the loop ratio and its length is not very small) in which case, the governing equation has to be supplemented by an extra term. Secondly, our isothermal supposition of the loop and its environment does need refinement, as observations (see, e.g. Winebarger et al. 2003, Warren et al. 2008, Berger et al. 2011, Mulu-Moore 2011) show that the loops are not always in hydrostatic equilibrium nor isothermal. Here we assumed the idealistic situation of a static background, however recent analysis by Ruderman (2011) showed that the temporal dependence of density through flow and cooling can also influence the ratio of the two periods.

Chapter 4

The P_1/P_2 period ratio for kink oscillations of an asymmetrical coronal loop

In This Chapter we aim to investigate another geometrical effect, namely the asymmetry of the coronal loop, i.e. its deviation from a semi-circular shape used by most of previous studies on the periods of oscillation. Our aim is to study the fundamental and first kink eigenmodes of an asymmetric coronal loop with fixed ends in the dense photosphere. In order to make analytical progress, we consider cold plasma approximations and take into account the effect of density stratification, so the change in the value of P_1/P_2 ratio is connected to the density scale-height that quantifies the variation of density along the magnetic structure. This chapter is based on the results published by Orza and Ballai (2013) .

4.1 Introduction

Observed asymmetries of coronal loops were found as early as 1970s (see Kjeldseth Moe & Nicolas 1977). Later Dere & Mason (1993) observed a large range of velocities associated with non-thermal components in the quiet and active regions of the Sun. Recent observations of asymmetries in coronal line profiles by Peter (2001), Hara et al. (2008), De Pontieu et al. (2009), De Pontieu & McIntosh (2010a), Peter (2010), Martínez et al. (2011) show that information hidden in details of spectral line profiles can exhibit significant deviations from a single Gaussian in coronal lines formed in active regions. These observations consisted in the discovery of a strongly blueshifted component in the coronal lines at the footpoints of the loop (Hara et al. 2008). The blueward asymmetries found were of the order of 5%-10% in spectral lines in the low corona. Observed asymmetries were also interpreted in terms of nanoflare models where nanoflares at coronal heights lead to high speed evaporative upflows (see e.g. Patsourakos & Klimchuk 2006). Martínez et al. (2011) found that asymmetrical line profiles can arise from the convolution along the line of sight of emission from different parcels of plasma with different Doppler velocity and/or temperatures dominating the different emission sources.

In the present Chapter we will assume that the observed asymmetric behaviour of plasma dynamics is connected to the deviation of the coronal loop from a perfect semi-circular shape. Obviously there are many other mechanisms that can act as a source of asymmetry (different cooling/ heating rate) but here, for the sake of simplicity, we will concentrate on one single aspect.

4.2 Initial set-up

We start by considering MHD kink oscillations in the thin tube approximation whose dynamics is given by equation (3.1) (see, e.g. Dymova and Ruderman 2005, 2006). Following Ruderman (2010), we use the Lagrangian displacement $\boldsymbol{\xi} = (\xi_r, \xi_\theta, \xi_z)$, as described in Chapter 2, to find the displacement of the tube

axis (asymmetry). Hence we can write here

$$\frac{\partial^2 \xi_r}{\partial t^2} - c_k^2(z)\frac{\partial^2 \xi_r}{\partial z^2} = 0, \qquad \xi_r(0) = \xi_r(L) = 0, \tag{4.1}$$

where ξ_r is the plasma displacement, defined as in equation (2.40).

In order to study the asymmetry of a coronal loop, we introduce a new parameter, α, that is connected to the loop displacement or distorsion (deviation from a semi-circular loop). To pursue further with analytics, we change our coordinate system from loop plane coordinate system (x, z, Cartesian) to a new polar coordinate system (r, θ) with $\theta \in [0, \pi]$ as in Figure 4.1.

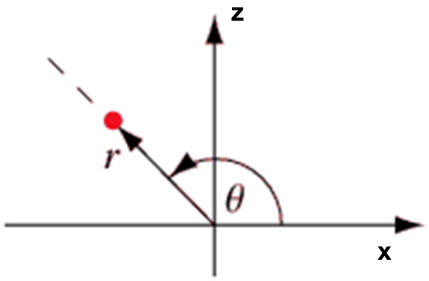

Figure 4.1: The polar coordinate system, with r (the radial coordinate) and θ (the angular coordinate, often called the polar angle)

The new coordinates, r, and θ, are defined in terms of Cartesian coordinates through

$$z = r\sin\theta,$$

$$x = r\cos\theta,$$

where r is the radial distance from the origin, and θ is the counterclockwise angle from the x-axis.

In terms of x and z we have,

$$r = \sqrt{x^2 + z^2}, \tag{4.2}$$

$$\theta = \tan^{-1}\left(\frac{z}{x}\right). \tag{4.3}$$

The arc length of a polar curve given by $r = r(\theta)$ is

$$s = \int_{\theta_1}^{\theta_2} \sqrt{r^2 + \left(\frac{dr}{d\theta}\right)^2}\, d\theta, \tag{4.4}$$

and the line element is given as

$$ds^2 = dr^2 + r^2 d\theta^2. \tag{4.5}$$

Denoting H_1 to be the loop height, and introducing the asymmetry (distorsion) of the loop (see Figure 4.2) through a parameter, α, that quantifies the loop displacement, we have that:

$$z = H_1 \sin\theta,$$

$$x = H_1 \cos\theta + \alpha H_1 \cos 2\theta \ - \alpha H_1.$$

We consider that the temporal dependence of variables has the form $\exp(i\omega t)$

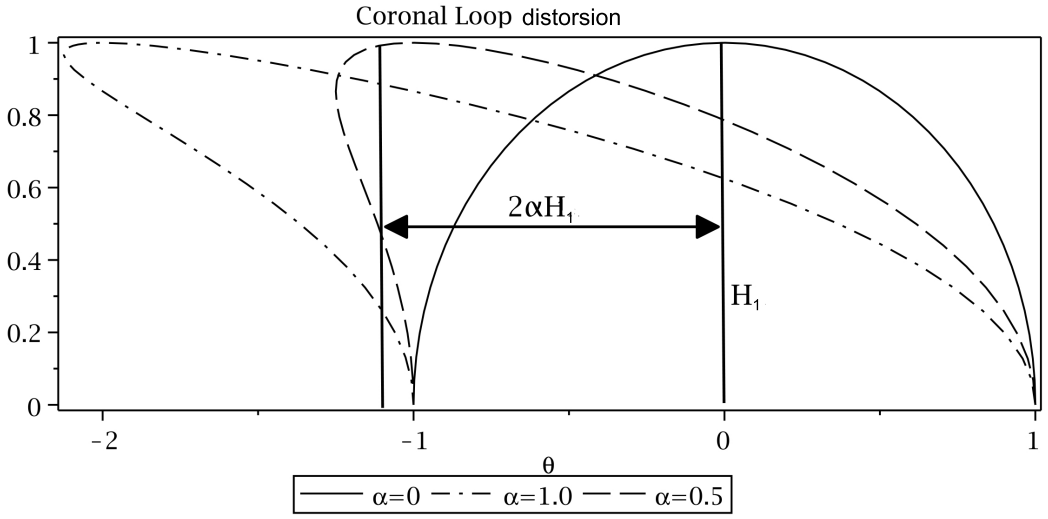

Figure 4.2: The loop shape for different distorsion parameter α. For $\alpha = 0.0$ the loop is symmetric (semi-circular), the height of the loop is the same for asymmetric loop profiles.

and we express the z-derivative from equation (4.1) in terms of the arc length,

s as,

$$\frac{d}{dz^2} = \frac{d}{ds^2}\left(\frac{ds}{dz}\right)^2,$$

from equation (4.5) it follows that

$$ds^2 = dx^2 + dz^2 + r^2 d\theta^2.$$

The propagation of kink waves in a loop in the thin flux tube approximation becomes

$$\frac{d^2\xi_r}{ds^2} + \frac{\omega^2}{c_k^2(s)}\xi_r = 0, \qquad \xi_r(0) = \xi_r(\pi) = 0. \tag{4.6}$$

We are working in thin flux tube approximation and by changing to the coordinate along the loop we simplify equations involved further. There are two possible scenarios one could assume for an asymmetric loop: (i) constant height and (ii) constant length. Case (ii) is more complex because for a constant loop length with deviation from a semi-circular shape we increase the magnetic tension in one leg of the loop at the expense of the other one and equation (4.6) would not anymore be valid.

Further we are interested in the geometrical effects, so we consider that the loop has a constant height, i.e. we are dealing with case (i) and we are going to study coronal loops with different α parameter rather than study the real time asymmetry of a loop, which would implicate more complex analysis, i.e. case (ii).

Under the above assumptions the arc length from equation (4.4) can then be calculated as

$$\left(\frac{ds}{d\theta}\right)^2 = \left(\frac{dz}{d\theta}\right)^2 + \left(\frac{dx}{d\theta}\right)^2 =$$

$$H_1^2(1 + 4\alpha \sin\theta \sin 2\theta + 4\alpha^2 \sin^2 2\theta).$$

In order to solve equation (4.6) we would require the kink speed as $c_k(s)$, which is difficult to express. It turns out that equation (4.6) becomes easier to solve in terms of coordinate θ

$$\frac{d\xi_r}{ds} = \frac{d\xi_r}{d\theta} \cdot \frac{d\theta}{ds}.$$

It is straightforward to show that

$$\frac{d\theta}{ds} = \frac{1}{H_1\sqrt{1+4\alpha\sin\theta\sin 2\theta+4\alpha^2\sin^2 2\theta}},$$

therefore the first term of equation (4.6) can be written as:

$$\frac{d^2\xi_r}{ds^2} = \frac{d^2\xi_r}{d\theta^2}\left(\frac{d\theta}{ds}\right)^2 + \frac{d\xi_r}{d\theta}\frac{d}{d\theta}\left(\frac{d\theta}{ds}\right)\frac{d\theta}{ds}$$

As a result, equation (4.6) in the new variable becomes

$$A(\theta)\frac{d^2\xi_r}{d\theta^2} - B(\theta)\frac{d\xi}{d\theta} + \frac{\omega^2}{c_k^2(\theta)}\xi_r = 0, \tag{4.7}$$

where the coefficients $A(\theta)$ and $B(\theta)$ are given by

$$A(\theta) = \frac{1}{H_1^2(1+4\alpha\sin\theta\sin 2\theta+4\alpha^2\sin^2 2\theta)},$$

and

$$B(\theta) = \frac{1}{2}\frac{4\alpha\sin 2\theta(\cos\theta+2\cos 2\theta+4\alpha\cos 2\theta)}{H_1^2(1+4\alpha\sin\theta\sin 2\theta+4\alpha^2\sin^2 2\theta)^2}.$$

Next we consider that the inside and outside magnetic field of the coronal loop are identical, while the density varies exponentially according to (see, e.g. Verth et al. 2007, McEwan et al. 2008, Morton and Erdélyi 2009, Morton and Ruderman 2011, Morton et al. 2011):

$$\rho_i = \rho_{f_i}\exp\left[-\frac{z}{H}\right] = \rho_{f_i}\exp\left[-\frac{H_1\sin(\theta)}{H}\right],$$

$$\rho_e = \rho_{f_e}\exp\left[-\frac{z}{H}\right] = \rho_{f_e}\exp\left[-\frac{H_1\sin(\theta)}{H}\right]. \tag{4.8}$$

According to these relations, the density decreases from ρ_{f_i}, ρ_{f_e} at footpoint ($\theta = 0$, with 'i' referring to interior and 'e' referring to exterior) to the apex ($\theta = \pi/2$) and then increases back to ρ_{f_i}, ρ_{f_e} at the other footpoint ($\theta = \pi$). In the above relation H is the density scale-height for an isothermal plasma (the same value inside and outside the loop), and ρ_{fi}, ρ_{fe}, are the densities inside

and outside the loop at the footpoints.

In the new variable, equation (2.73) becomes

$$c_k^2(\theta) = \frac{c_k^2(\theta = 0)}{\exp\left[-\frac{\pi y H_1}{L}\sin(\theta)\right]}, \tag{4.9}$$

where $c_k(\theta = 0)$ is the kink speed at the footpoints of the loop and can be expressed as

$$c_k^2(\theta = 0) = \frac{2B_0^2}{\rho_{fi} + \rho_{fe}} = \frac{2v_{Ai}^2(f)}{1 + D},$$

where $D = \rho_{fe}/\rho_{fi}$ is a density ratio parameter, B_0 is the magnetic field in the loop, $y = L/(\pi H)$ and $v_{Ai}(f)$ is the Alfvén speed at the footpoints of the loop. We consider that $D < 1$ (density outside the loop is smaller than inside).

The above density profile is valid for a simplified model of a coronal loop where we considered plasma to be isothermal and all other effects related to this are neglected. A more realistic profile would require a non-isothermal plasma description.

4.3 Results

For coronal conditions we consider the density ratio parameter $\rho_e/\rho_i = D = 0.5$ (same as in chapter 3), $D = \rho_e(0)/\rho_i(0)$ with the density stratification parameter $L/(\pi H)$ varying between 0 and 4. Larger values of y would correspond to unrealistic scale-heights. Another variable in our problem is α that quantifies the loop distorsion. The quantity $v_{Ai}(f)$ represents the Alfvén speed at the footpoints and in our analysis we assume it to be 5×10^4 m s^{-1}. The coronal loop considered here is of length $L = 150$ Mm, that gives us H_1 to be $H_1 \approx 50$ Mm (loop height at the apex). Accordingly the displacement of the apex is 95.48α Mm.

Having defined all quantities, we solve equation (4.7) numerically, for ξ, using the shooting method, assuming that the footpoints of the loop are fixed in the dense photosphere, i.e. $\xi_r = 0$ at $s = 0, L$ or $\xi_r = 0$ at $\alpha = 0$ and $\alpha = \pi$.

The P_1/P_2 period ratio with respect to the displacement parameter α and the ratio $L/(\pi H)$ for coronal conditions ($D = 0.5$) is shown in Figure 4.3 with

the case discussed earlier by, e.g. Andries et al. (2005) corresponding to the value $\alpha = 0.0$.

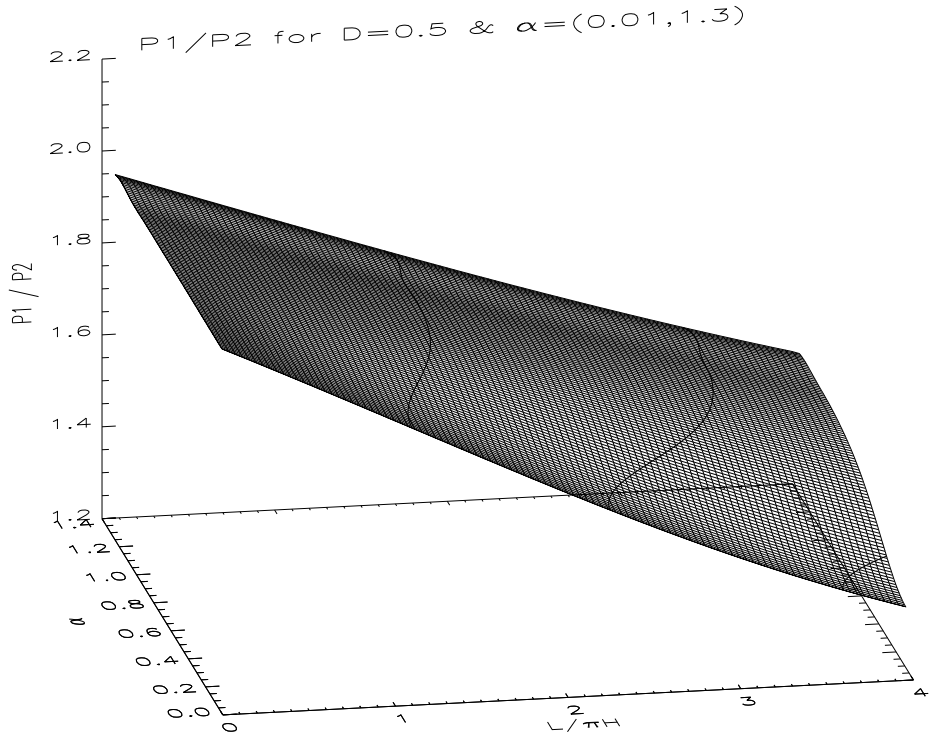

Figure 4.3: The variation of the P_1/P_2 period ratio with parameter α, and the ratio $L/(\pi H)$ for the case of a typical coronal loop (the density ratio here is $D = 0.5$ and half loop length $L = 150$ Mm).

Figure 4.3 shows that the changes in P_1/P_2 period ratio due to the distorsion parameter, α, varied between 0.01 and 1.3. Typically a change of 5% in the period ratio is obtained for approximate values of $L/\pi H = 2$ and $\alpha = 0.6$. Further changes of the order of $10 - 15\%$ can be achieved for rather unrealistic values of $L/\pi H = 4$ and $\alpha = 1.0$ (see Figure 4.4). The relative change was calculated as the percentage change of our results (see, Figure 4.4) compared to the case when $\alpha = 0.0$. In the vicinity of $\alpha = 0.0$, the change is not significant, but as the loop distorsion increases, this difference shows a change in P_1/P_2 of the order of $5 - 8\%$ for values of α from 0.45 to 0.9. The relative change is negative, which means that the P_1/P_2 period ratio, assuming the loop to be

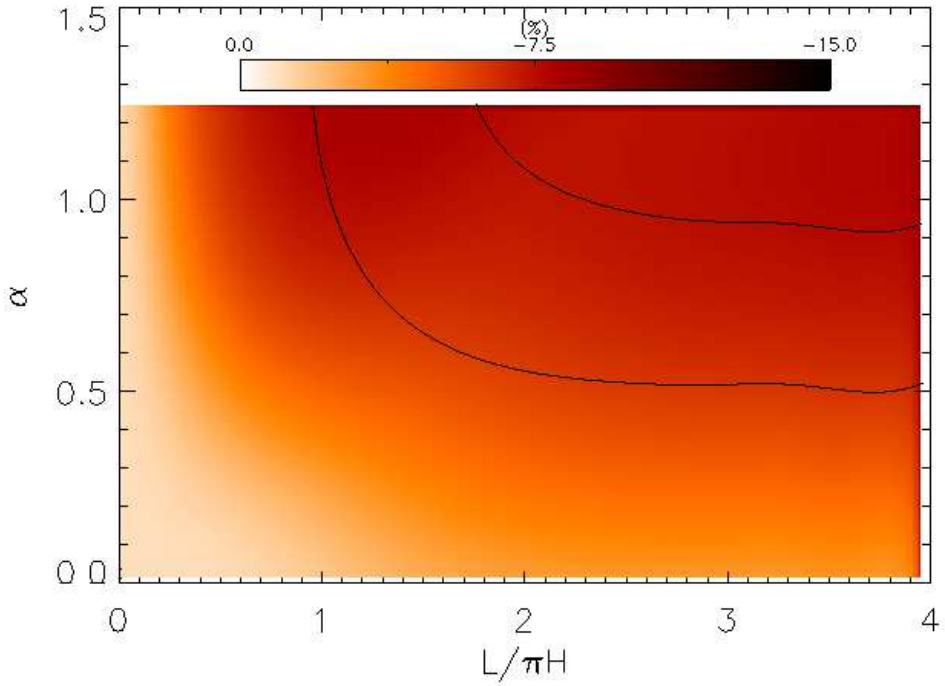

Figure 4.4: The relative variation of the P_1/P_2 period ratio with parameter α, and the ratio $L/(\pi H)$ for the case of a typical coronal loop (the density ratio here is $D = 0.5$ and $L = 150$ Mm). The reference value is obtained for $\alpha = 0.0$.

semi-circular, could be overestimated. The density ratio, D, does not have any important effect of the variation of period ratio, changes brought are of the order of 0.1%.

4.4 Summary

The P_1/P_2 period ratio of transverse fundamental kink mode and its first harmonic is an ideal tool for diagnosing the longitudinal structure of magnetic structures. In this Chapter we investigated the P_1/P_2 ratio for an asymmetric(distorted) coronal loop assuming that the magnetic field and temperature are the same inside and outside the loop, and that the loop dynamics is treated in the cold plasma approximation. We showed that in the case of non semi-

circular coronal loops, the change in the P_1/P_2 period ratio for realistic values is of the order of $5-8\%$. This value can significantly grow to values of over 20% if we assume that there is a temperature difference between the plasma inside and outside the coronal loop, as we saw in Chapter 3. For this analysis, we used the thin flux tube approximation, which allowed us to employ equation (3.1) to describe the dynamics of oscillations. We also supposed the idealistic situation of a static background, however recent analysis by Ruderman (2011) showed that the temporal dependence of density through flow and cooling can also influence the ratio of the two periods.

Our results prove the robustness of seismological techniques developed earlier but also confirm that the effects that significantly influence the P_1/P_2 period ratio are connected to the intrinsic properties of the plasma, i.e. magnetic field structuring, density (and through it, the temperature). Effects such as geometrical (asymmetry, non-circular cross section, non-planaricity, loop curvature) all have limited effect on P_1/P_2.

Chapter 5

Kink oscillations in expanding coronal loops

We investigate the effect of the loop expansion through the solar corona on the period ratio P_1/P_2 and the consequences of the inclusion of the length of the loop as a dynamical parameter on estimations of the degree of density stratification. First we assume that the expansion occurs at the same rate in the vertical and horizontal direction. This motion preserves the initial semi-circular shape of the loop. Later this assumption is relaxed and the properties of kink oscillations will be investigated in a loop that moves so that the initial semi-circular shape transforms gradually into a semi-elliptical loop. The temporal evolution of periods of kink oscillations and their ratio is studied in both cases. The present Chapter is based on the published results of Ballai and Orza (2012).

5.1 Observational facts

The problem of loop emergence and expansion through the solar atmosphere is one of the most challenging topics of solar physics as it involves the analysis of the evolution of the magnetic field in different regions of the solar interior and atmosphere, where conditions can change from region to region. According to the standard theory, the magnetic field produced by the dynamo action in the tachocline is transported through the solar convective zone towards the solar surface by magnetic buoyancy coupled with convective motion (Parker 1955, 1988). Once at the surface, the emerged flux tube creates sunspots and bipolar active regions (Zwaan 1987). In the solar atmosphere the rise of the flux tube continues due to an excess of the magnetic pressure inside the loop (e.g. Archontis et al. 2004). For the purpose of our investigation, we will assume that this excess is balanced at the transition region (TR) and from this height, the expansion is not a driven problem any longer, instead, the loop moves through the corona in the virtue of its inertia. During the emergence and expansion phase, the flux tube can interact with existing magnetic structures in the solar atmosphere, and this might be responsible for the appearance of small-scale (e.g. compact flares, plasmoids, X-point brightenings) and large-scale events (flares and CMEs) as suggested by Archontis (2004). Loop emergence often is associated with strong upflows as observed by, e.g. Harra et al. (2010, 2012).

Since we are interested in the dynamics of a single loop, we will assume that the expansion of the loop through the solar atmosphere takes place in such a way that the reconnection events (or other effects that perturb the morphology and topology of the field lines) do not appear.

It is rather straightforward to imagine what happens with oscillations in a loop when the length of the loop is increasing. As the length of the loop becomes larger, the frequency of oscillations becomes smaller, i.e. the periods of oscillations are expected to grow, however, in an inhomogeneous waveguide, particular periods will be differently affected by the combined effect of inhomogeneity and loop length increase. Therefore, we expect that the period ratio of oscillations will change with the degree of inhomogeneity that also changes with time.

5.2 Mathematical formalism

In our analysis we will capture the dynamical behaviour of the loop once reached the transition region (TR). At this height, the loop can interact with a global blast wave propagating in the low solar corona. This instigator could be easily identified with an EIT wave that propagates in the low corona over very large distances and they are known to be one of the major source for kink oscillations of coronal loops (see, e.g. Ballai 2007). We assume that the height at which the loop starts its journey through the corona is at 3 Mm above the solar surface. A typical loop length is of the order of 300 Mm. For practical reasons, we are going to consider that the height of the loop in its final position would be about 97 Mm resulting in a loop length of about 306 Mm.

The raising speed of loops is generally taken to be 10-15 km s^{-1} (Chou and Zirin 1988, Archiontis 2008), therefore the time needed for the loop to travel the distance from the TR to its steady position is easily estimated to be between 3.4 and 5.2 hours. This time is at least two order of magnitude larger than a typical period of kink oscillations, so there is enough time for the development of oscillations. Higher rising speeds are also possible, recently Schmidt and Ofman (2011) reported expansions of a post-flare loop with speeds of hundreds km s^{-1}. Standing waves are formed if the speed of change in the length of the loop is smaller than the period of oscillations. This condition is easily satisfied for fast kink oscillations. We assume that the loop expands into the 'empty' corona, i.e. it will not encounter any interaction with existing magnetic elements.
In the first instance we assume that the semi-circular shape of the loop at the TR is preserved throughout the expansion. Assuming an initial height of 3 Mm above the surface, the distance between the footpoints of the loop is 6 Mm. When reaching the final height of 97 Mm, the each of the footpoints travel over a distance of 150 Mm. In addition we assume that the expansion occurs at constant temperature (isothermal process). Due to the increase in the volume of the loop, a pressure difference is generated meaning that the plasma flows along magnetic field lines resulting in a density that depends not only on the height, z, but also on time. As it raises through the solar corona, the tangent to the loop is also changing monotonically (see Figure 5.1), therefore the momentum

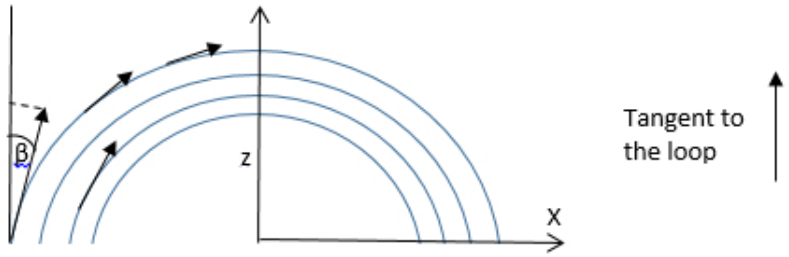

Figure 5.1: The projection on the direction tangent to the loop, where the angle β is a function depending on time and space.

equation in an unperturbed state becomes

$$\rho_0 \frac{\partial u}{\partial t} + \rho_0 u \frac{\partial u}{\partial z} = -\frac{\partial p_0}{\partial z} - g\rho_0 \cos\beta(z,t), \tag{5.1}$$

where the angle β is a function depending on time and space, u is the equilibrium flow of the plasma, ρ_0 and p_0 are the equilibrium density and pressure, and g is the gravitational acceleration.

5.3 Density profile

In coronal loops, the flows are of the order of a few tens of km s^{-1}, therefore in equation (5.1) we can neglect the terms on the left hand side since

$$u\frac{\partial u}{\partial z} \sim \frac{u^2}{L} \approx \frac{10^8}{10^8} = \mathcal{O}(1) = \frac{\partial u}{\partial t},$$

that is two order of magnitude smaller than terms on the right hand side. We can write pressure as

$$p_0(z,t) = \frac{k_B T_0 \rho_0(z,t)}{m},$$

where k_B is the Boltzman constant, T_0 is the constant temperature and m is the mean atomic mass per particle. Introducing this expression into the RHS

of equation (5.1) we obtain that

$$\frac{1}{\rho_0}\frac{\partial \rho_0}{\partial z} + \frac{\cos\beta(z,t)}{H} = 0, \tag{5.2}$$

where H is the constant density scale-height. Focusing on the density distribution inside the loop, we can integrate the above equation to obtain

$$\rho_i = \rho_f \exp\left[-\int_0^z \frac{\cos\beta(z',t)}{H} dz'\right]. \tag{5.3}$$

Assuming that the loop is semicircular we obtain that $\beta(z,t) = \pi z/L(t)$, therefore the density inside the coronal loop becomes

$$\rho_i = \rho_f \exp\left[-\frac{L(t)}{\pi H}\sin\frac{\pi z}{L(t)}\right], \tag{5.4}$$

where ρ_f is the density of the plasma at the footpoint of the loop. For simplicity we will assume that the external density can simply be written as $\rho_e = D\rho_i$, where throughout our calculations we consider $D = 0.5$. Figure 5.2 depicts schematically the change of the equilibrium density, both in space and time. Here length was normalised to the length of the loop at the start of the emergence (considered $L_0 = 3\pi$ Mm) and time (here denoted by τ) was normalised to the quantity $L_0/v_{\rm ris}$, where $v_{\rm ris}$ is the vertical rising speed of the loop considered $v_{\rm ris} = 15$ km s^{-1}. According to our expectations, the density of the loop decreases with time. We assume that the flux tube is thin even at the beginning of its expansion.

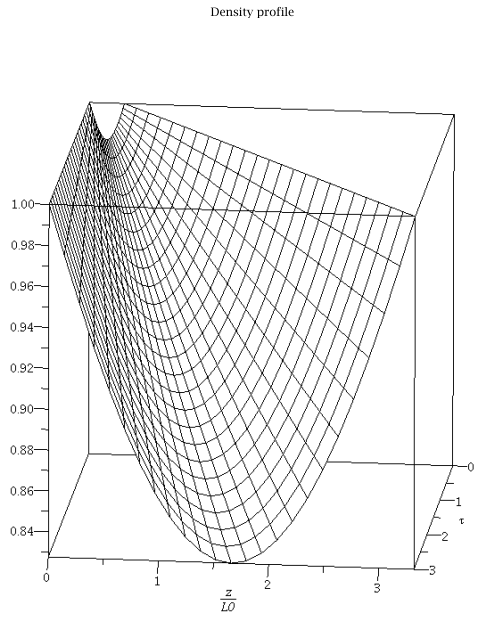

Figure 5.2: A schematic representation of the evolution of the equilibrium density measured on the vertical axis in the units of density at the footpoint. Here lengths are given in units of the loop length at the start of the expansion in the corona (L_0) and time is given in units of $L_0/v_{\rm ris}$, where $v_{\rm ris}$ is the constant rising speed in the vertical direction, here taken to be 15 km s^{-1}

5.4 Kink oscillations of a coronal loop with non-stationary density and plasma flow

We consider that the tube is not expanding in transversal direction, so that the cross-section radius remains constant and equal to a constant a. The plasma density in the tube and in the surrounding plasma can vary along the tube z and with time t. For cylindrical coordinates (r, φ, z) with the z-axis coinciding with the tube axis the unperturbed density is $\rho(z,t)$. Initially, there is a plasma flow along the tube with the velocity $U(z,t)$.

Here we do not take into account physical processes that cause the density variation, so we don't use the momentum and energy equations for the unperturbed quantities. The unperturbed magnetic field is everywhere in the z -

direction and has constant magnitude $B_0(z,t)$.
Let us consider the perturbed quantities of magnetic field $\mathbf{B}$ and velocity $\mathbf{u}$,

$$\mathbf{B} = \mathbf{B}_0(z,t) + \mathbf{B}_1(r,\varphi,z,t),$$

$$\mathbf{u} = \mathbf{u}_0 + \mathbf{u}_1(r,\varphi,z,t)$$

where the perturbation of velocity $\mathbf{u}_1$ has the components $\mathbf{u}_1 = (v_r, v_\varphi, v_z)$ and the components of the perturbation of magnetic field $\mathbf{B}_1$ are $\mathbf{B}_1 = (b_r, b_\varphi, b_z)$. To describe the plasma motion we use the ideal linearised MHD equations for a cold plasma, i.e.

$$\frac{\partial \mathbf{u}_1}{\partial t} + (\mathbf{U}\cdot\nabla)\mathbf{u}_1 + (\mathbf{u}_1\cdot\nabla)\mathbf{U} = \frac{1}{\mu_0\rho}\left[(\nabla\times\mathbf{B}_1)\times\mathbf{B}_0 + (\nabla\times\mathbf{B}_0)\times\mathbf{B}_1\right], \quad (5.5)$$

$$\frac{\partial \mathbf{B}_1}{\partial t} = \nabla\times(\mathbf{u}_1\times\mathbf{B}_0 + \mathbf{u}_1\times\mathbf{B}_1), \quad (5.6)$$

$$\nabla\cdot\mathbf{B}_1 = 0. \quad (5.7)$$

along with the mass conservation equation,

$$\frac{\partial\rho}{\partial t} = \frac{\partial(\rho U)}{\partial z} = 0. \quad (5.8)$$

From equation (5.5) with $\mathbf{B}_0(z,t)$, $\mathbf{U}(z,t)$ we obtain that $v_z = 0$.

At the tube boundary the dynamic and kinematic boundary conditions have to be satisfied. The linearized dynamic boundary condition is that the perturbation of the magnetic pressure, $P = B_0 b_z/\mu_0$, has to be continuous,

$$[P] = 0 \text{ at } r = a, \quad (5.9)$$

where $[f]$ indicates the jump of a function f across the boundary.

If we take the equation of the perturbed tube boundary to be $r = a + \eta(t,\varphi,z)$, then the linearized kinematic boundary condition becomes

$$v_r = \frac{\partial\eta}{\partial t} + U\frac{\partial\eta}{\partial z} \text{ at } r = a. \quad (5.10)$$

Since the tube surface is tangential discontinuity, the normal component of the magnetic field at the tube surface is zero. This condition can be written as

$$b_r - B_0 \frac{\partial \eta}{\partial z} = 0 \text{ at } r = a. \tag{5.11}$$

The boundary condition (5.11) follows from (5.10) using equation (5.6). We used the fact that the magnetic field lines are frozen in the dense photospheric plasma to obtain the boundary conditions at $z = 0, L$. When there is no equilibrium flow these conditions become $\mathbf{u}_1 = 0$. In the presence of equilibrium flow they become more complicated. In ideal MHD, the electrical field, $\mathbf{E}$, is given by

$$\mathbf{E} = -(\mathbf{U} + \mathbf{u}_1) \times (\mathbf{B}_0 + \mathbf{B}_1). \tag{5.12}$$

In the regions $z < 0$ and $z > L$ the magnetic field lines are straight and plasma will flow along the magnetic field lines, so $\mathbf{E} = 0$ in these regions, which implies that $\mathbf{E}_r = 0$ at $z = 0, L$. Then, linearizing these boundary conditions and taking into account that both $\mathbf{U}$ and $\mathbf{B}_0$ are parallel to the z - direction, we immediately obtain that

$$B_0 \mathbf{u}_1 - U(\mathbf{B}_1 - \mathbf{e}_z bz) = 0 \text{ at } z = 0, L, \tag{5.13}$$

Since the tube boundary consists of magnetic field lines which are frozen in the dense plasma in the regions $z \leq 0$ and $z \geq L$, it follows that

$$\eta = 0 \; at \; z = 0, L. \tag{5.14}$$

This condition is consistent with (5.13) and (5.10).

The system of equations (5.5)-(5.7) can be transformed into

$$\frac{\partial \mathbf{u}_1}{\partial t} + U \frac{\partial \mathbf{u}_1}{\partial z} = -\frac{1}{\rho} \nabla \mathbf{P} - \mathbf{e}_z \frac{\partial \mathbf{P}}{\partial z} + \frac{\mathbf{B}_0}{\mu_0 \rho} \frac{\partial \mathbf{B}_{1\perp}}{\partial z}, \tag{5.15}$$

$$\frac{\partial \mathbf{B}_{1\perp}}{\partial t} + \frac{\partial (U \mathbf{B}_{1\perp})}{\partial z} = \mathbf{B}_0 \frac{\partial \mathbf{u}_1}{\partial z}, \tag{5.16}$$

5.4

$$\frac{\partial \mathbf{P}}{\partial z} = -\frac{\mathbf{B}_0}{\mu_0}\nabla_\perp \cdot \mathbf{B}_{1\perp}. \tag{5.17}$$

where the perpendicular component of magnetic field perturbation is defined as

$$\mathbf{B}_{1\perp} = \mathbf{B}_1 - \mathbf{e}_z b_z,$$

and the perpendicular gradient operator $\nabla_\perp$ is

$$\nabla_\perp = \nabla - \mathbf{e}_z \frac{\partial}{\partial z}.$$

The characteristic spatial scale of variation of all variables in the z- direction is L and in the r - direction is a. Since the tube is thin, $a/L = \epsilon \ll 1$. To take this difference into account one can introduce the stretching variable $\sigma = \epsilon^{-1} r$. Further, eliminating $\mathbf{u}_1$ from equations (5.15) and (5.16), we obtain

$$\left(\frac{\partial}{\partial t} + \frac{\partial}{\partial z}U\right)^2 \mathbf{B}_{1\perp} - \frac{\partial}{\partial z}\left(V_A^2 \frac{\partial \mathbf{B}_{1\perp}}{\partial z}\right) = -\epsilon^{-1}\frac{\partial}{\partial z}\left(\frac{\mathbf{B}_0}{\rho}\tilde{\nabla}_\perp \mathbf{P}\right), \tag{5.18}$$

with $\tilde{\nabla}_\perp = \epsilon \nabla_\perp$. Equation (5.18), in particular, implies that $P \sim \epsilon(B_0/mu_0)/|\mathbf{B}_{1\perp}|$. The ratio of the left-hand side of equation (5.17) to is right-hand side is of the order of ϵ^2, which implies that we can neglect the left-hand side of equation (5.17) when comparing it to the right-hand side, reducing it to

$$\tilde{\nabla}_\perp \cdot \mathbf{B}_{1\perp} = 0. \tag{5.19}$$

Appying the operator $\tilde{\nabla}_\perp \cdot$ to equation (5.16) and using (5.19) we obtain

$$\frac{\partial}{\partial z}\tilde{\nabla}_\perp \cdot \mathbf{u}_1 = 0. \tag{5.20}$$

Applying $\tilde{\nabla}_\perp \cdot$ to equation (5.11) and use (5.19) we obtain

$$\tilde{\nabla}_\perp \cdot \mathbf{u}_1 = 0 \; z = 0, L \tag{5.21}$$

From equations (5.20) and (5.21) it follows that

$$\tilde{\nabla}_{\perp} \cdot \mathbf{u}_1 = 0. \tag{5.22}$$

Next, applying the same operator to equation (5.15) rewritten in terms of the new independent variable σ and using equations (5.19) and (5.22) results in

$$\tilde{\nabla}_{\perp}^2 \mathbf{P} = 0. \tag{5.23}$$

If we consider the kink oscillations and take only perturbation of all variables proportional with $\exp(i\varphi)$, equation (5.23) reduces to

$$r\frac{\partial}{r}\partial r\frac{\partial P}{\partial r} - P = 0. \tag{5.24}$$

Note for the above result we used the stretching variable σ to neglect small terms. The solution to equation (5.24) is regular inside the tube, decaying far from the tube and satisfying boundary condition (5.9) is

$$P = f(t,z)r,\ r < a; \quad P = f(t,z)a^2/r,\ r > a. \tag{5.25}$$

with $f(t,z)$ an arbitrary function.

Writing the r-component of equation (5.15) at the tube boundary inside and outside the tube and use equation (5.25) we obtain

$$\frac{\partial v_{ri}}{\partial t} + \mathbf{U}_i\frac{\partial v_{ri}}{\partial z} = -\frac{f}{\rho_i} + \frac{\mathbf{B}_0}{\mu_0\rho_i}\frac{\partial b_{ri}}{\partial z} \tag{5.26}$$

$$\frac{\partial v_{re}}{\partial t} + \mathbf{U}_e\frac{\partial v_{re}}{\partial z} = \frac{f}{\rho_e} + \frac{\mathbf{B}_0}{\mu_0\rho_e}\frac{\partial b_{re}}{\partial z} \tag{5.27}$$

Since $b_{ri} = b_{re}$ with multiplying equation (5.26) by ρ_i, equation (5.27) by ρ_e, adding the results and using equations (5.10) and (5.11) we arrive at an equation for η.

$$\rho_i\left(\frac{\partial}{\partial t} + U_i\frac{\partial}{\partial z}\right)^2\eta + \rho_e\left(\frac{\partial}{\partial t} + U_e\frac{\partial}{\partial z}\right)^2\eta - \frac{2B^2}{\mu_0}\frac{\partial^2\eta}{\partial z^2} = 0, \tag{5.28}$$

an equation describing the displacement of the tube axis. Since we canceled out the dependence on φ by assuming that the perturbations of all variables are proportional to $exp(i\varphi)$ this implies that $\eta(z,t)$ is a complex-valued function, i.e. $\eta = \eta_R + i\eta_I$. For a real value function we need to take $\mathcal{R}(\eta)$ instead of η, that leads to

$$\eta = \eta_R \cos\varphi - \eta_I \sin\varphi.$$

In Cartesian coordinates the loop's displacement in the $x = r\cos\varphi$ and $y = r\sin\varphi$ directions, ξ_x and ξ_y, are given by (see, e.g. Ruderman 2010)

$$\xi_x = \eta_R, \quad \xi_y = -\eta_I.$$

We assume a quasi-stationary equilibrium, so that the characteristic time variation of equilibrium quantities (t_{ch}) is much longer than the period of kink oscillations (P) and introduce the small parameter $\epsilon \ll 1$ so that $P = \epsilon t_{ch}$. Using the definition of the period of oscillations we can write

$$\frac{L(\mu_0\rho_{ch})^{1/2}}{B_0} = \epsilon t_{ch} \Longrightarrow B_0 = \epsilon^{-1}\frac{L(\mu_0\rho_{ch})^{1/2}}{t_{ch}}, \tag{5.29}$$

meaning that we can introduce a scaled magnetic field, so that $\tilde{B}_0 = \epsilon B_0$. As a result, the equation describing the dynamics of the kink oscillations can be written as

$$\rho_i\left(\frac{\partial}{\partial t} + U_i\frac{\partial}{\partial z}\right)^2\eta + \rho_e\left(\frac{\partial}{\partial t} + U_e\frac{\partial}{\partial z}\right)^2\eta - \frac{2\epsilon^{-2}\tilde{B}^2}{\mu_0}\frac{\partial^2\eta}{\partial z^2} = 0. \tag{5.30}$$

The above equation must be solved subject to the standard boundary conditions (5.14), i.e.

$$\eta(z=0, z=L) = 0.$$

Following the solution method proposed by Ruderman (2011a), we will solve equation (5.30) using the Wentzel-Kramers-Brillouin (WKB) method (see, e.g. Bender and Országh 1987) and assume that the solution of the equation will be

of the form

$$\eta = \sum_{k=0}^{\infty} \epsilon^k S_k(z,t) \exp\left[\frac{i}{\epsilon}\Phi(t)\right]. \tag{5.31}$$

Expanding S in series

$$S = S_0 + \epsilon S_1 + ..., \tag{5.32}$$

substituting equations (5.31) and (5.32) into equation (5.30), and collecting terms of the order of ϵ^{-2} we obtain

$$\frac{\partial^2 S_0}{\partial z^2} + \frac{\Omega^2}{\tilde{c}_k^2} S_0 = 0, \tag{5.33}$$

where

$$\Omega = \frac{d\Phi(t)}{dt}, \quad \tilde{c}_k^2 = \frac{2\tilde{B}^2}{\mu_0[\rho_i(z,t) + \rho_e(z,t)]}.$$

This approximation is sometimes called the approximation of geometrical optics. Equation (5.33) must be solved subject to the boundary condition $S_0 = 0$ when $z = 0$ and $z = L$. Equation (5.33) together with the line-tying condition form an eigenvalue problem in which Ω is the eigenvalue and Ω^2 is a real function.

In the next order of approximation (also called the approximation of physical optics), we collect the terms of the order of ϵ^{-1} and equation (5.30) reduces to

$$\frac{\partial^2 S_1}{\partial z^2} + \frac{\Omega^2}{\tilde{c}_k^2} S_1 = \frac{2i\Omega}{\tilde{c}_k^2}\left[\frac{\partial S_0}{\partial t} + \frac{S_0}{2\Omega}\frac{d\Omega}{dt} + \frac{\rho_i U_i + \rho_e U_e}{\rho_i + \rho_e}\frac{\partial S_0}{\partial z}\right], \tag{5.34}$$

that has to be solved subject to the boundary condition $S_1(z = 0, z = L) = 0$. The boundary-value problem determining S_1 has a solution only when the RHS of equation (5.34) satisfies the compatibility condition, i.e. the orthogonality to S_0. After multiplying the RHS of equation (5.34) by S_0 and integrating with respect to z in the interval $(0, L)$ we obtain (similar to Ruderman 2011a) that the compatibility condition reduces to

$$\omega \int_0^L \frac{S_0^2}{c_k^2} dz = const., \tag{5.35}$$

where

$$\omega = \epsilon^{-1}\Omega, \quad c_k = \epsilon^{-1}\tilde{c}_k.$$

As a consequence, the dynamics of kink oscillations in coronal loops is fully described by the system of equations (5.33) and (5.35). In deriving equation (5.35) we took into account the mass conservation equation, relating the plasma flow and its density

$$\frac{\partial \rho}{\partial t} + \frac{\partial (\rho U)}{\partial z} = 0.$$

5.5 Time dependent density

This density profile would correspond to an initial expansion of the loop when the height of the loop is less than the scale-height (assuming expansion into an isothermal 1 MK corona, this height would correspond to 47 Mm). In this case, we may expect that the amplitude of oscillations increases as the loop expands.

The function $S_0 = A(t)\sin(\pi z/L(t))$ is a solution for equation (5.33). Were by $A(t)$ we refer to the amplitude of oscillations at a given time t. Using equation (5.35) we find the following relation,

$$\frac{\omega}{2}\frac{A^2(t)}{c_K^2(t)}L(t) = ct.$$

where $\omega = \pi c_K(t)/L(t)$, so the relation simplifies into

$$\frac{\pi}{2}\frac{A^2(t)}{c_K(t)} = ct.$$

Rewriting this into a different form we obtain the following statement

$$\frac{A^2(t)}{c_K(t)} = \frac{A^2(0)}{c_K(0)}$$

Hence, the amplitude of oscillations behaves like

$$A(t) = A(0)\left(\frac{c_k(t)}{c_k(0)}\right)^{1/2} = A(0)\left(\frac{L(t)}{L(0)}\right)^{1/2} \tag{5.36}$$

where $A(0)$, $c_k(0)$ and L_0 are the amplitude of oscillations, the kink speed and the length of the loop at $t = 0$.

A particular case to discuss is when the expansion of the loop occurs linearly with time and we write that

$$L(t) = L_0 + v_{\rm ris} t \tag{5.37}$$

where L_0 is the length of the loop at the initial time and $v_{\rm ris}$ is the rising speed, i.e. at the TR level ($L_0 = 3\pi$ Mm) and v_r is the rising speed, here assumed constant. Accordingly, the kink speed becomes

$$c_k^2 = c_{kf}^2 \exp\left[\frac{L_0 + \pi v_{\rm ris} t}{\pi H} \sin \frac{\pi z}{L_0 + v_r t}\right] \tag{5.38}$$

where

$$c_{kf}^2 = \frac{2B^2}{\mu_0 \rho_f (1+D)}.$$

Returning to the general case, the equations describing the dynamics of kink oscillations are

$$\frac{\partial^2 S_0}{\partial z^2} + \frac{\omega^2}{{c_k}^2} S_0 = 0, \quad \omega \int_0^L \frac{S_0^2}{c_k^2} dz = const. \tag{5.39}$$

Let us introduce a new set of dimensionless quantities

$$\xi = \frac{z}{L_0}, \;\; \tau = \frac{\pi v_{\rm ris} t}{L_0}, \;\; \tilde{\omega} = \frac{\omega L_0}{c_{kf}}, \;\; \tilde{S}_0 = \frac{S_0}{L_0}. \tag{5.40}$$

In the new variables the equations to be solved transform into

$$\frac{\partial^2 \tilde{S}_0}{\partial \xi^2} + \exp\left[\frac{-L_0(1+\tau)}{\pi H} \sin \frac{\pi \xi}{1+\tau}\right] \tilde{\omega}^2 \tilde{S}_0 = 0, \tag{5.41}$$

and

$$\tilde{\omega} \int_0^{1+\tau} \tilde{S}_0^2 \exp\left[\frac{-L_0(1+\tau)}{\pi H} \sin \frac{\pi \xi}{1+\tau}\right] d\xi = const. \tag{5.42}$$

that should be solved subject to the boundary conditions $S_0(\xi = 0; \xi = 1+\tau) = 0$. The solution of equation (5.41) can be found numerically using, e.g. the shooting method. In Figure 5.3 we display first the variation of periods of oscillations of the fundamental mode and its first harmonic for three different values

5.5

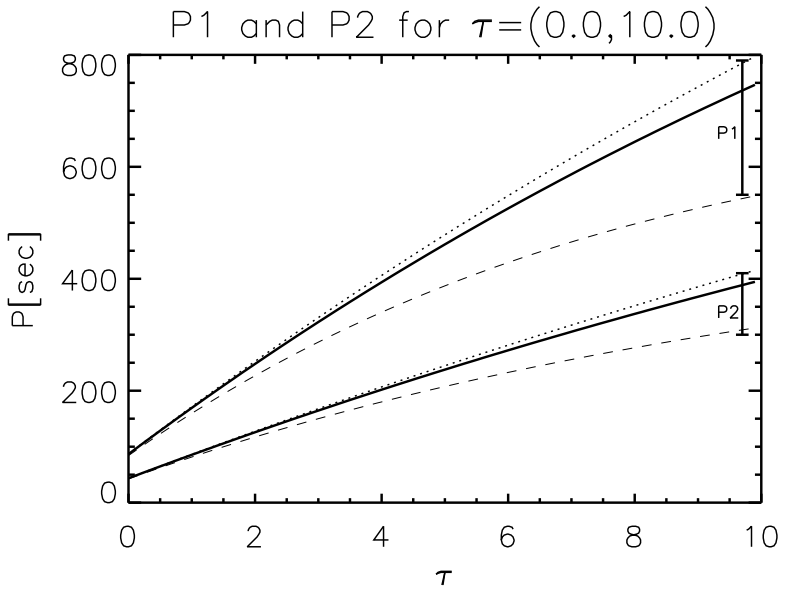

Figure 5.3: The variation of the periods of the fundamental mode and its first harmonic with the dimensionless time variable τ for three different values of stratification: H=70.5 Mm (dotted line), H=47 Mm (solid line), and H=23.5 Mm (dashed line)

of H in terms of the dimensionless time variable, τ. The bands for each period are clearly labeled in the figure. The three distinct value of periods were obtained for three values of scale-height keeping the initial length of the loop at 3π Mm. The dotted line represents the case of a scale-height of 70.5 Mm, which, assuming a plasma in hydrostatic equilibrium, would correspond to a plasma temperature of 1.5 MK. The solid line is plotted for a loop expanding into a corona where the constant scale-height is 47 Mm, that would correspond to a 1 MK hot plasma. Finally, the dashed line stands for an expansion of the loop into a plasma where the density scale-height is 23.5 Mm, corresponding to a plasma temperature of 0.5 MK. The two bands for the periods clearly show that the two oscillations are differently affected by the expansion, i.e. change in the length of the loop. This is also obvious in Figure 5.4 where we plotted the ratio of the periods of the fundamental and first harmonic as a function of the time variable, τ. The plot clearly shows that the oscillations of a loop expanding into a 'hot' plasma (i.e. large scale-height) are the least affected, but in all three cases the

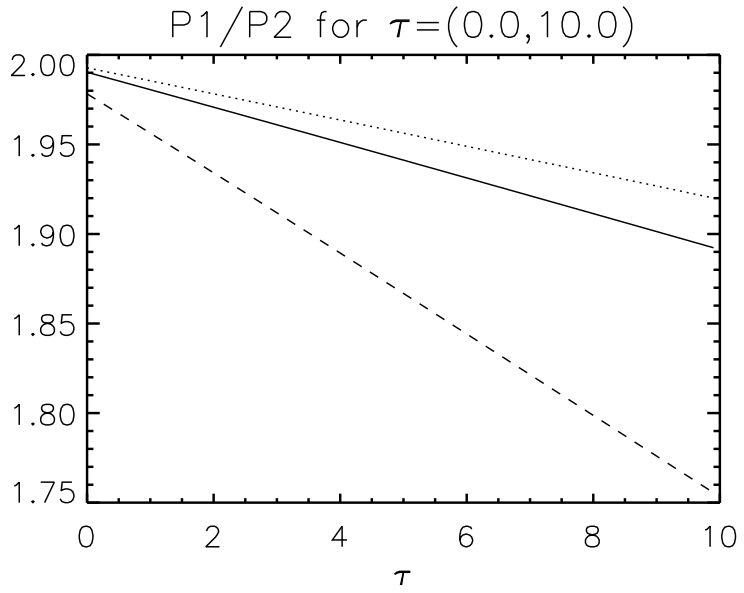

Figure 5.4: The variation of the P_1/P_2 period ratio with respect to the dimensionless parameter τ, for a loop expanding in the solar corona with persisting semi-circular shape. The meaning of each line-style is identical to Figure 5.3.

period ratio decreases with time. We should note here that the periods shown in Figure 5.4 do not start at the value of 2 because at the start of their expansion through the solar corona, loops are already stratified and the least stratified is the case that corresponds to $H = 1.5$ MK. Let us make a final note: in observations, the identification of periods in coronal loops is a dynamical process. i.e. in EUV the intensity is measured in one location (or mega-pixel to reduce errors) for a long time-period. The duration of observation vary, and mostly they are driven either by the availability of the instrument or by the limited life-time of oscillations before they are damped by, e.g. resonant absorption, although observations show that not all loop oscillations damp (probably these oscillations are maintained by a constant lateral buffeting). Typically, for damped oscillations, the detection time is a few periods with a range of 6.7-90 minutes (Aschwanden 2004). In terms of the dimensionless quantity τ, this range would correspond to $\tau = 0.64 - 8.6$. Although the lower limit is too small to count in the effect of expansion, a duration of $\tau = 8.6$ would add an important effect in

studying the transverse kink oscillations. Figure 5.4 shows that for one given value of internal structuring, the value of the period ratio can change also because of the expansion of the loop. Although the periods shown in Figure 5.3 display a monotonic increase with the parameter τ, in reality these values will saturate, the saturation occurring faster for those modes that propagate in a highly structured plasma (e.g. for the case of H=23.5 Mm, the saturation value of periods is about 400 seconds and the saturation starts at about $\tau = 20$). In addition, the period ratio for all cases discussed here tend to same value (near 1) for large values of τ. We need to mention here the very important fact that the effect of increase on the periods of oscillations and the decrease of the period ratio is relevant only in the expansion phase of the loop.
Analytical solutions of the equations. (5.41) can be obtained for the limiting case of a loop at the beginning of its expansion through the solar corona, i.e. small values of τ, see Section 5.7.

5.6 Solutions to the wave equation in the case of the loop at the beginning of its expansion

An interesting insight into the character of the solution of the governing equation can be obtained analytically in the limiting case of

$$\zeta = L_0(1+\tau)/\pi H \ll 1,$$

i.e. we restrict ourself to the first part of the emergence into the solar corona. In this case the argument of the exponential function in equation (5.41) can be expanded (keeping only the first two terms) and the equation to be solved reduces to

$$\frac{\partial^2 \tilde{S}_0}{\partial \xi^2} + \tilde{\omega}^2 \tilde{S}_0 = -\sin\frac{\pi\xi}{1+\tau}\zeta\tilde{S}_0, \tag{5.43}$$

Since we are looking for periodic solutions and we expect that both the amplitude and frequency will depend on time, we will employ the Poincaré-Lindstedt

method (Meirovitch 1970) to find corrections to the eigenfunctions and eigenfrequencies (it can be shown that this method is similar to the re-normalization technique used by Ballai et al 2007 in the case of dispersive shocks). We are looking for solutions in the form of series and write

$$\tilde{S}_0 = \sum_{k=1}^{\infty} \zeta^k \tilde{S}_0^{(k)}, \quad \tilde{\omega} = \sum_{k=1}^{\infty} \zeta^k \tilde{\omega}^{(k)}, \tag{5.44}$$

where the functions S_i are periodic functions. We first concentrate on the fundamental mode. After inserting the expansions (5.44) into the governing equation (5.43), we collect terms proportional to subsequent powers of ζ. In the first order of approximation, collecting terms $\sim \mathcal{O}(\zeta^0)$, results in

$$\frac{\partial^2 \tilde{S}_0^{(0)}}{\partial \xi^2} + \tilde{\omega}^{(0)2} \tilde{S}_0^{(0)} = 0. \tag{5.45}$$

Solving this equation, subject to the mentioned boundary conditions, yields in the case of the fundamental mode

$$\tilde{S}_0^{(0)} \sim \sin \frac{\pi \xi}{1+\tau}, \quad \tilde{\omega}^{(0)} = \frac{\pi}{1+\tau}. \tag{5.46}$$

In the next order of approximation (i.e. terms $\sim \mathcal{O}(\zeta)$) we obtain

$$\frac{\partial^2 \tilde{S}_0^{(1)}}{\partial \xi^2} + \tilde{\omega}^{(0)2} \tilde{S}_0^{(1)} = -\frac{\pi^2}{(1+\tau)^2} \sin^2 \frac{\pi \xi}{1+\tau} -$$

$$-\frac{2\pi}{1+\tau} \tilde{\omega}^{(1)} \sin \frac{\pi \xi}{1+\tau}, \tag{5.47}$$

that has to be solved subject to the boundary conditions

$$\tilde{S}_0^{(1)}(\xi = 0, \xi = 1+\eta) = 0. \tag{5.48}$$

The last term in equation (5.47) will cause secular growth of the solution, therefore rendering the solution S_1 non-periodic. To suppress this possibility, we choose $\tilde{\omega}_1 = 0$. As a result, the solution of equation (5.47) together with the

boundary conditions is simply written as

$$\tilde{S}_0^{(1)} \sim \sin\frac{\pi\xi}{1+\tau} + \frac{3}{2}\cos\frac{\pi\xi}{1+\tau} - \frac{1}{6}\left(3+\cos\frac{2\pi\xi}{1+\tau}\right). \tag{5.49}$$

In the next order of approximation we collect terms $\mathcal{O}(\zeta^2)$ and obtain

$$\frac{\partial\tilde{S}_0^{(2)}}{\partial\xi} + \tilde{\omega}^{(0)2}\tilde{S}_0^{(2)} = -\tilde{\omega}^{(0)2}\tilde{S}_0^{(1)}\sin\left(\frac{\pi\xi}{1+\tau}\right) - 2\tilde{\omega}^{(0)}\tilde{\omega}^{(1)}\tilde{S}_0^{(0)}. \tag{5.50}$$

Using the expression of $\tilde{\omega}^{(0)}$, $\tilde{S}_0^{(0)}$ and $\tilde{S}_0^{(1)}$ determined earlier, the RHS of the above equation can be written as

$$\text{RHS} = \left[\frac{\pi^2}{3(1+\tau)^2} - \frac{2\pi\tilde{\omega}^{(2)}}{1+\tau}\right]\sin\frac{\pi\xi}{1+\tau} + A\sin^2\frac{\pi\xi}{1+\tau} + B\sin\frac{2\pi\xi}{1+\tau} + C\sin\frac{3\pi\xi}{1+\tau}, \tag{5.51}$$

where the coefficients of higher harmonics (A, B and C) are not needed for our discussion. In order to prevent non-periodic behaviour we need to impose the condition that the coefficient of the first term is zero, leading to

$$\tilde{\omega}^{(2)} = \frac{\pi}{6(1+\tau)}. \tag{5.52}$$

As a result, the eigenfunction and eigenfrequency of fundamental mode oscillations can be written as

$$\tilde{S}_0 = \sin\frac{\pi\xi}{1+\tau} + \zeta\left[\frac{3}{2}\cos\frac{\pi\xi}{1+\tau} - \frac{1}{6}\left(3+\cos\frac{2\pi\xi}{1+\tau}\right)\right],$$

$$\tilde{\omega} = \frac{\pi}{1+\tau} + \zeta^2\frac{\pi}{6(1+\tau)}, \tag{5.53}$$

meaning that the change in the frequency due to expansion is a second order effect. It is easy to show that the period of the fundamental mode in this

approximation can be written as

$$P_1 = \frac{12(1+\tau)}{6+\zeta^2}, \tag{5.54}$$

proving the increase of the period P_1 with τ seen in Fig 5.3.

Repeating the same method for the first harmonic, where the eigenfunction and eigenfrequency in the zeroth-order approximation are

$$\tilde{S}_0 = \sin\frac{2\pi\xi}{1+\tau}, \quad \tilde{\omega}^{(0)} = \frac{2\pi}{1+\tau},$$

we obtain that

$$\tilde{\omega} = \frac{2\pi}{1+\tau} + \zeta^2\frac{2\pi}{15(1+\tau)}, \tag{5.55}$$

meaning that the period of the first harmonic in this approximation behaves like

$$P_2 = \frac{15(1+\tau)}{15+\zeta^2}, \tag{5.56}$$

showing an increasing tendency with respect to τ. Now, using equations (5.54) and (5.56) we can calculate the period ratio of the fundamental mode and its first harmonic as

$$\frac{P_1}{P_2} \approx 2\left(1-\frac{\zeta^2}{60}\right) = 2\left[1-\frac{L_0^2(1+\tau)^2}{60\pi^2H^2}\right], \tag{5.57}$$

so that the change in the period ratio is very small but decreases with ζ.

The results confirm the tendency of periods to increase with time and of the period ratio to decrease with time.

5.7 Non-circular emergence

In reality, the expansion of a loop in the empty corona so that the semi-circular shape is preserved is unlikely since the footpoints have to move in a much denser plasma than the apex of the loop. That is why in this section we will assume that the expansion rate in the vertical direction is larger than the expansion of footpoints in the horizontal direction. The expansion still starts at the TR level where the shape of the loop is semi-circular and assume that the process remains isothermal. As a result of different expansion rates, the loop evolves so that the shape becomes more elliptical. The properties of transverse loop oscillations in an elliptical coronal loop were studied recently by Morton and Erdélyi (2009) assuming that the semi-elliptical shape is reached in the emerging stage, before reaching a semi-circular shape. They found that the difference in P_1/P_2 period ratio between the circular and elliptical shape is up to 6%.

Since the dynamics is going to be different over the two directions, it is more convenient to introduce a polar coordinate system in which

$$x = a(t)\cos\theta, \quad z = b(t)\sin\theta, \tag{5.58}$$

with $\dot{a}(t) < \dot{b}(t)$, the over-dot denoting the derivative with respect to time. The length of the loop is covered by the parameter θ that varies now between 0 and π. It is more convenient to use the coordinate along the loop, s, therefore the dynamics of transverse kink oscillations is described by

$$\rho_i \left(\frac{\partial}{\partial t} + U_i \frac{\partial}{\partial s}\right)^2 \eta + \rho_e \left(\frac{\partial}{\partial t} + U_e \frac{\partial}{\partial s}\right)^2 \eta - \frac{2B^2}{\mu_0}\frac{\partial^2 \eta}{\partial s^2} = 0, \tag{5.59}$$

A key parameter in our discussion is going to be the arc-length that is defined as

$$\frac{\partial s}{\partial \theta} = \sqrt{a(t)^2 \sin^2\theta + b(t)^2 \cos^2\theta} = \alpha(\theta, t). \tag{5.60}$$

In order to solve equation (5.59) we would need to express the density as function of s and t. However, it turns out that it is much easier to deal with the variable

θ instead. Therefore we express the derivatives in the governing equation as

$$\frac{\partial}{\partial s}=\frac{1}{\alpha}\frac{\partial}{\partial \theta},\quad \frac{\partial^2}{\partial s^2}=\frac{1}{\alpha^2}\frac{\partial^2}{\partial \theta^2}-\frac{\sin 2\theta(a(t)^2-b(t)^2)}{2\alpha^4}\frac{\partial}{\partial \theta}. \tag{5.61}$$

Assuming again a quasi-stationary equilibrium, similar as in the previous section, and introducing the small parameter, ϵ, in the same way as presented in equation (5.6) the governing equation for transverse kink oscillations can be written as

$$\frac{\partial^2\eta}{\partial t^2}+\frac{2}{\alpha}\left(\frac{\rho_i U_i+\rho_e U_e}{\rho_i+\rho_e}\right)\frac{\partial^2\eta}{\partial\theta\partial t}+\frac{1}{\alpha^2}\left[\frac{\rho_i U_i^2+\rho_e U_e^2}{\rho_i+\rho_e}-\right.$$

$$\left.\frac{2\epsilon^{-2}B_0^2}{\mu_0(\rho_i+\rho_e)}\right]\frac{\partial^2\eta}{\partial\theta^2}-\left[2\frac{\rho_i U_i+\rho_e U_e}{\rho_i+\rho_e}\frac{a\dot{a}\sin^2\theta+b\dot{b}\cos^2\theta}{\alpha^3}+\right.$$

$$+\frac{\rho_i U_i^2+\rho_e U_e^2}{\rho_i+\rho_e}\frac{\sin 2\theta(a(t)^2-b(t)^2)}{2\alpha^4}-$$

$$\left.2\frac{\epsilon^{-2}B_0^2}{\mu_0(\rho_i+\rho_e)}\frac{\sin 2\theta(a(t)^2-b(t)^2)}{2\alpha^4}\right]\frac{\partial\eta}{\partial\theta}=0, \tag{5.62}$$

that has to be solved subject to the boundary conditions $\eta(\theta=0,\theta=\pi)=0$.

Again, we will solve this equation using the WKB approximation presented earlier and suppose a solution of the form

$$\eta=\sum_{k=0}^{\infty}\epsilon^k S_k(\theta,t)\exp\left[\frac{i}{\epsilon}\Phi(\theta)\right]. \tag{5.63}$$

In the first order of approximation equation (5.62) reduces to

$$\frac{\partial^2 S_0}{\partial\theta^2}-\frac{\sin 2\theta(a^2-b^2)}{2\alpha^2}\frac{\partial S_0}{\partial\theta}+\frac{\alpha^2\Omega^2}{\tilde{c}_K^2}S_0=0, \tag{5.64}$$

together with the usual boundary conditions at the two ends of the loop. In the next order of approximation we obtain

$$\frac{\partial^2 S_1}{\partial\theta^2}-\frac{\sin 2\theta(a^2-b^2)}{2\alpha^2}\frac{\partial S_1}{\partial\theta}+\frac{\alpha^2\Omega^2}{\tilde{c}_k^2}S_1=$$

$$= \frac{2i\alpha\Omega}{\tilde{c}_k^2}\left[\frac{\partial S_0}{\partial t} + \frac{\alpha S_0}{2\Omega}\frac{\partial \Omega}{\partial t} + \frac{\rho_i U_i + \rho_e U_e}{\rho_i + \rho_e}\frac{\partial S_0}{\partial \theta}\right]. \tag{5.65}$$

This equation has to be solved subject to the boundary condition $S_1(\theta = 0, \theta = \pi) = 0$. Again, the equation for S_1 will have solution if the right-hand side of the above equation satisfies the compatibility condition, i.e. the orthogonality to S_0. Following the same solving procedure as presented earlier, it is easy to show that the compatibility condition reduces to

$$\omega_\alpha \int_0^\pi \frac{S_0^2}{c_k^2}\, d\theta = 0 \tag{5.66}$$

Therefore, the system of equations (5.64) and (5.66) will determine completely the dynamics of the expanding coronal loop.

Let us assume that at $t = 0$ the loop is semi-circular and its length is L_0. In order to reproduce the different movement over the two directions, we introduce two different expansion speeds in the horizontal (v_h) and vertical (v_v) direction, so that $v_h < v_v$. Again, we suppose that the motion occurs linearly in time and write the dynamics over the two axes as

$$x = \left(\frac{L_0}{\pi} + v_h t\right)\cos\theta, \quad z = \left(\frac{L_0}{\pi} + v_v t\right)\sin\theta. \tag{5.67}$$

Let us introduce a new set of dimensionless quantities

$$\tau = \frac{v_v t}{L_0}, \quad \tilde{\omega} = \frac{\omega L_0}{c_{kf}}, \quad \tilde{\alpha} = \frac{\alpha}{L_0}, \quad V = \frac{v_h}{v_v}, \quad \tilde{S}_0 = \frac{S_0}{L_0}. \tag{5.68}$$

In the new variables, the governing equations become

$$\frac{\partial^2 \tilde{S}_0}{\partial \theta^2} + \tilde{\alpha}^2\tilde{\omega}^2 \exp\left[-\frac{L_0(1+\tau\pi)}{\pi H}\sin\theta\right]\tilde{S}_0 +$$

$$\frac{\sin\theta\cos\theta[\tau^2\pi^2(1-V^2) + 2\tau\pi(1-V)]}{1 + \tau^2\pi^2(\sin^2\theta + V^2\cos^2\theta) + 2\tau\pi(\sin^2\theta + V\cos^2\theta)} \times \frac{\partial \tilde{S}_0}{\partial \theta} = 0, \tag{5.69}$$

and

$$\tilde{\omega}\tilde{\alpha}\int_0^\pi \left(\frac{\tilde{S}_0^2}{\tilde{c}_k^2}\right) d\theta = 0, \tag{5.70}$$

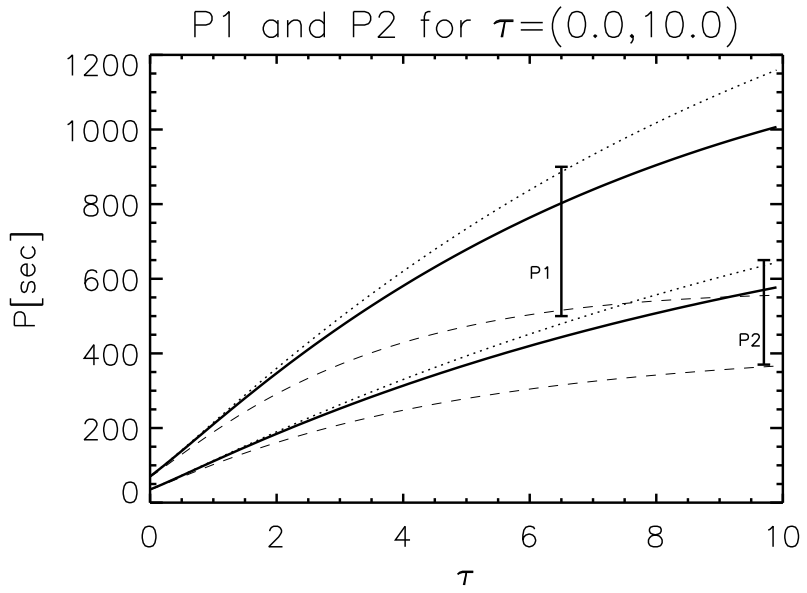

Figure 5.5: The same as in Figure 5.3, but here we assume that the expansion of the loop occurs such that the loop evolves into a loop with a semi-elliptical shape. The meaning of different line-styles is identical to Fig 5.3.

where $\bar{c}_k = c_k/v_v$.

Figure 5.5 displays the evolution of the period of oscillations for the fundamental mode and its first harmonic for three different values of L_0/H, similar values as used in the previous section. Comparing the findings in Figure 5.3 and Figure 5.5, the effect of the expansion into an elliptical shape compared to the constant semi-circular shape is evident. As time progresses the period of oscillations tend to a higher value for elliptical shape, however this conclusion is more true for the fundamental mode. The period of the fundamental mode corresponding to an expansion in a solar corona where scale height is only 23.5 Mm (corresponding to a temperature of 0.5 MK in a loop in hydrostatic equilibrium) saturates rather quickly.

A more significant change is evident when comparing the P_1/P_2 period ratio of the expansion into an elliptical shape shown in Figure 5.5 to the variation of the period ratio for a semi-circular shape. For the same time interval the decrease of the period ratio is much more significant, and similar to the previous

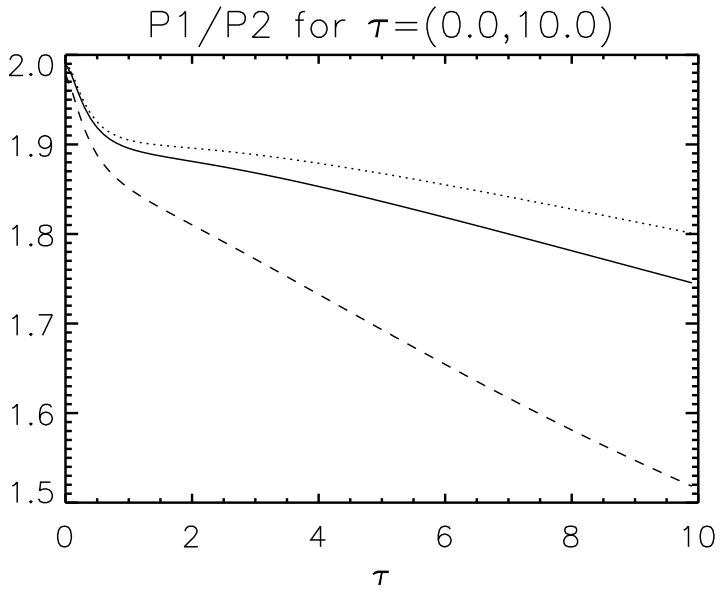

Figure 5.6: The same as in Figure 5.4, but here we assume that the expansion of the loop occurs such that the loop evolves into a loop with a semi-elliptical shape. The meaning of different line-styles is identical to Fig 5.3.

case, the period ratio is more affected for the case of strong stratification, i.e. small H.

We ought to mention here that the temporal dependence of the length of the loop (linear variation with time) would mean that the increase in the size of the loop occurs at a constant rate, i.e. $dL/dt = ct$.

5.8 Conclusions

The solar corona is a very dynamical environment where changes in the dynamical state of the plasma and field occur on all sort of time scales. In the present study we combined for the first time two kinds of dynamical events: the time-evolution of a coronal loop through its expansion into the 'empty' corona and the transverse kink oscillations of coronal loops. The emergence and expansion of a coronal loop through the solar atmosphere is a very complex phenomenon, but here we reduced our model to a simplified process, where the expansion

is solely described by the change in the length of the loop with an associated temporal equilibrium density variation.

The governing equation for kink oscillations was solved in the WKB approximation when the boundary conditions are time-dependent. As expected, due to the change in the length of the loop, the amplitude and periods of oscillations increase with time, however, the period ratio of the fundamental mode and its first overtone decreases. This last physical parameter is of paramount importance for the remote determination of density structuring of coronal loops with the help of seismological approaches. In the first instance we regarded the loop to have an initial semi-circular shape that is maintained through the expansion phase. Later, this restriction was lifted based on the natural assumption that the expansion into the vertical direction (i.e. in the direction of density decrease) occurs much easier than in the horizontal direction. In this limit, the loop evolves into a semi-ellipse, with the major axis in the vertical direction. Comparing the results of the two approaches it is clear that the behaviour of the period ratio is sensitive to the geometrical shape of the loop, a more significant drop in the P_1/P_2 ratio being achieved in the second case. Although our numerical results were obtained for three different structuring degrees (measured by the ratio of the initial loop length to the density scale-height) it is also evident that both the temporal change in the loop length and the stratification will have the same effect upon the period ratio resulting in a mutual amplification of the effect.

Our model predicts that the amplitude of oscillations increases with time, however due to the particular choice of density, damping processes were neglected. Once the density is allowed to vary also in radial direction, according to the theory of resonant absorption (see, e.g. Goossens et al. 1992, Rudeman and Roberts 2002), loops will damp very quickly with the resonant position displaying a steady motion due to the change of the length of the loop. The amplitude of oscillations can also be damped due to the cooling of the plasma (Morton et al. 2010), an effect that was also neglected here. In an expanding loop, the growth of the amplitude due to emergence and decay of amplitude due to resonant damping or cooling will be competing processes and the competition between these two effects.

Chapter 6

2D Magnetic reconnection in stratified atmosphere

6.1 Introduction

Magnetic reconnection, observed under many different conditions, is one of the key physical processes that allow coherent self-organization and relaxation on time-scales faster than the global dissipation time in magnetized plasmas. What is magnetic reconnection? One could describe it as local reconfiguration and annihilation of magnetic field resulting in relaxation of the global topology of the magnetic configuration and transfer of the energy stored in the magnetic field into kinetic and thermal energy of the plasma. In the ideal MHD approximation of a magnetized plasma, the Lorentz force perfectly binds both ions and electrons to magnetic field-lines by assuming the Larmor radii of particles' gyration around the field-lines to be infinitely small. Then, Faraday's law insures that the magnetic field-lines move together with the quasi-neutral plasma i.e., the magnetic field is frozen into the plasma fluid when collisional and inertial effects are ignored. As a result, ideal MHD allows no change in the topology of magnetic field immersed in plasma fluid and is therefore incapable of describing the process of magnetic reconnection. In order to allow the magnetic field to reconnect, dissipative and other physical processes become important locally on spatial scales smaller than the system size have to be included in the plasma description. Depending on the magnitude of the ambient magnetic

field, surrounding plasma temperature and density, various 'non-ideal' effects can become the main mechanism for breaking the magnetic field lines. These include, but are not limited to, collisional resistivity, inertial separation of ion and electron fluids due to their mass density difference, anisotropy due to finite ion and electron Larmor radius effects, and combinations thereof. Below, we briefly describe what is known to date about the magnetic reconnection phenomenon.

In nature, the phenomenon has been directly measured in the solar wind see, e.g. Phan (2006), the Earth's magnetotail (Oieroset et al. 2002) and magnetopause (Frey et al. 2003), Vaivads et al. 2004). There is much evidence that magnetic reconnection is responsible for the generation and evolution of solar flares, see e.g. Linton & Priest (2003), Nandy et al. (2003) and coronal mass ejections (CMEs) (Linker et al. 2003), while it has also been proposed as the mechanism for solar coronal heating by Falconer et al. (1997). Although presently there is much less astrophysical data available, magnetic reconnection processes have been conjectured to play an important role in heating of the interstellar, intergalactic and intracluster media, acceleration and relaxation of jets, and dynamics of accreting systems see, e.g. Gary (2002), Colgate et al. (2001). Jet-like events, first reported by Brueckner & Bartoe (1983), are characterised by non-Gaussian spectral line profiles. Dere et al. (1991) suggested that they are produced by bi-directional jets as a result of magnetic reconnection. To date, these jetlike events (often called explosive events) are mainly observed in spectral lines formed at transition region temperatures as reported in studies by Dere (1994), Chae et al. (1998), Innes et al. (2001), Madjarska & Doyle (2003), although observations of explosive events in chromospheric lines are also reported. For example, Madjarska & Doyle (2002) presented the temporal evolution of different plasma temperature using high-cadence (10 s) observations obtained with the Solar Ultraviolet Measurement of Emitted Radiation (SUMER) spectrometer, and found a time delay in the response of the S VI 933 A (2105K) line with respect to Ly 6 (2104K), with the Ly 6 line responding earlier. They concluded that the jet-like events may first appear at chromospheric temperatures. In a follow-up work, Doyle et al. (2005) reported on a joint SUMER, Coronal Diagnostic Spectrometer (CDS) on board the SOHO) and TRACE imager study, confirming the possibility that some jet-

like events originate in the chromosphere. They further suggested that jet-like events could be divided into two types: one formed in the chromosphere and the other formed in the transition region. Some of the observed features are the result of spicules and/or macrospicules (Madjarska & Doyle 2003; Madjarska et al. 2006), while others are the result of high velocity flows in small loops (Teriaca et al. 2004). In a more recent work, Madjarska et al. (2009) presented observational data relating explosive events to a surge and demonstrated that the division of small-scale transient events into a number of different subgroups, for instance explosive events, blinkers, spicules, surges or just brightenings, is ambiguous, implying that the definition of a feature based only on either spectroscopic or imaging characteristics as well as insufficient spectral and spatial resolution can be incomplete.

Several numerical models were developed to study jet-like events. Sarro et al. (1999) used a 1D magnetic flux-tube model to simulate the temporal evolution of UV emission line profiles, e.g. C IV 1548.2 A, in response to energy perturbations located below the transition-region. The maximum blue-shifts they obtained reach values of the order of 100 km s^{-1}.

Though magnetic reconnection is undoubtedly a three-dimensional (3D) phenomenon, to date, no true 3D phenomenological description of magnetic reconnection agreed upon exists in the community. Since we investigate only two-dimensional (2D) systems in this work, here we limit the discussion to that of 2D magnetic reconnection, as well. Two phenomenological descriptions of 2D steady-state magnetic reconnection in the resistive MHD limit were proposed early on. One, by Sweet (1957) and Parker (1963), known as Sweet-Parker reconnection, describes evolution of a long and thin current layer, whose length is of the order of the system size and width is proportional to square root of resistivity. The other, by Petschek, proposed a localized reconnection region (Petschek proposed that such localization would be accomplished by slow shocks along the magnetic field separatrices) which would allow for faster plasma inflow and faster reconnection of magnetic field lines. The Sweet-Parker description of resistive reconnection has been confirmed by numerous numerical simulations i.e Uzdensky et al (2000), however its predicted reconnection rate is too slow for that observed both in space (Birn et al. 2001) and in laboratory experiments

(Cothran et al. 2005), Yamada et al. 2006). On the other hand, while there is no experimental or computational evidence of slow shocks emanating from the reconnection region, as proposed by Petschek, localization of the reconnection layer appears to be the key to the so-called 'fast reconnection' , which allows for release of magnetic energy in a period of time consistent with observations (see, e.g. Linker et al. 2003, Shay et al. 2004). Numerical simulations have confirmed that both of the mechanisms proposed to produce such instability-induced locally enhanced resistivity (Malyshkin et al. 2005) and two fluid and/or kinetic effects (Birn et al. 2001) lead to fast reconnection (Breslau et al. 2003).

Innes & Tóth (1999) presented a 2D MHD study on jet-like events with different initial conditions, representative of different regions in which the reconnection occurs, e.g. the corona and chromosphere. Their conclusion was that high-velocity components in the profiles of lines formed around 10^5 K can be obtained in both cases, irrespective of the initial conditions. However, heat conduction was not included, and no brightening was found at the zero velocity position of the spectral line. In their model, the initial equilibrium state consists of two regions of oppositely directed magnetic field lines, with a narrow current sheet between the two regions.

Yokoyama & Shibata (1995, 1996) performed 2D magnetic reconnection to study coronal X-ray jets using both oblique and vertical initial coronal magnetic fields. The temperature of the hot X-ray jets they obtained reach 3 times the coronal temperature. Moreno-Insertis et al. (2008) considered magnetic reconnection triggered by flux emergence from below the photosphere using a 3D MHD model. Very strong X-ray jets with high temperature (3×10^7K at the reconnection site) and high velocity (peak velocity 400 km s^{-1}) were produced. In their model, the flux emergence is very strong (maximum field strength 3.8 kG), which plays a very important role in forming such strong jets. Isobe et al. (2008) focused on the process of magnetic flux emergence, and presented simulations of magnetic flux emergence driven by the upward convective motion. They found that small-scale horizontal magnetic fields could be produced even when the initial magnetic field is uniform and vertical. The horizontal magnetic fields emerging from the convection zone into the photosphere undergoes magnetic reconnection with the background vertical field, which is a

source of high-frequency MHD waves that may contribute to coronal heating or solar wind acceleration. Murray et al. (2009) presented another simulation of magnetic flux emergence, where the long-term evolution of magnetic reconnection was initiated by flux emergence. All the flux emergence studies mentioned above did not include heat conduction and radiative effects. The latter will reduce both the temperature and the velocity of the outflow jets. Litvinenko & Chae (2009) discussed magnetic reconnection at different heights in the solar atmosphere, and found that the temperature and speed of the outflow jets vary by several orders. Their study was based on an extended Sweet-Parker model (Parker 1957, 1963), assuming that the inflowing magnetic energy is completely converted in the current sheet into the thermal and kinetic energies of the outflowing plasma.

Magnetic reconnection at the current sheet is initiated by introducing localized anomalous resistivity. Roussev et al. (2001) carried out 2D MHD simulations, where jet-like events are formed during the process of magnetic reconnection. In their model, the initial magnetic field is parallel to the yaxis (vertical), and there is a thin current concentration formed along the y-axis. Magnetic reconnection is initiated by a localized increase of the magnetic diffusivity in the current concentration. Blue-shifts of the order of 100 kms^{-1} were obtained. By using the same model, they further extended the work and performed simulations under different physical conditions (Roussev et al. 2001a, 2001b). In order to investigate the events they used a 2D MHD model from an unstratified to a stratified Sun by introducing gravity and resistivity in their initial magneto-hydrostatic solution. Studying mangnetic reconnection in this 2D environment the dynamics change from an initial stage, straight magnetic field lines to a more complex 2D X-point reconnection due to magnetic field expansion by inclusion of gravity in the initial states. They studied several cases where the magnetic field expands faster or slower with height. The faster it expands the slower and more complex the magnetic reconnection becomes at the early stages of the evolution.

Inspired by the work of Rousev et al. (2002) (hereafter, referred to as ROU02) we decided to study a similar reconnection process but taking into account a different magnetic field and a more complex stratified environment

where the reconnection process is not confined to a a very small region in the middle of the simulation box. In this work, we also attempt to advance the understanding of the fast reconnection phenomenon through Hall MHD and its relevance to the reconnection process. We are going to use LARE2D (see Arber et al. 2001) in order to solve the system of equations.

Lare2D is a Lagrangian remap codes for solving the MHD equations in 2D. The code uses a staggered grid and is second order accurate in space and time. The use of shock viscosity and gradient limiters make the code ideally suited to shock calculations. It solves nonlinear MHD equations with user controlled viscosity, resistivity, gravity, Hall term, partially ionised hydrogen equation of state, Cowling resistivity and parallel thermal conductivity. IN ROU02 the induced resistivity was considered as nonuniform. Here, we take resitivity to be constant, and compare with ROU02 study for various values of resistivity.

6.2 Physical setup of the problem

In this section we present our 2D model for magnetic reconnection in stratified atmospheres. The MHD equations including gravity and resistivity are given in section 6.2.1. In section 6.2.2 we provide the set of initial conditions followed by numerical experiments in 6.3.

6.2.1 MHD equations

The MHD equations that include gravity and resistivity terms are

$$\frac{D\rho}{Dt} = -\rho\nabla\cdot\mathbf{U}, \tag{6.1}$$

$$\rho\frac{D\mathbf{U}}{Dt} = -\nabla\rho + \mathbf{j}\times\mathbf{B} + \rho\mathbf{g} - \nabla\cdot\tau, \tag{6.2}$$

$$\nabla\cdot\mathbf{B} = 0, \tag{6.3}$$

$$\frac{D\mathbf{B}}{Dt} = (\mathbf{B}\cdot\nabla)\mathbf{U} - \mathbf{B}\nabla\cdot\mathbf{U} - \nabla\times[\eta\nabla\times\mathbf{B}], \tag{6.4}$$

$$\frac{De}{Dt} = -\gamma e\nabla\cdot\mathbf{U} + Q. \tag{6.5}$$

Table 6.1:

Phys. quantity	Notation	Typical Value
Length	L_0	1.5×10^6(m)
Velocity	V_{A0}	1.293×10^5(ms^{-1})
Time	t_{A0}	11.6(s)
Gravity	g_0	2.7×10^2(ms^{-2})
Density	ρ_0	5.02×10^{-11}(kgm^{-3})
Temperature	T_0	1×10^5(K)
Magnetic field	B_0	0.0008(T)

where $D/Dt = \partial/\partial t + \mathbf{U} \cdot \nabla$, and γ, ρ, p, e, $\mathbf{U}$, $\mathbf{B}$, $\mathbf{j}$, $\mathbf{g}$, η, τ, Q denote the adiabatic index, mass density, kinetic gas pressure, thermal energy, fluid velocity, magnetic field, electric current density, the field of gravity, magnetic diffusion coefficient, viscous stress tensor and dissipation term. The current, $\mathbf{j}$, and pressure, p, are given by

$$\mathbf{j} = \nabla \times \mathbf{B}, \quad p = e(\gamma - 1) = \rho T. \tag{6.6}$$

6.2.2 Initial states

We start by denoting a typical length scale, velocity, time scale, mass density, temperature, kinetic gas pressure, thermal energy, magnetic field strength, and electric current density, by L_0, V_{A0}, t_{A0}, ρ_0, T_0, p_0, e_0, B_0, and j_0, respectively. All these parameters are chosen to represent the *quiet* solar transition region. Assigned values for these parameters can be found in Table 6.1 (in SI units). Dimensionless quantities are denoted by t^*, $\mathbf{u}$, $\mathbf{b}$, $\mathbf{g}^*$, ρ^*, T^*, p^*, e^* and j^*.

Relations between the physical quantities and normalised variables are given by

$$t^* = \frac{t}{t_{A0}}, \mathbf{u} = \frac{\mathbf{U}}{V_{A0}}, \mathbf{b} = \frac{\mathbf{B}}{B_0},$$
$$\mathbf{g}^* = \mathbf{g}\frac{t_{A0}}{V_{A0}}, \rho^* = \frac{\rho}{\rho_0}, T^* = \frac{T}{T_0},$$
$$p^* = \frac{p}{p_0}, e^* = \frac{e}{e_0}, j^* = \frac{j}{j_0}.$$

Tthe normalised coordinates x^* and y^* are

$$x^* = x/L_0, y^* = y/L_0,$$

where we have $x^*_{\min} \leq x^* \leq x^*_{\max}$ and $y^*_{\min} \leq y^* \leq y^*_{\max}$ with $x^*_{\min} = -x^*_{\max}$ and $y^*_{\min} = -y^*_{\max}$. Initially the plasma is static, i.e. $\mathbf{u} = 0$, and the initial magnetic field, $\mathbf{b} = (b_x, b_y)$, is prescribed by

$$b_x(x^*, y^*) = b_0 \left(\frac{x_{sc}}{y_{sc}}\right) \left[\frac{x^*}{x_{sc}} \text{arcsinh} \left(\frac{x^*}{x_{sc}} - \sqrt{1 + \left(\frac{x^*}{x_{sc}}\right)^2}\right)\right] \exp\left(-\frac{y^*}{y_{sc}}\right), \tag{6.7}$$

and

$$b_y(x^*, y^*) = \text{arcsinh}\left(\frac{x^*}{x_{sc}}\right) \left[b_1 + b_0 \exp\left(-\frac{y^*}{y_{sc}}\right)\right] \tag{6.8}$$

The variables x_{sc} and y_{sc} are two free model parameters, where x_{sc} - controls the width of the current concentration around the symmetry axis x^* and y_{sc} controls the scale height of the magnetic field. The constants b_0 and b_1 are chosen in such a way that the magnetic field lines of opposite polarity are straight.

Initially we have a static equilibrium so the Lorentz and gravity forces have to be balanced by the pressure gradient in the entire physical domain, determined by the momentum equation

$$\frac{\partial p^*}{\partial x^*} + j^* b_y = 0, \tag{6.9}$$

$$\frac{\partial p^*}{\partial y^*} - j^* b_x + \rho^* g^* = 0. \tag{6.10}$$

Here $j^* = (0, 0, j^*_z)$ is the only non-zero component of the electric current density. These equations are solved by means of Lare2D in order to find the corresponding mass density, ρ^*, and kinetic gas pressure, p^*, using the magnetic field given by equations (6.7) and (6.8). The corresponding plasma temperature is determined by $T^* = p^*/\rho^*$.

Once all the initial parameters, γ, x_{sc}, y_{sc}, b_0, b_1, g are given, we can start our simulation using Lare2D. The plasma 'beta' parameter depends on both spatial coordinates and is constant with height. The actual dependence is controlled

by the value of the y_{sc} parameter. The smaller y_{sc}, the faster β will increase. Once the scale-height has higher values, β tends to be uniform with height (see Figure 6.1).

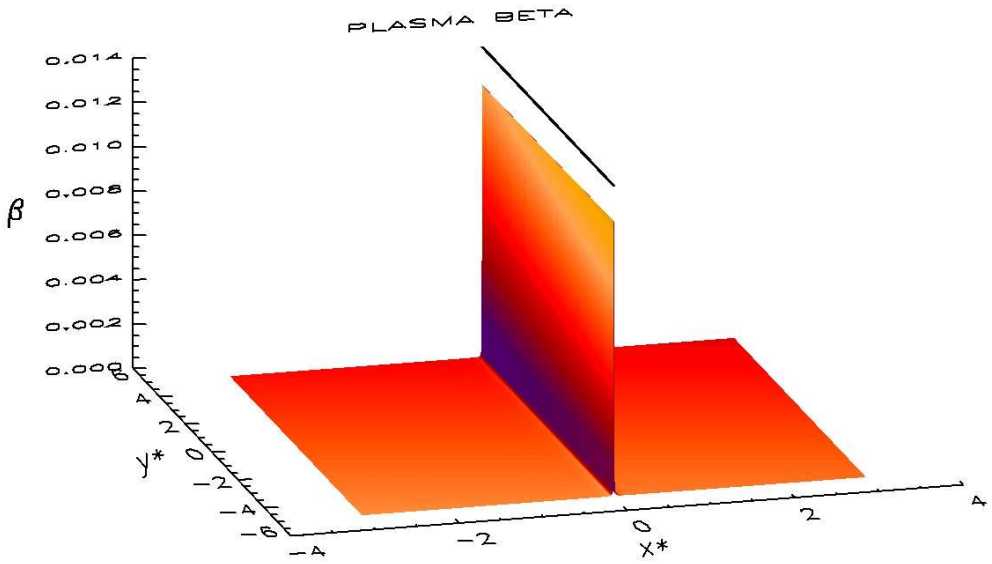

Figure 6.1: Initial plasma β in the simulation domain for $y_{sc} = 10$ and $\eta = 0.005$.

6.3 Set of experiments

Further we explore the dynamical evolution of magnetic reconnection in various physical conditions representing a 2D stratified solar atmosphere. Based on the initial setup we are going to study three different states (see Table 2).

Experiments are carried out by using Lare2D MHD code, equations are solved in a 2D domain with the centre of diffusion region moved down by $y_0^* = 0.5$ in order to have faster upward propagation. The numerical grid-size is $N_x \times N_y = 1500 \times 2000$, with the computational domain chosen to be the size of $[2x^*_{max}, 2y^*_{max}] = [6, 10]$. In all experiments, we choose $\gamma = 5/3$, $g^* = 0.0242$, $x_{sc} = 0.05$, $y_{sc} = 10$, $b_0 = 0.1$, $b_1 = 0.75$ in such a way that the magnetic field has straight field lines inside the box and we vary η. We also carry out

simultaneously, simulations using Lare2D code for another similar magnetic field profile studied in detail by ROU02 and compare the two cases.

We first show the distribution of equilibrium plasma parameters for our initial set-up with $\eta = 0.005$ and compare with the initial setup parameters from ROU02. We can spot that the density profile of ROU02, is less stratified than ours as shown in Figures 6.2 and 6.3. The density stratification shown here has

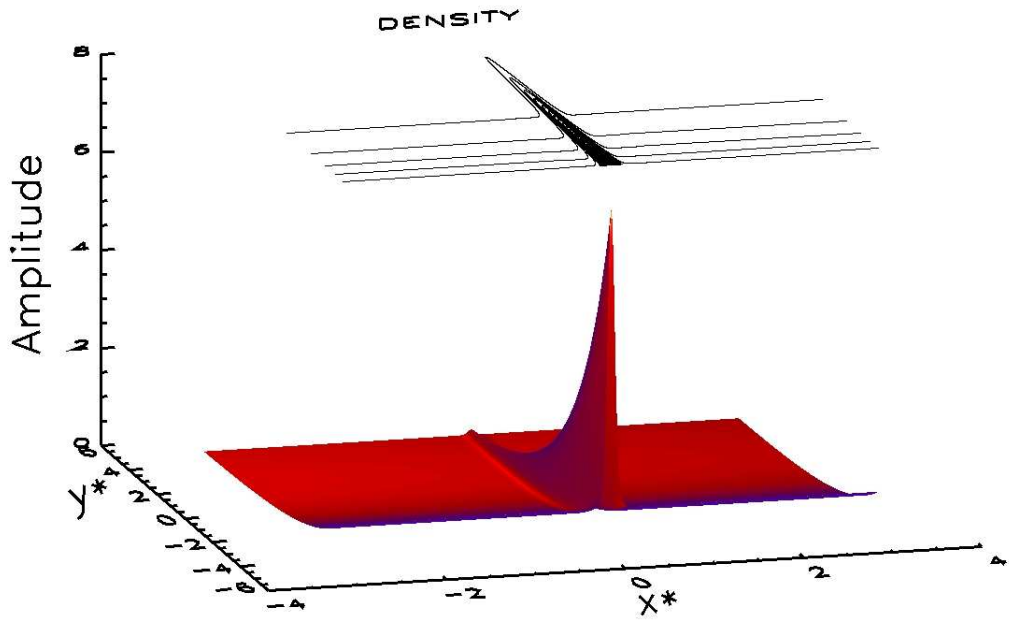

Figure 6.2: Density profile for ROU02 case $\eta = 0.005$ $t^* = 0$

this shape because in our case magnetic field lines are straight and in ROU02 case they flare out. The stratification can be seen better if we represent the surface plots of the initial J_z for both cases in Figure 6.5 for our case and Figure 6.4 for ROU02 profile. Initial temperature profile shown in Figure 6.6 can also be compared with Figure 6.7 for ROU02. We can see that in regions with higher densities we have lower temperatures compared to regions with lower densities. For both cases, the only noticeable difference is that initial temperature, as in our case is higher mainly due to different density stratification. (see Figures 6.8 and 6.9).

6.3

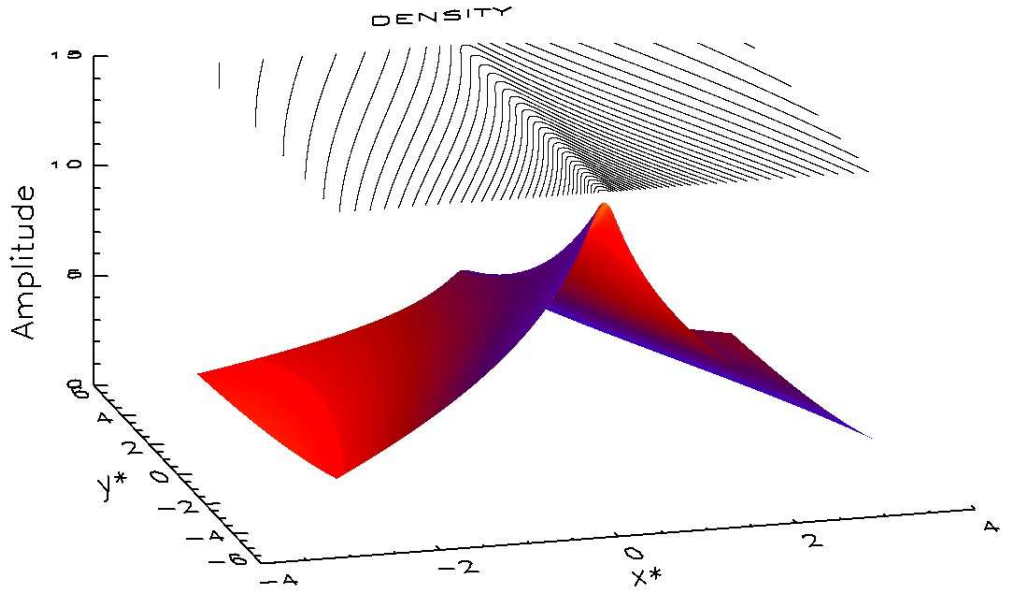

Figure 6.3: Density profile for our case $\eta = 0.005$ $t^* = 0$

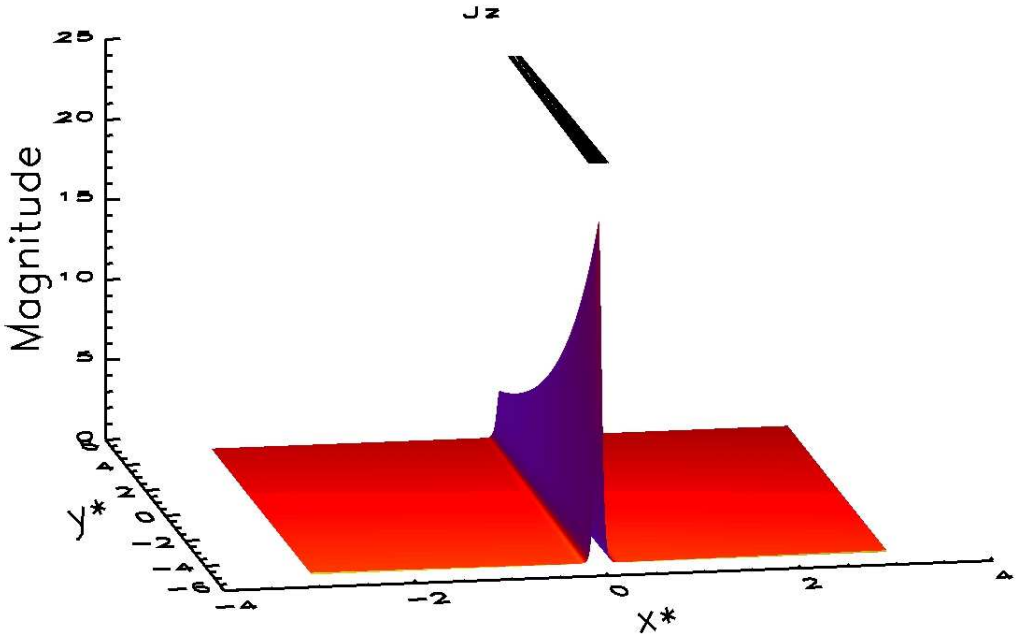

Figure 6.4: J_z for ROU02 case $\eta = 0.005$, $t^* = 0$

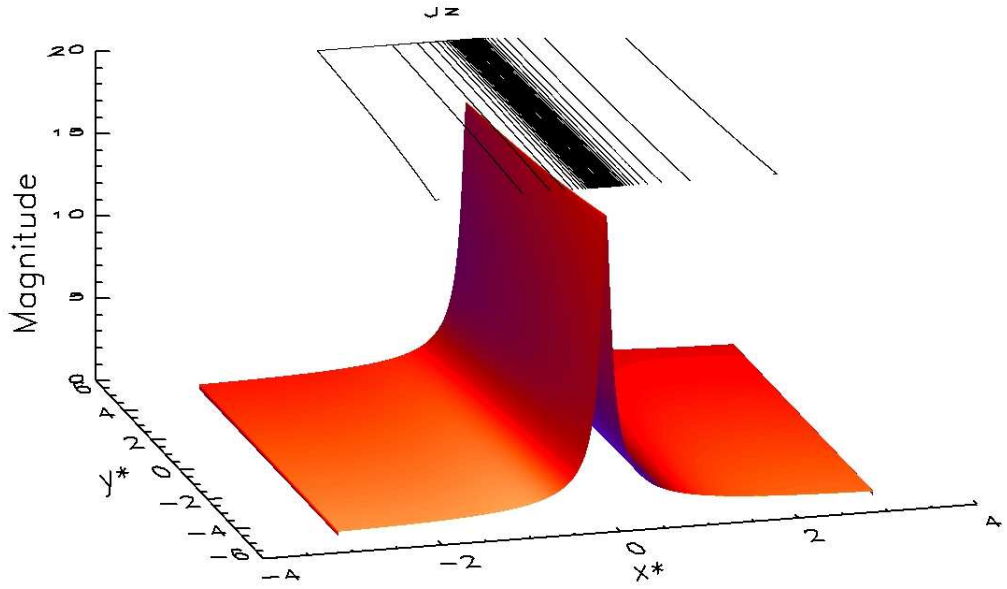

Figure 6.5: J_z for our case $\eta = 0.005$, $t^* = 0$

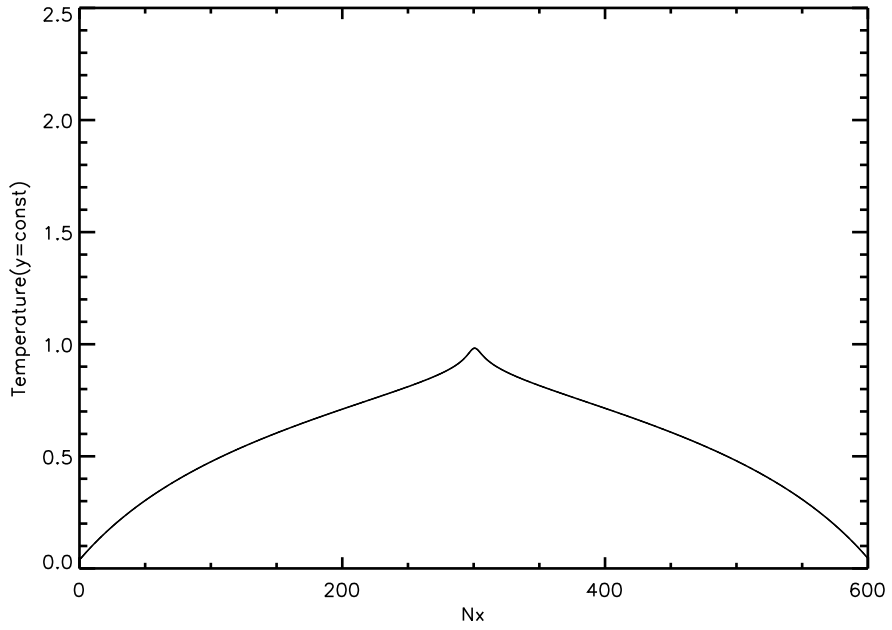

Figure 6.6: Temperature profile for our magnetic field with respect to x at $y = -0.5$, $nx = 300$ represents $x^* = 0$.

6.3

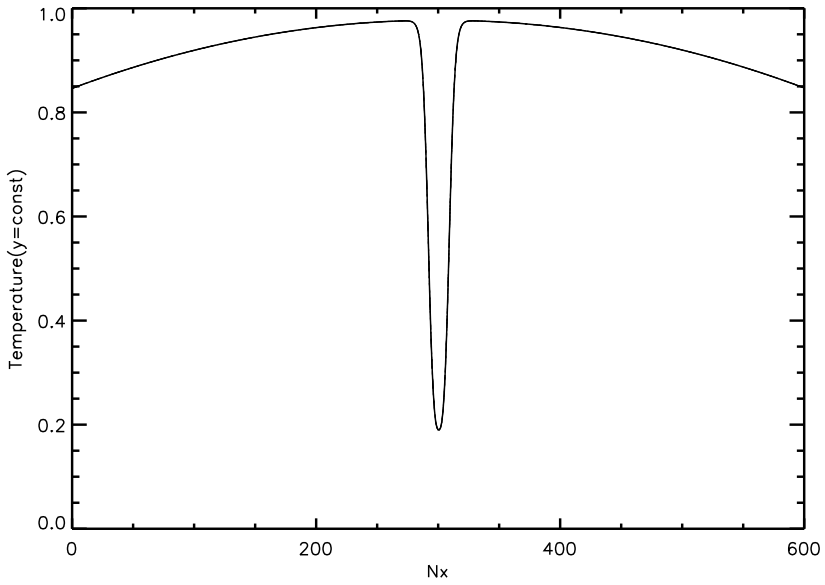

Figure 6.7: Temperature profile for ROU02 with respect to x at $y = -0.5$, where $nx = 300$ represents $x^* = 0$.

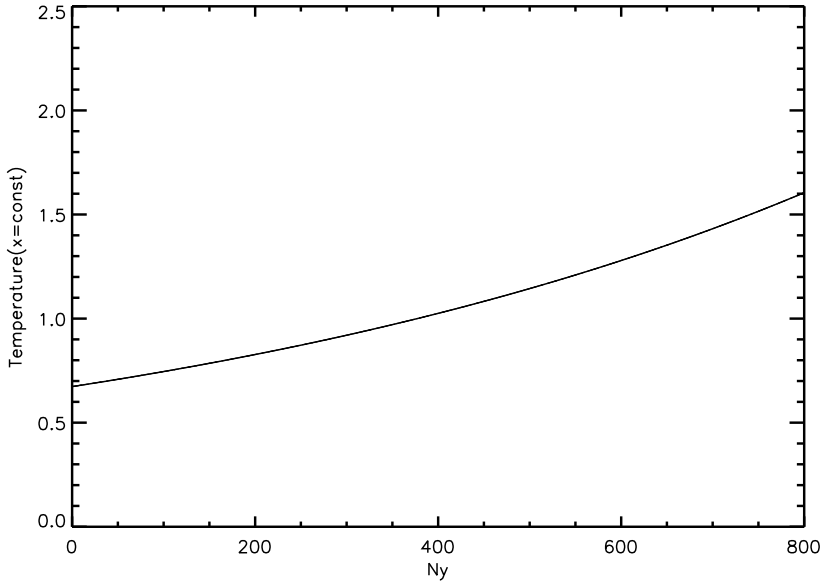

Figure 6.8: Temperature profile for our magnetic field with respect to y at $x = 0$, and $t^* = 0$, where $ny = 400$ represents $y^* = -0.5$.

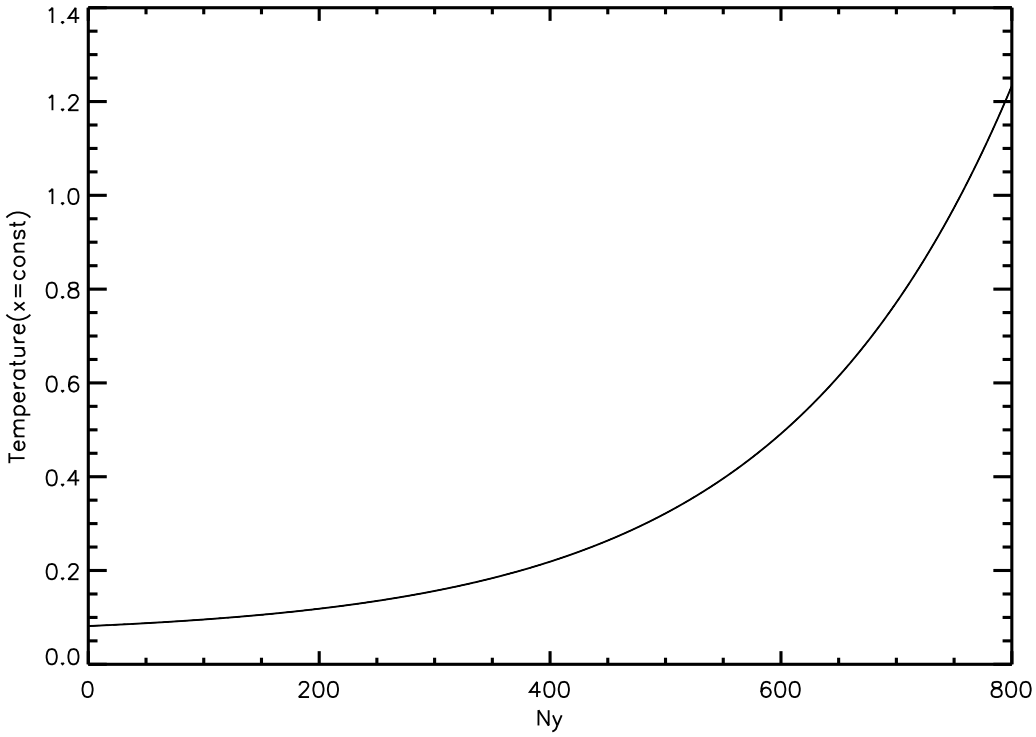

Figure 6.9: Temperature profile for ROU02 with respect to x at $x = 0$ and $t^* = 0$, where $ny = 400$ represents $y^* = -0.5$.

6.4 Reconnection process

Once we've started the simulations we find that the magnetic field lines start to reconnect at around $t^* = 6$. Once this process starts, both magnetic pressure and kinetic gas pressure decrease in the region of localised magnetic diffusion. This initiates pressure-driven inflow of plasma in the diffusion region from outside. This is followed by two reconnection jets that are naturally formed. The faster the magnetic field strength decreases with height, the further the jets will expand in horizontal direction, x^*.

Comparison with ROU02, at the reconnection point reveals some differences due to the magnetic field profile, differences related to current sheet width (wider jet's for ROU02). As we would expect in ROU02, due to opening of the magnetic field lines, reconnection jets expand faster in horizontal x^* direction (see Figure 6.10) compared to our 'straight' magnetic field line case (see Figure 6.11). A

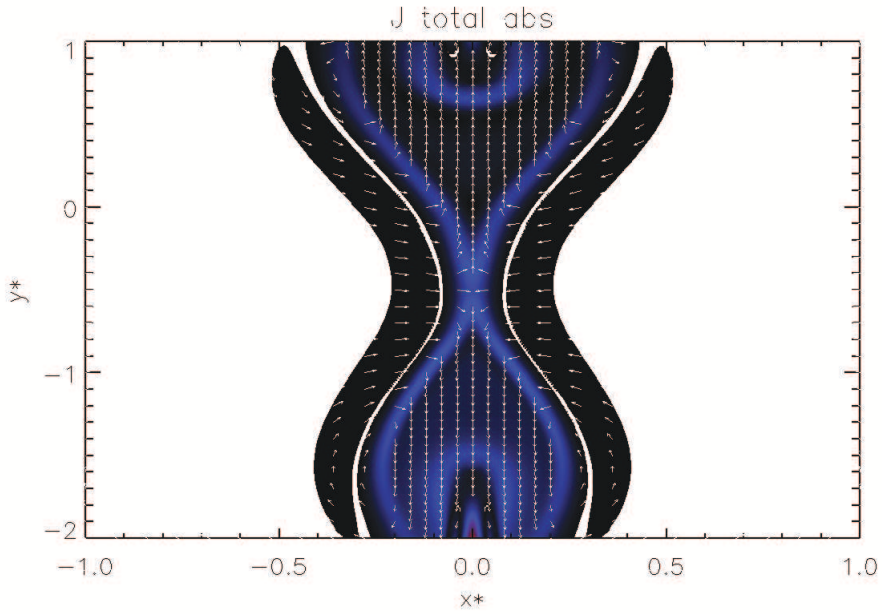

Figure 6.10: ROU02 representation of J_z and jets through velocity vector plots at $t^* = 5$

better way to see this difference is through magnetic field line reconnection (see Figure 6.13 and Figure 6.12)

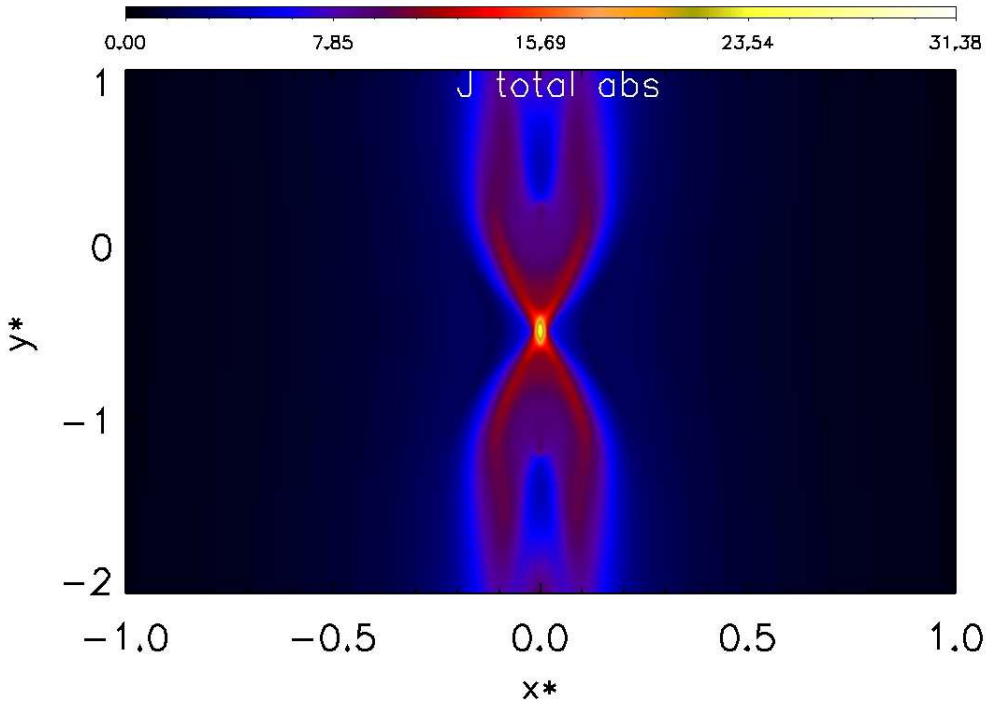

Figure 6.11: Straight case J_z for experiment Exp2 at $t^* = 6$

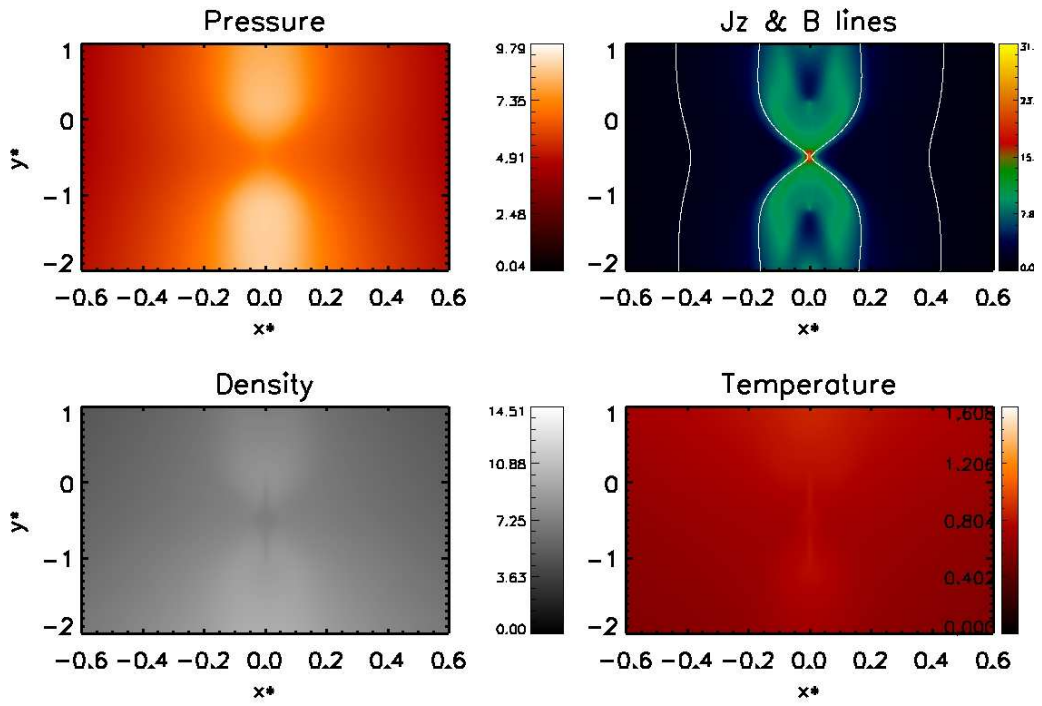

Figure 6.12: Exp2 our 'straight' case representation of B^* top left, p^* to right, ρ^* bottom left and T^* bottom right at $t^* = 6$

The wider the jets are the smaller the pressure difference between inside and outside of the jets. The standing slow-mode shocks are recognised as locations of strong positive current concentrations (bright lanes). They occur because of the steep gradient of the parallel magnetic field component across the shocks, with the after-shock field strength being decreased. These are recognised in Figure 6.14 for ROU02 and Figure 6.15 for our magnetic field profile as negative current densities (dark lanes).

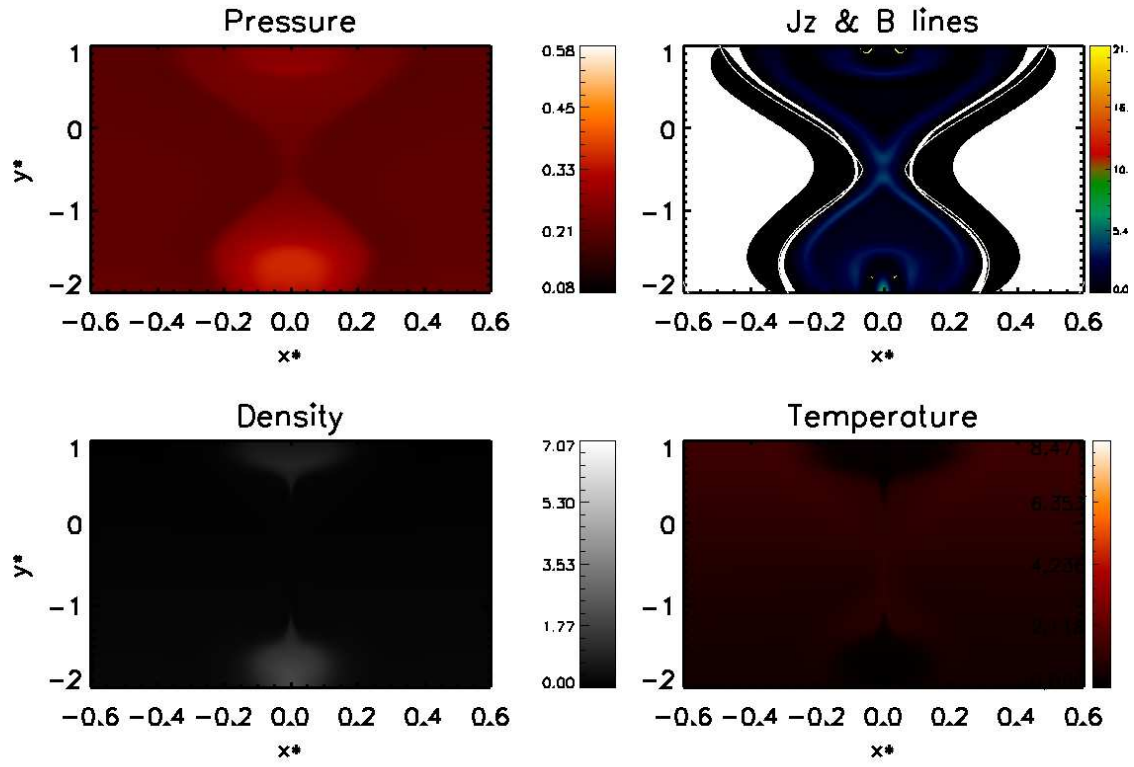

Figure 6.13: ROU02 case representation of B^* top left, p^* to right, ρ^* bottom left and T^* bottom right at $t^* = 5$

6.4

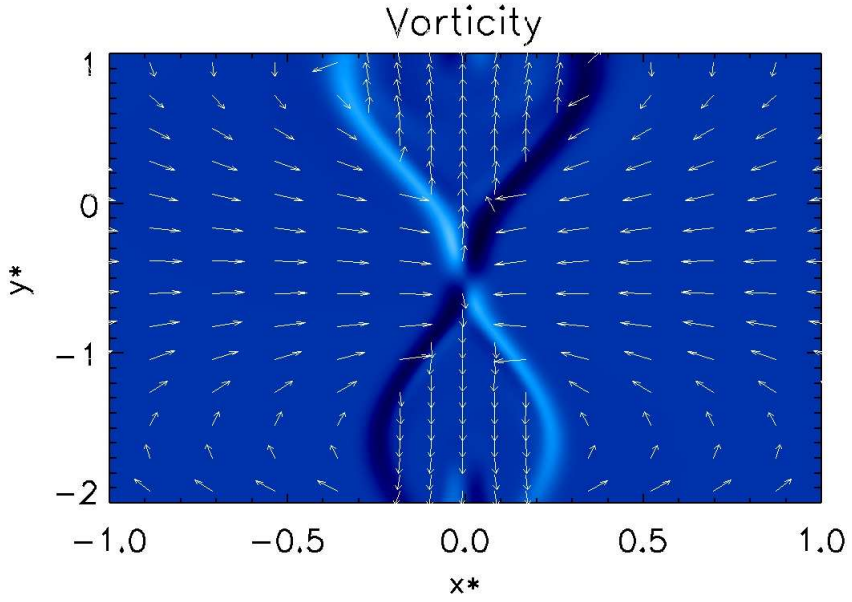

Figure 6.14: The vorticity in the ROU02 case at $t^* = 6$.

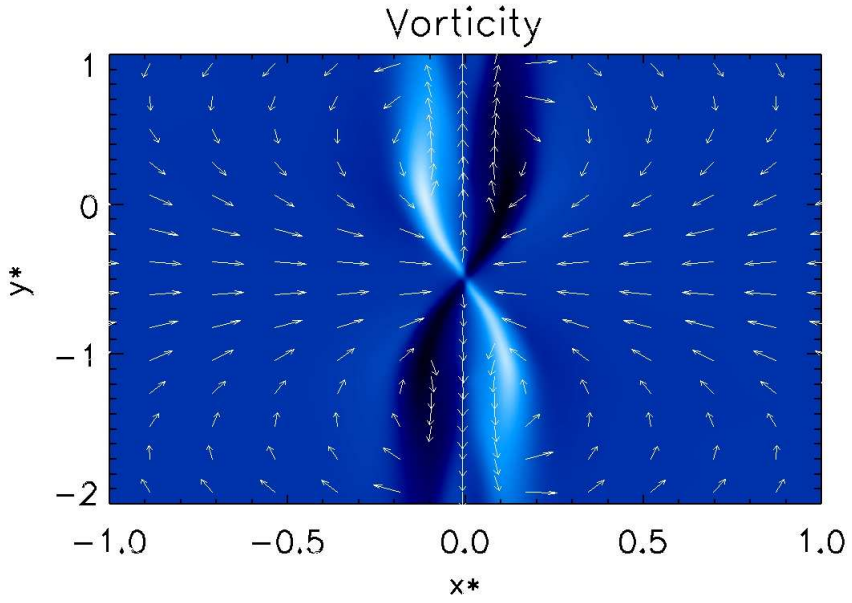

Figure 6.15: The vorticity for our 'straight' case in Exp2 at $t^* = 6$.

6.5 Time evolution of reconnection processes

By comparing the graphs showing the peak jet velocity versus position and time (y, t^*) and plotting the reference density and temperature, we can see that the parameter η changes the dynamics of the reconnecting magnetic field lines substantially. We can see that in ROU02, maximum jet velocity changes with

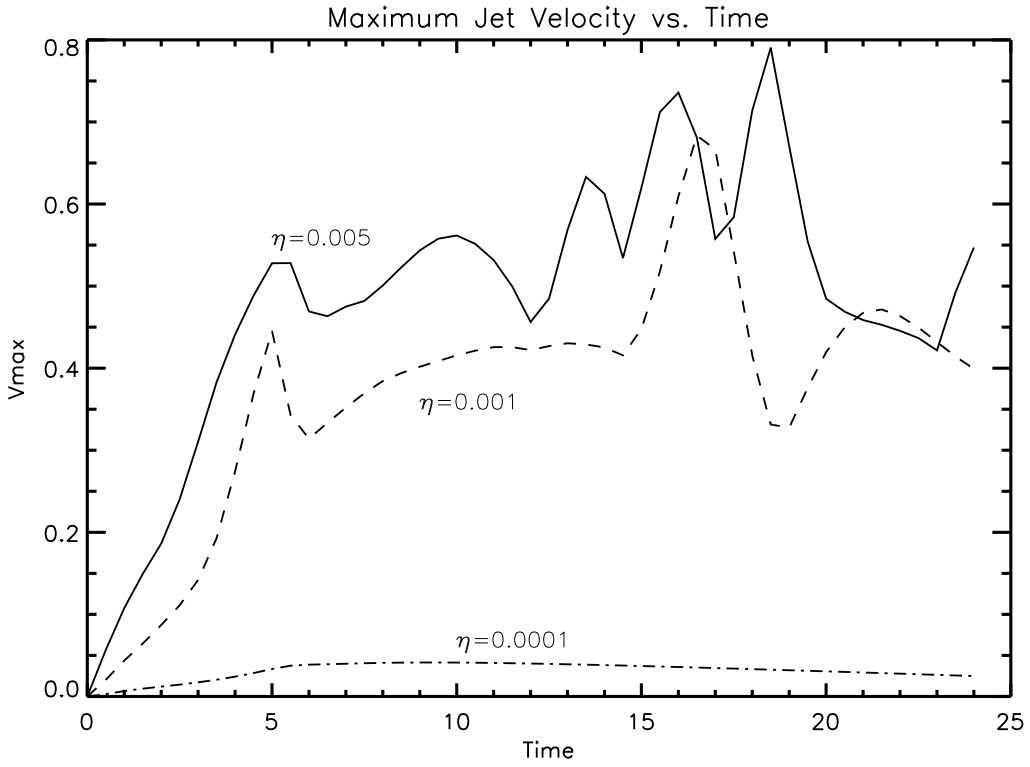

Figure 6.16: ROU02 Maximum Jet Velocity vs. time for different values of η

an order of 20% when η varies from 0.005 to 0.001 (see Figure 6.16). Whereas for $\eta = 0.0001$, the change in velocity is even more pronounced. Maximum jet velocity was calculated by taking the maximum value of absolute velocity vector in the entire simulation box.

6.5

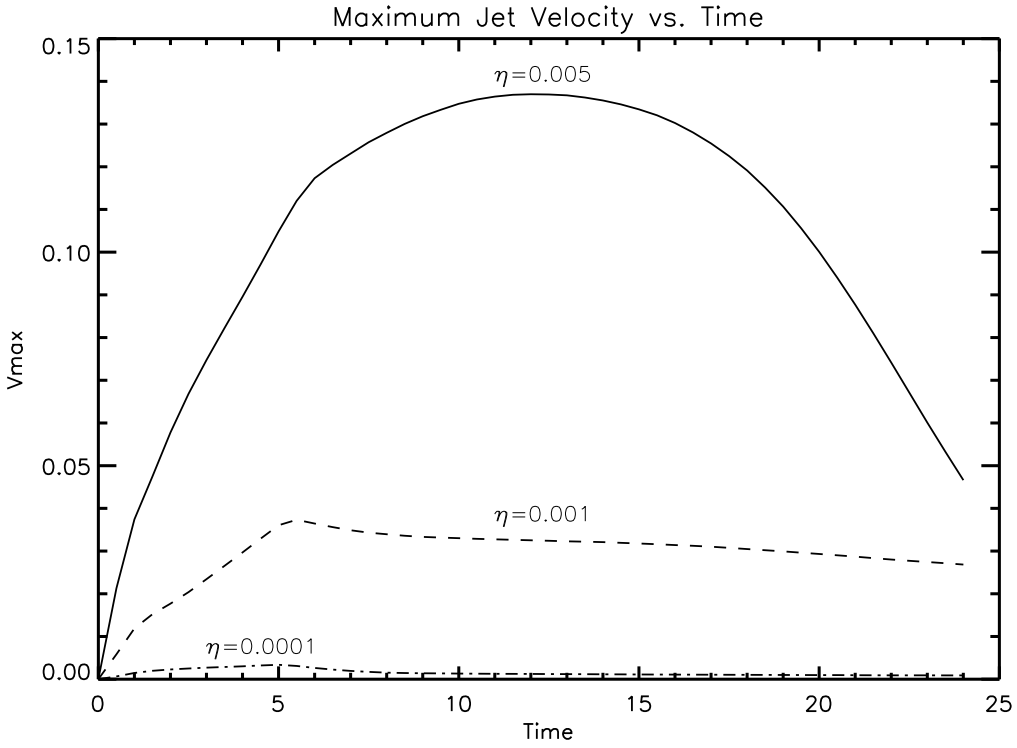

Figure 6.17: Straight case Maximum Jet Velocity vs. time for various η

When comparing to a straight magnetic field line profile, the same pattern appears (see Figure 6.17). Maximum jet velocity is higher in the Exp2 ($\eta = 0.005$) than Exp. 1 and 3. It is worth mentioning that these values are significantly smaller than in the ones found by ROU02 (see Figure 6.16). In Figure 6.16 we can spot several peaks compared to Figure 6.17 where you only see a broad Gaussian shape, this is due to density stratification in our case. Density is more stratified in x^*-direction (see Figure 6.2) when compared to ROU02 (Figure 6.3), where the density stratification is mainly present in the middle of the simulation box, hence we will see more occurrences of magnetic islands than in our case for the same period of time.

Maximum jet velocity as a function of position along y^* also increases with time (see Figure 6.19 for our case and Figure 6.18 for ROU02 case); $\eta = 0.005$ results in higher values for velocities for both profiles.

Velocity is increasing from the reconnection point ($x = 0, y = -0.5$) out-

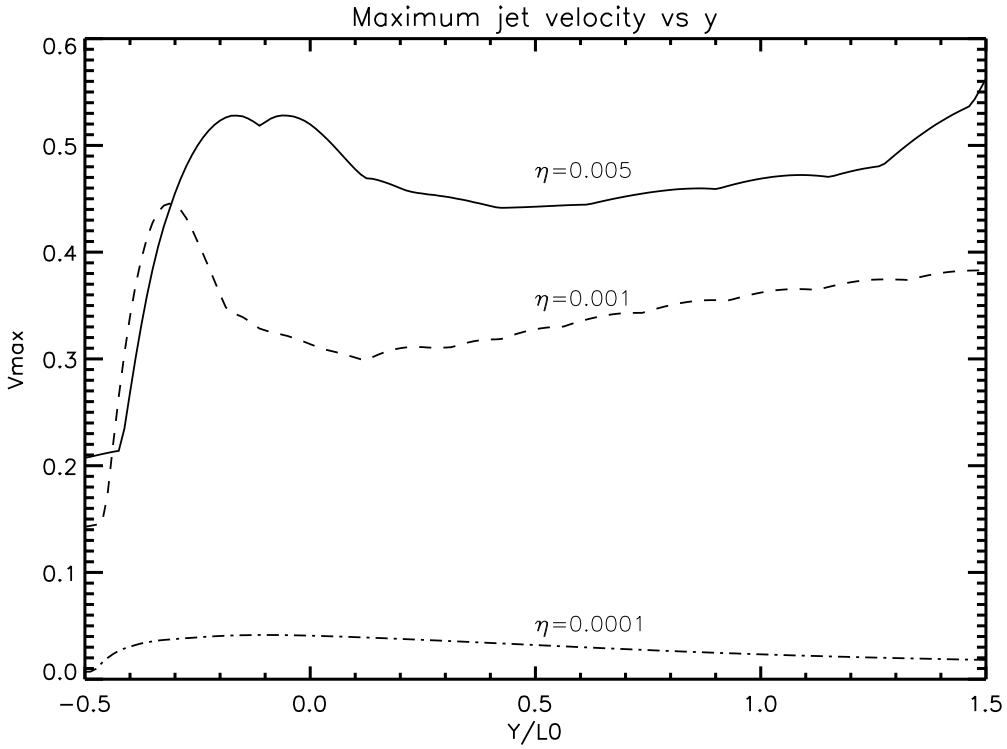

Figure 6.18: ROU02 Maximum Jet Velocity vs. y^* for various values of η

wards in y^* direction as one would expect (see Figure 6.18 and 6.19). The only difference here is that the amplitude is larger in ROU02 case. When it comes to densities at reconnection point region, density evacuates faster in ROU02 compared to our model (see Figures 6.20 and 6.21) and due to constant pressure in ROU02 study, temperature is increasing with decreasing density (see Figure 6.22). This is not the case for our profile (see Figure 6.23).

6.5

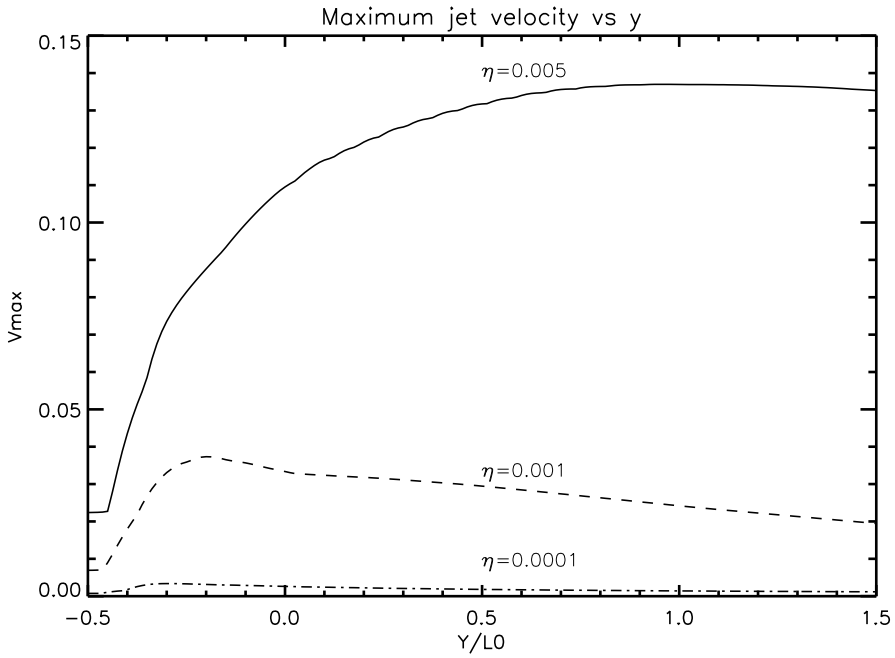

Figure 6.19: Straight case Maximum Jet Velocity vs. y^* for different η parameters

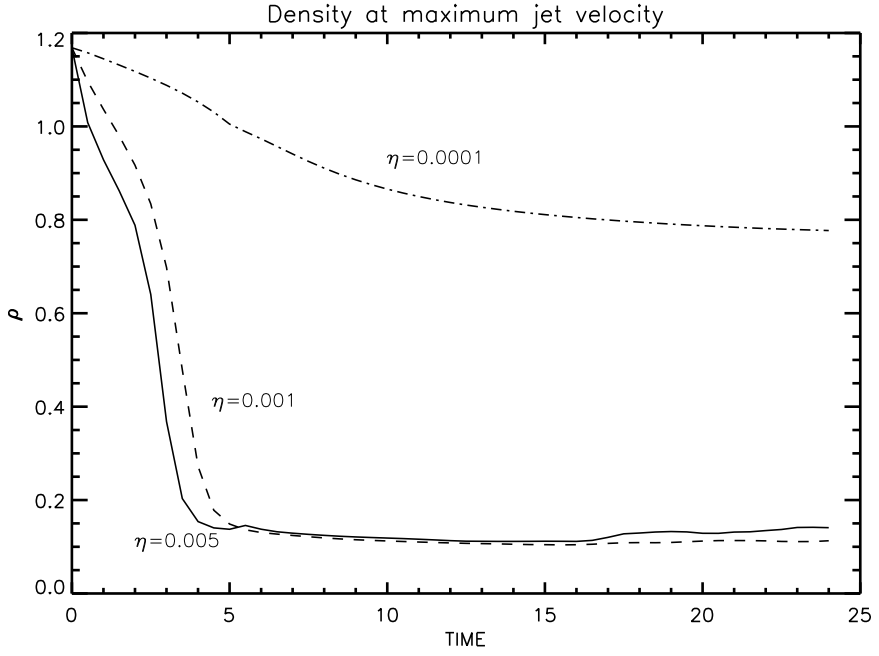

Figure 6.20: ROU02 case density at the reconnection point ($x^* = 0, y^* = -0.5$)

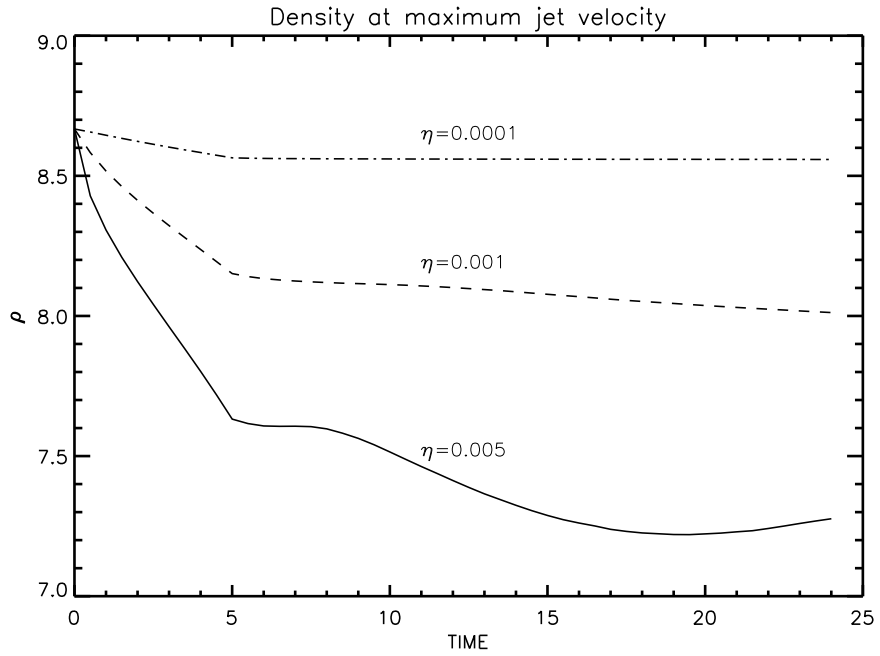

Figure 6.21: Our 'straight' case density at the reconnection point ($x^* = 0, y^* = -0.5$)

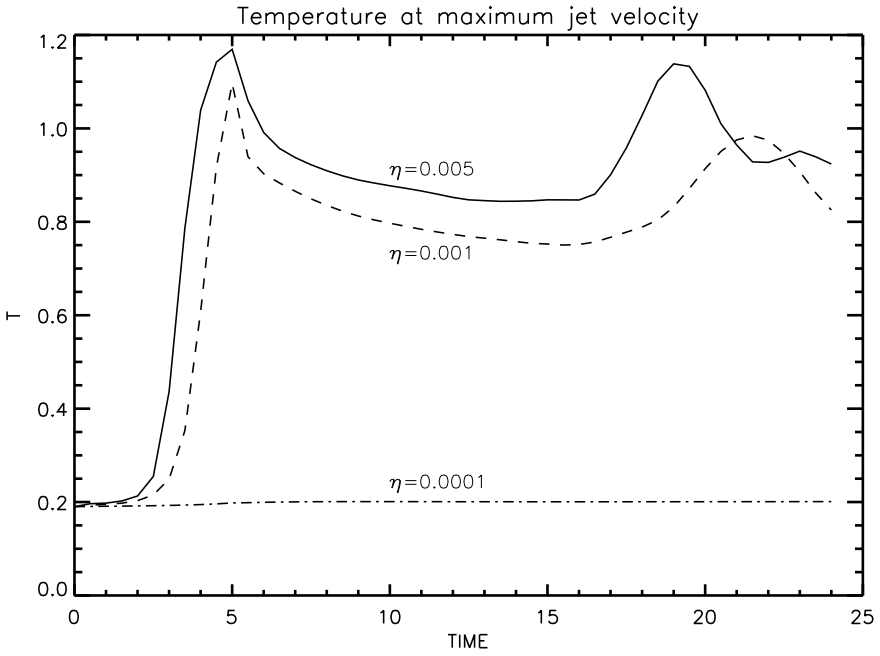

Figure 6.22: ROU02 case temperature at the reconnection point ($x^* = 0$)

6.5

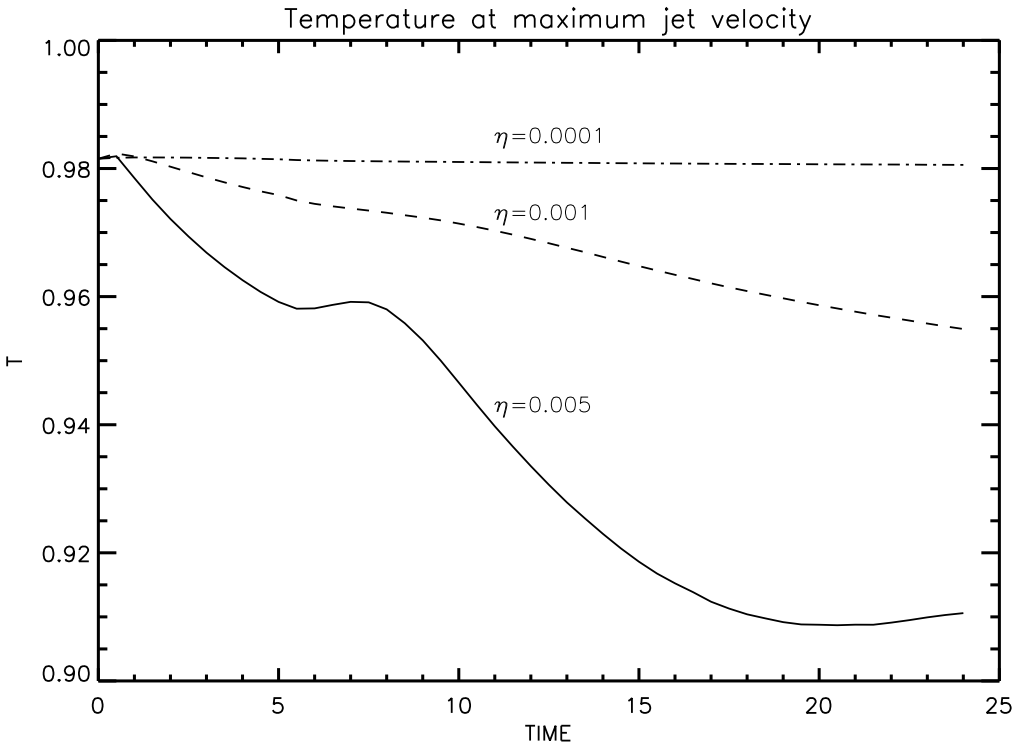

Figure 6.23: Our 'straight' case temperature at reconnection point ($x^* = 0, y^* = -0.5$)

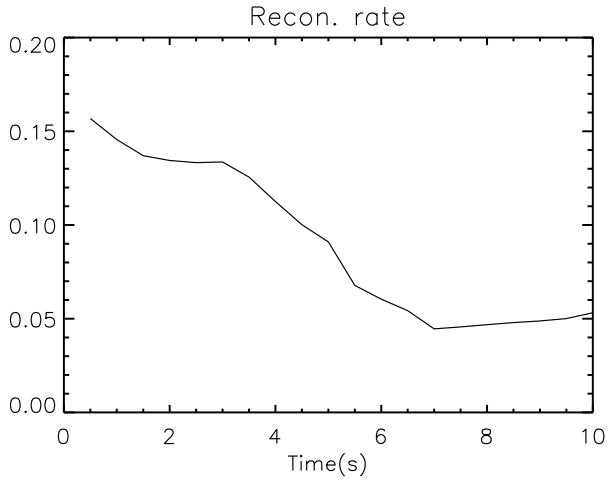

Figure 6.24: ROU02 case reconnection rate for $\eta = 0.005$

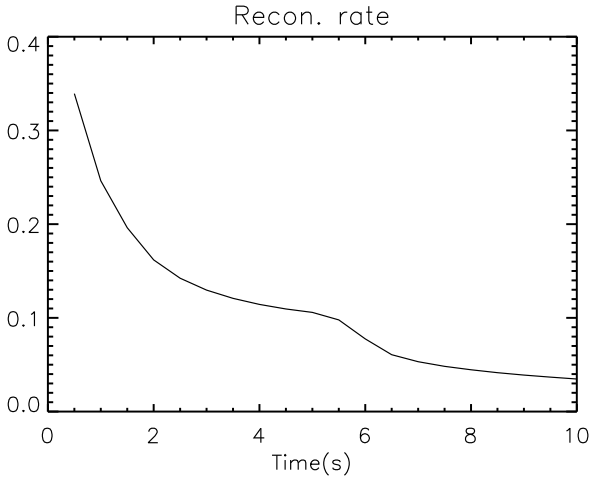

Figure 6.25: Our 'straight' case reconnection rate for $\eta = 0.005$

6.6

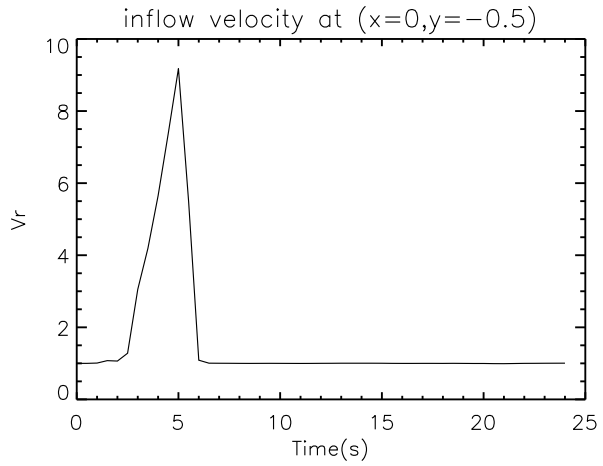

Figure 6.26: ROU02 case inflow velocity at $(x^* = 0, y^* = -0.5)$ for $\eta = 0.005$

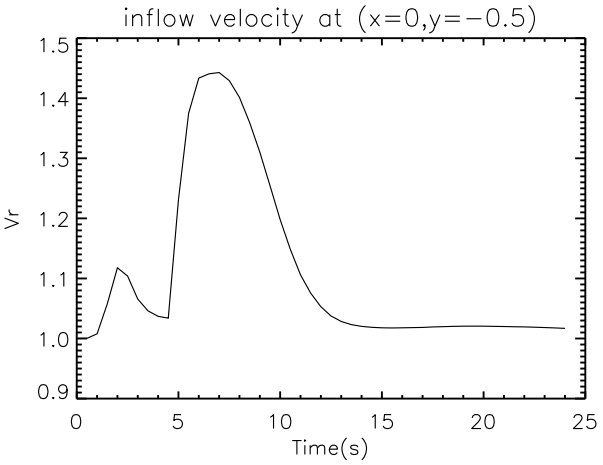

Figure 6.27: Our 'straight' case inflow velocity at $(x^* = 0, y^* = -0.5)$ for $\eta = 0.005$

Reconnection rates (inflow/outflow velocities) for both cases (ROU02 and our profile) show a small increase between $t^* \approx 4 - 6$ (see Figures 6.24 and 6.25). However in our case the speeds are of 2-3 orders of magnitude smaller due to the density and magnetic configuration that we proposed (see Figure 6.27 compared to Figure 6.26).

6.6 Hall MHD

Recent computational work by Birn et al. (2001) has demonstrated that the Hall term is important for collisionless reconnection. The relevant Hall phenomena is the decoupling of the ions from the magnetic field on length scales of the order of the ion inertial depth or less (see Arber 2006). This effect is included by using a generalized Ohms law in which the Hall term couples the motion of magnetic flux to the electrons rather than the ions. Introducing this term in a resistive simulation also generates Hall currents in regions where both the Hall term and resistivity are significant. However, these currents are always in the plane of the simulation and play no direct role in the reconnection process. Furthermore, Birn et al. (2001) treats fully ionized plasmas so that ion-neutral collisions, often important in other applications of the Hall physics of plasmas, are absent. Provided that the ion inertial length, $\lambda_i = c/\omega_{pi}$, where ω_{pi} is the ion plasma frequency and c is the vacuum speed of light, is larger than the scale on which the frozen-in condition is broken, the reconnection rate is insensitive to the precise mechanism responsible for reconnecting the magnetic field at a 2D X point (see, e.g. Hesse et al. 1999, Cassak et al. 2005). The ion inertial length is the length scale at which the Hall term becomes important in the generalized Ohm′s law. Thus, Hall MHD gets approximately the correct collisionless Petschek reconnection rate, provided the width of the central Sweet-Parker resistive region in the standard Petschek model is much less than the ion inertial length. When this condition is satisfied it has been shown that the Petschek reconnection rate is insensitive to the value of the resistivity (see, e.g. Bessho & Bhattacharjee 2007) and that the Hall reconnection rate is larger than the equivalent resistive MHD rate (see Lottermoser & Scholer 1997). The small η Hall reconnection rate is broadly in agreement with the steady Hall reconnection rate found with $\eta = 0$ (Huba and Rudakov 2004), i.e., numerical resistivity on grid scale, and the consensus view is therefore that for small resistivity, the Hall reconnection rate is the same as the collisionless result and is a constant. Here we do not deal with the general problem of collisionless reconnection but only the collisionless limit of the Hall MHD model. In addition, when we include the effect of the Hall term in our simulation, we can see that

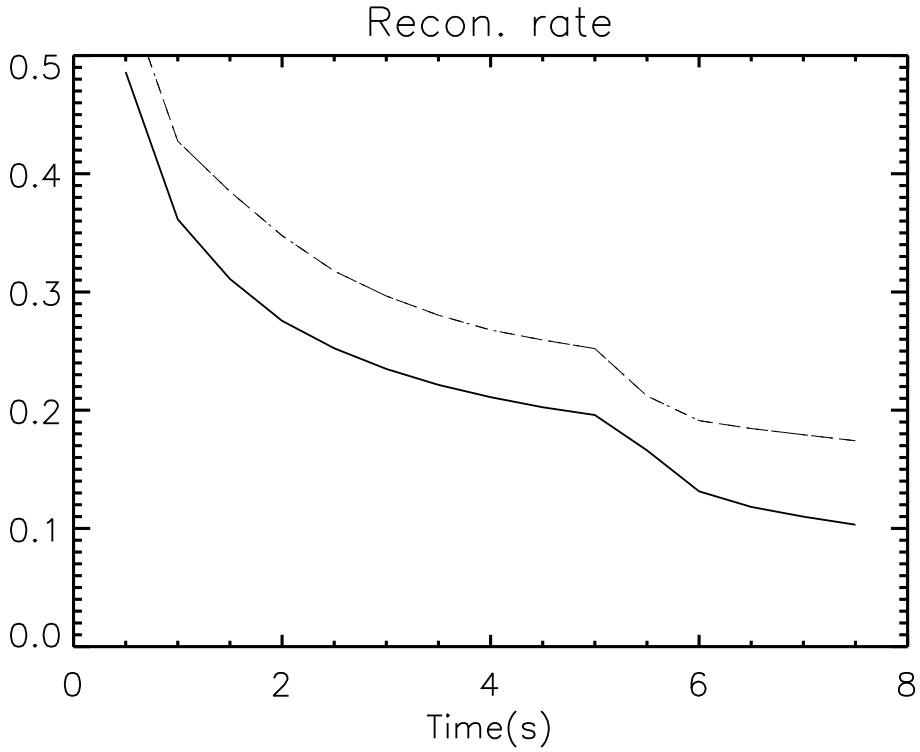

Figure 6.28: Reconnection rate for $\eta = 0.005$, dashed line represents reconnection rate with Hall term included and $\lambda_i = 0.005$, solid line represents the previous case without Hall effect.

the reconnection rate increases with parameter λ_i (dotted line see Figure 6.28). For values of $\lambda_i = 0.005$, the rate of reconnection increases with about 10%.

Further investigation with higher values of λ_i, would be more interesting. Unfortunately due to the limited resolution of the grids, when $\lambda \sim \lambda_i$, is to small, the simulation code leads too numerical instability. Future work with better resolution will be undertaken to fully explore the effects of Hall term.

6.7 Summary

We have examined the dynamical consequences of magnetic reconnection in a 2D stratified environment representing the 'quiet' Sun transition region. In a similar manner to Rousev et al. (2002), we investigated different initial states.

They were constructed by assigning different values of the resistivity parameter, η. In all the cases, the scale-height was kept constant unlike in Roussev et al. (2002). We focused, instead, on enhancing the stratification in density, which led to a change in the temperature profile for a slightly different magnetic field configuration, and studied the effect of resistivity and non-ideal effects (inclusion of Hall term) on the reconnection process.

In the early phases of the reconnection process, we discovered the same complicated double-oscillatory ('chess-mate' like) pattern of the vorticity like in ROU2. This is caused by initial deviations in the force balance, since the magnetic field is diffused away faster than the pressure gradient reacts on changes in the Lorentz force. As a result, the Lorentz force gets a double-wave pattern in the horizontal x-direction. This, combined with the very initial compressing effect of the Lorentz force in the vertical y direction, produces a complex pattern of the vorticity. The alternating signs of the vorticity were found to follow those of the Lorentz forces with respect to the x^* and y^* coordinates (see Figure 6.29). This initial phase is eventually suppressed and ultimately vanishes. This

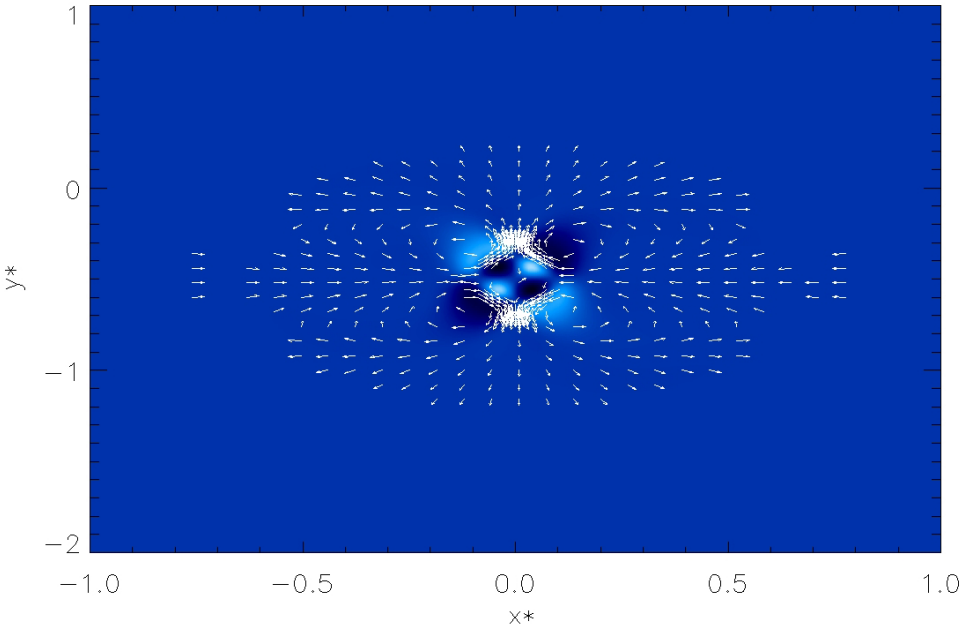

Figure 6.29: Reconnection rate for $\eta = 0.005$, at early stages $t^* = 0.5$

occurs at about the time when the advective term in the induction equation becomes comparable in magnitude to the diffusive term.

By comparing the three different experiments with $\eta = 0.0001$, $\eta = 0.005$, $\eta = 0.001$, we found that for resistivity $\eta = 0.005$ the reconnection process was faster, however, this rate was slower than in ROU2, due to strong stratification. The reconnection was triggered at about the same time $t^* = 6$, in both cases but the evolution was completely different mostly due to the fact that in our model the plasma β was constant with height unlike in ROU02. If the reconnection rates for both cases showed a small increase between $t^* = 4 - 6$, in our case the speeds were of 2-3 orders of magnitude smaller because of the magnetic field configuration and density stratification. Different values of η substantially change the dynamics of the reconnection process.

The inclusion of Hall term in the MHD equations did bring changes to the reconnection process with an increase of $\sim 10\%$ in the reconnection rates. In order to obtain a considerable increase in the reconnection rate, one would need to increase the ion inertial depth, λ_i. An extension of the model to 2.5D or 3D, could in principle change the behaviour of plasma β into decreasing function with height and also due to different gravity and density stratification reconnection could be faster. Such extensions should be investigated in future models.

In conclusion, we believe that our results give a different physical insight to the dynamical consequences of magnetic reconnection in stratified physical environment. Although our investigation involved 2D MHD in 'quiet' chromosphere, it can be expanded for other magnetic regions, by including a more realistic 3D profile. Pressure difference between the top and bottom of the magnetic configurations lead to plasma flows. It would be interesting to include such plasma flows in the equilibrium state and study the various regions and parameters for which the Kelvin-Helmholtz instability dominates the tearing instability and vice-versa.

Chapter 7

Discussions and Future Work

Motivated by earlier related studies, i.e. Andreis et al. (2005, 2009) & Roussev et al. (2001,2002), the present thesis work was dedicated to further explore the relationship between the composition of a plasma structure and the oscillations supported by the coronal loop and their link with magnetic reconnection through various 2-dimensional physical environments approximating the solar atmosphere.

The examined model situations differ from ideal MHD environment for the study of oscillations to those where the effects of gravity, resistivity and Hall term were taken into consideration for the study of magnetic reconnection. Ideal MHD was taken in consideration for the investigation of the effect of the environment, geometry on the period ratio, assuming that the density scale-heights (implicitly the temperature) inside and outside magnetic structures were different (Chapters 3 and 4). The same ideal MHD equations were used for the study of the emergence and expansion of a coronal loop through the solar atmosphere, which is a very complex phenomenon, but here we reduced our model to a simplified process, where the expansion was solely described by the change in the length of the loop with an associated temporal equilibrium density variation (in Chapter 5).

Using a simple mathematical method first applied in the context of loop oscillations by McEwan et al. (2008), we derived for the first time an analytical expression that connects the value of the period of kink oscillations and parameters of the loop. We found that in the case of coronal loops, the effect

of temperature difference between the loop interior and exterior can lead to changes of the order of 30-40%, that could have significant implications on the diagnosis of longitudinal density structure of the coronal loop. In the case of prominences, given the very large density and temperature difference between the prominence and coronal plasma, the changes in P_1/P_2 due to the different temperature are very small. For the study of expansion on coronal loop oscillations, our model predicts that the amplitude of oscillations increases with time, however due to the particular choice of density, damping processes were neglected. Once the density is allowed to vary also in radial direction, according to the theory of resonant absorption (see, e.g. Goossens et al. 1992, Rudeman and Roberts 2002), loops will damp very quickly with the resonant position, displaying a steady motion due to the change of the length of the loop. The amplitude of oscillations can also be damped due to the cooling of the plasma (Morton et al. 2010), an effect that was also neglected here. In an expanding loop, the growth of the amplitude due to emergence and decay of amplitude due to resonant damping or cooling will be competing processes and the competition between these two effects.

Once dispersive effects are taken into account the domain of applicability of P_1/P_2 seismology in the case of coronal loops becomes restricted and physically accepted solutions can not be found for any temperature ratio. For this one would need to consider that initial parameters (magnetic field, density, pressure, etc.) depend on more than one variable, therefore including extra dimensions will lead to non-trivial system of MHD equations. In such circumstances, the ideal MHD equations would not qualify for the description of a 3D magnetic field. We admit that our experiments are rather artificial, as the physical considerations involved in the study of P_1/P_2 seismology are not realistic. First we supposed that the loop is thin, and equation (3.1) can be applied to describe the dynamics of kink oscillations in coronal loops. It is obvious that this statement is not true for very short loops (the ratio of the loop ratio and its length is not very small) in which case, the governing equation has to be supplemented by an extra term. Secondly, our isothermal supposition of the loop and its environment is also that needs refinement as observations (see, e.g. Winebarger et al. 2003, Warren et al. 2008, Berger et al. 2011, Mulu-Moore 2011) show that the

loops are not always in hydrostatic equilibrium nor isothermal. Here we supposed the idealistic situation of a static background, however recent analysis by Ruderman (2011) showed that the the temporal dependence of density through flow and cooling can also influence the ratio of the two periods. This is a first step in the development of more advance non-ideal MHD experiments.

Further in Chapter 6, we examined the impact of resistivity on the dynamics of 2D magnetic reconnection. We adopted a rather simplified form of the resistivity (i.e. constant) due to limitation of the numerical code used in the simulations Lare2D, changed the initial parameters (magnetic field line, density, pressure, plasma beta) in such a way the are close to reality. Experiments have been conducted to investigate the impact of various resistivity on the time-dependent evolution of the magnetic reconnection process. Later we included a dispersive effect (Hall effect) and compared the differences between the two cases. The physical situations examined here are far too simplistic to mach any set of observations, as we did not take into consideration a 3D MHD. Nevertheless, we believe these results provide some of the essential physical intuition needed to assess the meaning of observations in terms of physical properties of the emitting plasma.

As for future work of relevance to coronal seismology, we intend to further investigate the expansion of a coronal loop in non-ideal environment. Starting off with consideration of non constant acceleration, inclusion of non-constant cross section, also taking into account that the coronal loop is not in an 'empty' environment and can interact with other entities throughout its expansion. Further use a different numerical approach in constructing a 2D and then a 3D coronal loop, then study the oscillation of this loop in a numerical environment, using wavelet analysis and trying to detect the difference between the values of periods detected here with compared to the previous studies.

On the magnetic reconnection process, we would try to develop a different initial state, first with a straight magnetic field, then with an open field line profile and later with an arcade, and study the time-depended evolution of magnetic reconnection. Inclusion of an initial incompressible flow profile would be considered, as pressure difference between the top and bottom of the magnetic configuration leads to plasma flows. We expect for this to observe tearing in-

stabilities in the reconnection process as well as formation of violently, unstable long current sheets and multiple plasmoid formation. A further analysis will be the study of magnetic reconnection in turbulent background.

Appendices

.1

.1 Corrections to the eigenfunctions due to the density stratification

In the Appendix we estimate the corrections to the chosen eigenfunctions due to the density stratification. Analytical progress can be made in the small y/χ limit. Since χ is a value smaller than one, this condition would automatically mean that we work in the small y limit, provided χ is not becoming too small. We are interested only in the characteristics of fundamental mode of kink oscillations and its first harmonic. Following equation (5.60) with the boundary conditions $v_r(L) = dv_r(0)/dz = 0$ and $v_r(0) = v_r(L) = 0$ for the fundamental mode and first harmonic, we introduce a new variable so that

$$\zeta = \frac{z}{L}, \quad \text{with} \quad \frac{\omega L}{\sqrt{2}v_{Ai}} = \Omega.$$

In the new notations the density inside the loop can be written as

$$\rho_i(\zeta) = \rho_i(0) \exp\left[\frac{h}{H_i} \sin\frac{\pi\zeta}{2}\right], \tag{1}$$

where h is the loop height above the solar atmosphere (a similar equation can be written for the external density). Next, we are working in the approximation $h/H_i = \epsilon \ll 1$, so equation (5.60) becomes

$$\frac{d^2v_r(\zeta)}{d\zeta^2} + \Omega^2\left[1 + \epsilon sin\left(\frac{\pi\zeta}{2}\right) + \frac{1}{\xi}\left(1 + \frac{\epsilon}{\chi} sin\left(\frac{\pi\zeta}{2}\right)\right)\right] v_r(\zeta) = 0, \tag{2}$$

where $\xi = \rho_i(0)/\rho_e(0) > 1$ is the density ratio and $\chi = H_e/H_i < 1$, with H_e and H_i being the density scale heights inside and outside the loop. Let us we write v_r and Ω as

$$v_r(\zeta) = v_r^{(0)}(\zeta) + \epsilon v_r^{(1)}(\zeta) + \mathcal{O}(\epsilon^2), \quad \Omega = \Omega_0 + \epsilon\Omega_1 + \mathcal{O}(\epsilon^2). \tag{3}$$

Substituting these expansions into equation (2) and collecting terms proportional to subsequent powers of ϵ we obtain

$$\frac{d^2 v_r^{(0)}}{d\zeta^2} + (1+\xi^{-1})\Omega_0^2 v_r^{(0)} = 0, \tag{4}$$

$$\frac{d^2 v_r^{(1)}}{d\zeta^2} + (1+\xi^{-1})\Omega_0^2 v_r^{(1)} + 2(1+\xi^{-1})\Omega_0\Omega_1 v_r^{(0)} + \\ +\Omega_0^2 v_r^{(0)} \left(1 + \frac{1}{\xi\chi}\right) sin\left(\frac{\pi\zeta}{2}\right) = 0. \tag{5}$$

These equations must be solved separately for the fundamental mode and its first harmonic taking into account the boundary conditions

- For the fundamental mode

$$v_r(\zeta = 1) = 0, \quad \frac{dv_r}{d\zeta}(\zeta = 0) = 0$$

- For the first harmonic

$$v_r(\zeta = 1) = v_r(\zeta = 0) = 0$$

Let us first calculate the correction to the fundamental mode. It is easy to show that the solution of equation (4) taking into account the above boundary condition becomes

$$v_r^{(0)}(\zeta) = \cos\left(\frac{\pi\zeta}{2}\right), \tag{6}$$

and

$$\Omega_0 = \frac{\pi}{2\sqrt{1+\xi^{-1}}}. \tag{7}$$

It is important to note that the form of the above solution is exactly the same as the solution we employed for the eigenfunction, v_r. In the next order of approximation we obtain equation (5) which can be written as

$$\frac{d^2 v_r^{(1)}}{d\zeta^2} + (1+\xi^{-1})\Omega_0^2 v_r^{(1)} =$$

.1

$$-2(1+\xi^{-1})\Omega_0\Omega_1 v_r^{(0)} - \Omega_0^2 v_r^{(0)}\left(1+\frac{1}{\xi\chi}\right) sin\left(\frac{\pi\zeta}{2}\right). \tag{8}$$

This boundary value problem will permit solutions only if the right-hand side satisfies the compatibility condition that can be obtained after multiplying the left-hand side by the expression of $v_r^{(0)}$ and integrating with respect to the variable ζ between 0 and 1, or

$$\int_0^1 v_r^{(0)}\left[2(1+\xi^{-1})\Omega_0\Omega_1 v_r^{(0)} + \Omega_0^2 v_r^{(0)}\left(1+\frac{\xi^{-1}}{\chi}\right) sin\left(\frac{\pi\zeta}{2}\right)\right] d\zeta = 0.$$

After some straightforward calculus we can find that

$$\Omega_1 = -\frac{1}{3(1+\xi^{-1})^{3/2}}\left(1+\frac{1}{\xi\chi}\right). \tag{9}$$

As a result, equation (5) becomes

$$\frac{d^2 v_r^{(1)}}{d\zeta^2} + \frac{\pi^2}{4} v_r^{(1)} = \frac{\pi\left(\xi+\frac{1}{\chi}\right)}{(1+\xi)}\left[\frac{1}{3}\cos\left(\frac{\pi\zeta}{2}\right) - \right.$$

$$\left. -\frac{\pi}{4}\sin\left(\frac{\pi\zeta}{2}\right)\cos\left(\frac{\pi\zeta}{2}\right)\right] = 0. \tag{10}$$

This differential equation will have the solution

$$v_r^{(1)}(\zeta) = C_1 \sin\left(\frac{\pi\zeta}{2}\right) + C_2\cos\left(\frac{\pi\zeta}{2}\right)$$

$$+\frac{\left(\xi+\frac{1}{\chi}\right)}{3\pi}\frac{2\cos\left(\frac{\pi\zeta}{2}\right)+\pi\zeta\sin\left(\frac{\pi\zeta}{2}\right)+\frac{\pi}{2}sin(\pi\zeta)}{(1+\xi)}. \tag{11}$$

Applying the boundary condition $v_r^{(1)}(\zeta=1)=0$, we find the constant

$$C_1 = -\frac{\left(\xi+\frac{1}{\chi}\right)}{3(1+\xi)}.$$

.1

In order to find the value of C_2, we use the property of orthogonality, i.e.

$$\int_0^1 v_r^{(0)} v_r^{(1)}\, d\zeta = 0,$$

which result in

$$C_2 = -\frac{7}{9}\frac{\left(\xi + \frac{1}{\chi}\right)}{(1+\xi)\pi}.$$

As a result, the first order correction to v_r corresponding to the fundamental mode is

$$v_r^{(1)} = \frac{\left(\xi + \frac{1}{\chi}\right)}{(1+\xi)}\left[-\frac{1}{3}\sin\left(\frac{\pi\zeta}{2}\right) - \frac{7}{9\pi}\cos\left(\frac{\pi\zeta}{2}\right)\right] +$$

$$+\frac{\left(\xi + \frac{1}{\chi}\right)}{(1+\xi)}\left[\frac{1}{3\pi}2\cos\left(\frac{\pi\zeta}{2}\right) + \pi\zeta\sin\left(\frac{\pi\zeta}{2}\right) + \frac{\pi}{2}\sin(\pi\zeta)\right]. \qquad (12)$$

In Figure 1 we plot the correction to the eigenfunction for $\epsilon = 0.1$, $\chi = 0.9$, and $\xi = 10$. Figure (1) shows that we can approximate $v_r(z)$ by $\cos(\pi z/2L)$ since the first order correction brings changes of about $1(\%)$, i.e. insignificant.

.2

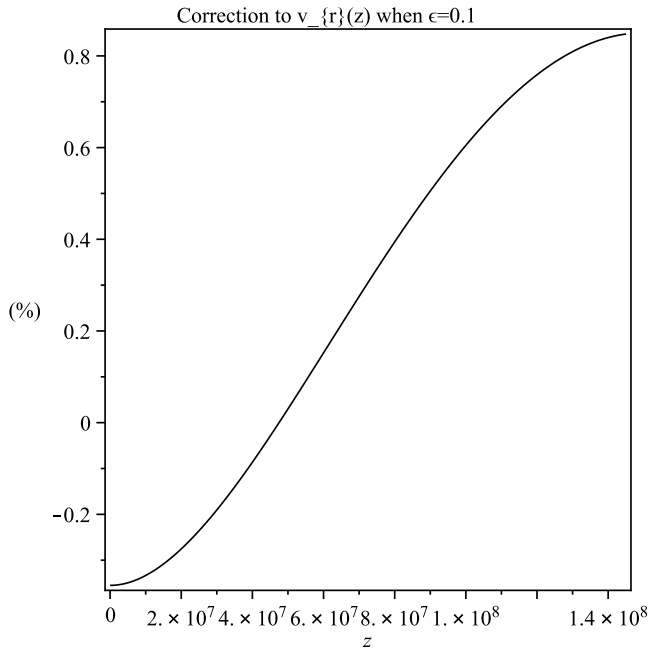

Figure 1: Correction to the eigenfunction for the fundamental mode kink oscillation when $\epsilon = 0.1$. Here $L = 1.5 \times 10^8$ m represents the loop length

.2 Corrections to the first harmonic

The same analysis can be repeated for the first harmonic, taking into account the right boundary conditions. After a straightforward calculation it is easy to show that

$$v_r^{(0)}(\zeta) = sin(\pi\zeta), \tag{13}$$

$$\begin{aligned} v_r^{(1)}(\zeta) = & \frac{\xi + 1/\chi}{1+\xi} \cdot \left[-\frac{176}{225\pi} \sin(\pi\zeta) + \frac{4}{15} \cos(\pi\zeta) \right] \\ & - \frac{16}{15\pi} \frac{\xi + 1/\chi}{1+\xi} \left[\frac{5\pi}{32} \cos\left(\frac{\pi\zeta}{2}\right) + \frac{3\pi}{32} \cos\left(\frac{3\pi\zeta}{2}\right) \right] \\ & - \frac{16}{15\pi} \frac{\xi + 1/\chi}{1+\xi} \left[\frac{\pi\zeta}{2} \cos(\pi\zeta) - \frac{1}{2} \sin(\pi\zeta) \right]. \end{aligned} \tag{14}$$

The correction to the eigenfunction corresponding to the first harmonic has been plotted in Figure 2 for the same values as before. It is obvious that the changes introduced by stratification in the value of the eigenfunction are of the

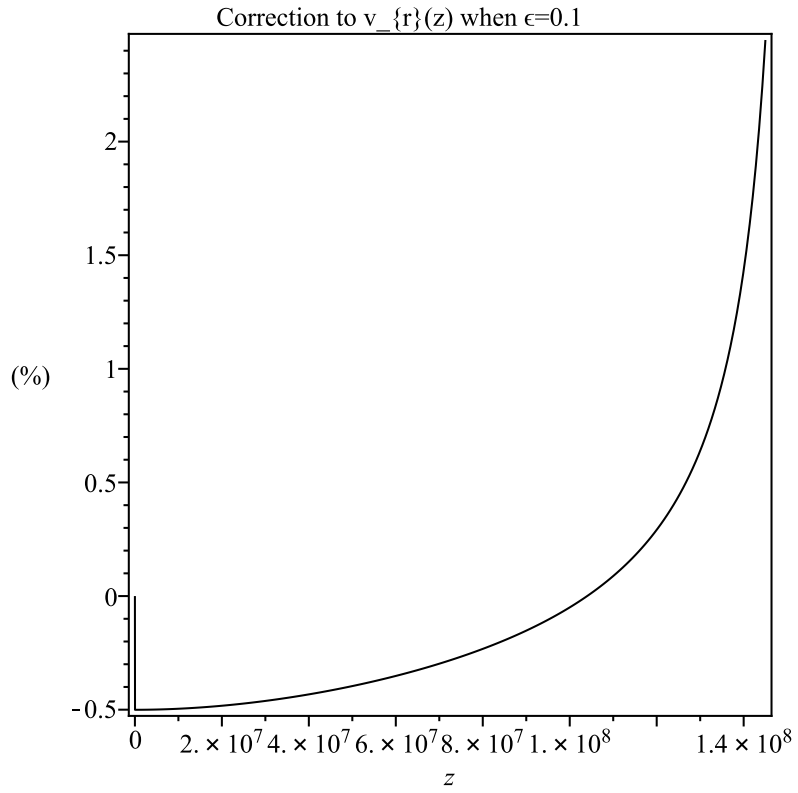

Figure 2: The same as Figure 1 but here we represent the correction to the eigenfunction for the first harmonic kink oscillation.

order of 2(%), i.e. negligably small. The two figures show that the effect of density stratification becomes more important for higher harmonics. Given the very large values of χ we used for prominences, the approximations used in this Appendix will always be valid. For the graphical representation of corrections in Figs 1 and 2 we used $\chi = 1$. If we lower this value to, e.g. 0.7 the corrections would still be small since the maximum relative change in the eigenfunction describing the fundamental mode would be 1.1 %, while for the first harmonic, this would increase to 3.5 %.

The robustness of our analysis was checked using a full numerical investigation for arbitrary values of χ and y. A typical dependence of the P_1/P_2 period ratio with respect to $L/\pi H_i$ for one value of χ is shown in Figure 3 where the solid line corresponds to the analytical and the dotted line represent the

.2

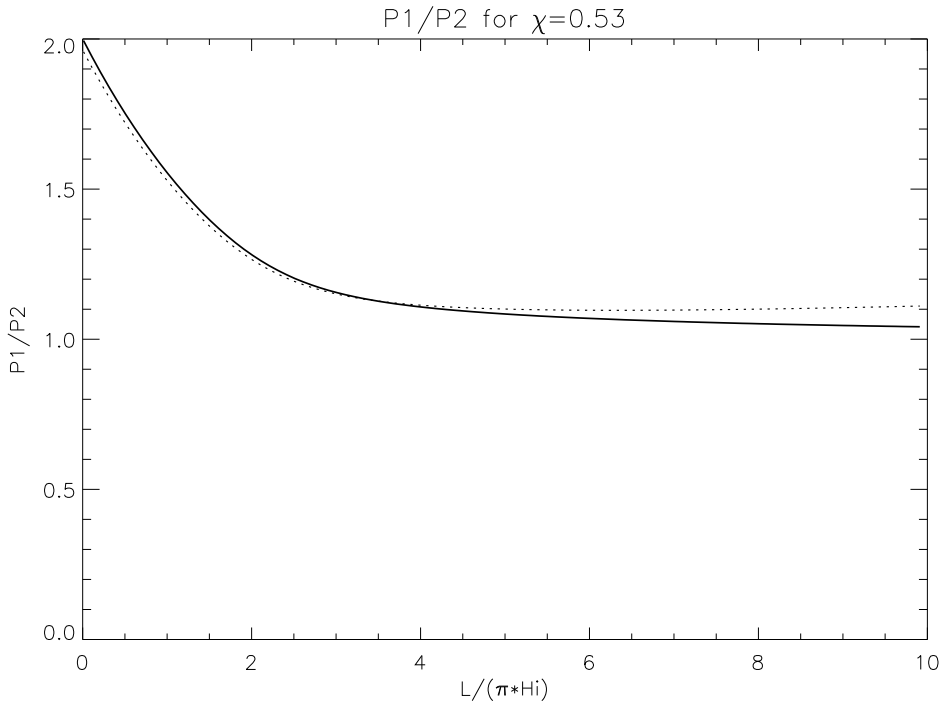

Figure 3: Comparison of the analytical (solid line) and numerical (dotted line) results for the P_1/P_2 variation with $L/\pi H_i$ for coronal case corresponding to $\chi = 0.53$.

numerical results, in both cases the density is inhomogeneous with respect to the coordinate z. The loop is set into motion using a Gaussian-shaped source and we use a full reflective boundary conditions at the two footpoints of the loop. After the oscillations are formed, we use the FFT procedure to obtain the values of periods. Our analysis shows that the differences between the results obtained using the variational method and a full numerical investigation are of the order of 7% but towards the large range of $L/\pi H_i$. Restricting ourself to realistic values, i.e. $L/\pi H_i < 5$, we see that the results obtained with the two methods coincide with great accuracy.

Bibliography

[1] Abramowitz, M., Stegun, I. A., 1964, *Handbook of Mathematical Functions*

[2] Andries, J., Arregui, I., & Goossens, M., 2005, Astrophys. J. Lett., 624, L57

[3] Andries, J., van Doorsselaere, T., Roberts, B., Verth, G., Verwichte, E., & Erdélyi, R., 2009, Space Science Rev., 149, 3

[4] Archontis, V., Moreno-Insertis, F., Galsgaard, K., et al. 2004, A&A, 426, 1047

[5] Archontis, V., 2008, J. Geophys. Res., 113, A03S04

[6] Arber, T. D., Longbottom, A. W., Gerrard, C. L., and Milne, J., 2001, J. Comput. Phys., 171, 151-181

[7] Arber, T. D., and Haynes, M., 2006, Phys. Plasmas, 13, 112105

[8] Arregui, I., Oliver, R., & Ballester, J. L., 2012, Living Rev. Sol. Phys, 9, 2

[9] Aschwanden, M.J., 1987, Sol. Phys. 111, 113-136

[10] Aschwanden, M.J., Schrijver, C.J., Winebarger, A.R., et al. 2003a, ApJ, 588, L49

[11] Aschwanden, M. J., de Pontieu, B., Schrijver, C. J., & Title, A. M., 2002, Sol. Phys., 206, 99

[12] Aschwanden, M. J., 2004, Physics of the Solar Corona, Springer-Verlag, Berlin

.2

[13] Aschwanden, M. J.., & Schrijver, C. J., 2011, ApJ, 736, 102

[14] Ballai, I., Erdélyi, R., & Pintér, B., 2005, Astrophys. J. Lett., 633, L145

[15] Ballai, I., Erdélyi, R. & Hargreaves, J., 2006, Phys. Plasmas, 14, 042108

[16] Ballai, I., 2007, Sol. Phys., 246, 177

[17] Ballai, I., Forgács-Dajka, E. & Marcu, A., 2007, Astron. Nachr., 328, 734

[18] Ballai, I., Douglas, M., & Marcu, A., 2008, A&A, 488, 1125

[19] Ballai, I., Jess, D., & Douglas, M., 2011, A&A, 534, 13

[20] Ballai, I., & Orza, B., 2012, A&A, 545, A118

[21] Baty, H., Priest, E. R., and Forbes, T. G., (2009a), Phys. Plasmas 13, 022312/17

[22] Baty, H., Priest, E. R., and Forbes, T. G., (2009b), Phys. Plasmas 16, 012102/16

[23] Beckers, J.M., 1972, Ann. Rev. Astron. & Astrophys., 10,73

[24] Berger, T., Testa, P., Hillier, A. et al. 2011, Nature, 472, 197

[25] Bray, R. J., & Loughhead, R. E., 1964, Sunspots (New York: Wiley)

[26] Bender, M. & Ország, S.A. 1987, Advanced Mathematical Methods for Scientists and Engineers, McGraw-Hill, Singapore

[27] Bessho, N. & Bhattacharjee, A. 2007, Phys. Plasmas, 14, 056503

[28] Bharti, L., Joshi, C., & Jaaffrey, S. N. A. 2007, ApJ, 669, L57

[29] Bhattacharjee, A. et al. 2005, Phys. Plasmas, 12, 042305

[30] Birn, J., et al. 2001, Geophys. Res., 106, 3715

[31] Birn, J., et al. 2005, Geophys. Res. Lett., 32, L06105

[32] Birn, J. and Priest, E. R., 2007, *Magnetic Reconnection in Plasmas*, Cambridge University Press

[33] Biskamp, D., 1986, Phys. Fluids, 29, 1520

[34] Biskamp, D., 2000, *Magnetic Reconnection in Plasmas*, Cambridge University Press

[35] Breslau, J. A., and Jardin, S. C., 2003, Phys. Plasmas, 10, 1291

[36] Brueckner, G. E., & Bartoe, J.-D. F., 1983, ApJ, 272, 329

[37] Cassak, P. A., Shay, M. A., and Drake, J. F., 2005, Phys. Rev. Lett., 95, 235002

[38] Cassak, P.A., et al. 2006, ApJ, 644, 2145

[39] Chae., J., Wang, H., Lee, C.-Y., Goode, P. R., & Schuhle, U., 1998, ApJ, 497, L109

[40] Chen, P.F., et al. 1999, ApJ, 513, 516

[41] Chou, D.-Y. & Zirin, H., 1988, ApJ, 333, 420

[42] Colgate, S. A., Li, H., Pariev, V., 2001, Phys. Plasmas, 8, 2425

[43] Cooper, F.C., Nakariakov, V.M. & Tsiklauri, D., 2003, A&A, 397, 765-770

[44] Cothran, C. D., Falk, A., Fefferman, A., Landerman, M., Brown, M. R., Schafer, M. J., 2003, Phys. Plasmas, 10, 1748

[45] Cowling, T. G., 1975, Nature, 255, 189

[46] Craig, J.I.D., & Litvinenko, Y.E., 2008, A&A, 484, 847

[47] Craig, J.I.D., & Watson, P.G., 2003, Solar Phys., 214, 131

[48] Craig, J.I.D., & Watson, P.G., 2005, Phys. Plasmas, 12, 12306

[49] De Moortel, I., & Brady, C. S., 2007, ApJ, 664, 1210

.2

[50] De Pontieu, B. & Erdélyi, R. , 2006, Royal Society of London Philosophical Transactions Series A 364, 383-394

[51] De Pontieu, B., McIntosh, S. W., Hansteen, V. H., & Schrijver, C. J., 2009, ApJ, 701, L1

[52] De Pontieu, B., & McIntosh, S. W., 2010a, ApJ, 722, 1013

[53] Dere, K.P., et al. 1991, Geophys. Res., 96, 9319

[54] Dere, K. P., & Mason, H. E., 1993, Sol. Phys., 144, 217

[55] Dere, K. P., 1994, Adv. Space Res, 14, 13

[56] Diaz, A.J., Donelly, G.R., & Roberts, B., 2007, A&A, 476, 359

[57] Donea, A.-C., Besliu-Ionescu, D., Cally, P. S., Lindsey, C., Zharkova, V. V., 2006, Sol. Phys., 239, 113

[58] Dorelli, J.C., 2003, Phys. Plasmas, 10, 3309

[59] Doyle, J. G., Ishak, B., Ugarte-Urra, I., Bryans, P., & Summers, H. P., 2005, A&A, 439, 1183

[60] Dungey, J.W., 1953, Phil. Mag 44, 725-738

[61] Dymova, M. V. & Ruderman, M. S., 2005, Sol. Phys.229, 79

[62] Dymova, M. V. & Ruderman, M. S., 2006, A&A457, 1069

[63] Edwin, P. M., & Roberts, B., 1983, Sol. Phys., 88, 179

[64] Erdélyi, R., & Ballai, I., 2007, Astron. Nachr., 328, 726

[65] Eto, S., et al. 2002, *PASJ*, 54, 481

[66] Falconer, D. A., Moore, R. L., Porter, J. G., Gary, G. A., Shimizu, T., 1995, ApJ, 482, 519

[67] Forbes, T., & Priest, E.R., 1984, Solar Phys., 94, 315

[68] Furth, H. P., Killeen, J., and Rosenbluth, M. N., 1963, Phys. Fluids 6, 459-484

[69] Frey, H. U., Phan, T. D., Fuselier, S. A., & Mende, S. B., 2003, Nature, 426,533

[70] Gabriel, A. H., et al. 1997, Sol. Phys., 175, 207

[71] Garciá de la Rosa, J.I., 1987, Sol. Phys., 112,49

[72] Gary, S.P., 2002, Phys. Plasmas, 9, 2437

[73] Golub, L., J. Bookbinder, E. Deluca, M. Karovska, H. Warren, C. J. Schrijver, R. Shine, T. Tarbell, A. Title, J. Wolfson, B. Handy, and C. Kankelborg, 1999, Phys. Plasmas 6, 2205

[74] Goossens, M., Hollweg, J.V. & Sakurai, T., 1992, Sol. Phys., 138, 233

[75] Grossmann-Doerth, U., Schmidt, W., & Schrter, E. H., 1986, A&A, 156, 347

[76] Hara, H., et al. 2008, ApJ, 678, L67

[77] Harra, L.K., Magara, T., Hara, H. et al. 2010, Sol. Phys., 263, 105

[78] Harra, L.K., Archontis, V., Pedran, E. et al. 2012, Sol. Phys., 278, 47

[79] Harris, E.G., Nuovo Cimento, 1962, 23, 115

[80] Hasan, S. S., Kalkofen, W., van Ballegooijen, A.A., & Ulmschneider, P., 2003, ApJ, 585, 1138

[81] Hesse, M., Schindler, K., Birn, J., and Kuznetsova, M., Phys. Plasmas, 1999, 6, 1781

[82] Hindman, B. W. & Jain, R., 2008, ApJ, 677, 769

[83] Huba, J. D., 2003, Springer, New York, 170197

[84] Huba, J. D., and Rudakov, L. I., 2004, Phys. Rev. Lett., 93, 175003

.2

[85] Isobe, H., & Tripathi, D., 2007, A&A, 449, L17

[86] Innes, D. E., Inhester, B., Axford, W. I., & Wilhelm, K. 1997, Nature, 386, 811

[87] Innes, D. E., & Toth, G., 1999, Sol. Phys., 185, 127

[88] Isobe, H., Proctor, M. R. E., & Weiss, N. O., 2008, ApJ, 679, L57

[89] Innes, D. E., 2001, A&A, 278, 1067

[90] Jamitzky, F., & Scholer, M., 1998, J. Geophys. Res., 100, 19277

[91] Jain, R., & Hindman, B. W., 2012, A&A, 545, A138

[92] Jess, D. B., Mathioudakis, M., Erdelyi, R., Verth, G., McAteer, R. T. J., & Keenan, F. P., 2008, ApJ, 680, 1523

[93] Ji H, Prager SC, Sarff JS. 1995. Phys. Rev. Lett. 74:2945

[94] Ji H, Yamada M, Hsu S, Kulsrud RM., 1998. Phys. Rev. Lett. 80:3256

[95] Ji H, Yamada M, Hsu S, Kulsrud RM, Carter T, Zaharia S., 1999. Phys. Plasmas 6:1743

[96] Jing, J. et al. 2003, ApJ, 584, L103

[97] Klimchuk., 2006, Sol. Phys., 234, 41

[98] Khodachenko, M., Haerendel, G., Rucker, H. O., 2003, A&A, 401, 721-732

[99] Kjeldseth Moe, O., & Nicolas, K. R., 1977, ApJ, 211, 579

[100] Knobloch, E., Weiss, N.O., 1984, Man. Not. R. astr. Soc. 207, 203-214

[101] Kosovichev, A. G. & Zharkova, V. V., 1998, Nature, 393, 317

[102] Kulsrud, R., 1998, Phys. Plasmas 5, 1599

[103] Labrosse, N., et al. 2010, ApJ, 714, 636-643

[104] Levinton FM, Batha SH, Yamada M, Zarnstorff MC. 1993. Phys. Plasmas B 5:2554

[105] Lighthill, M. J., 1960, Proceedings of the Royal Society A, 252:297-430

[106] Lin, R. P., et al. 2003, Astrophys. J. Lett. 595, L69.

[107] Linton, M. G., and Priest, E. R., 2003, ApJ, 595, 1259

[108] Linker, J. A., Mikic, Z., Lionello, R., Riley, P., Amari, T., Odstrcil, D., 2003, 10, 1971

[109] Lites, B. W., Bida, T. A., Johannesson, A., & Scharmer, G. B. 1991, ApJ, 373, 683

[110] Litvinenko, Y. E. & Chae, J., 2009, A&A, 495, 953

[111] Long, D. M., Gallagher, P. T., James McAteer, R. T., & Bloomfield, S., 2008, ApJ, 680, L81

[112] Lorrain, P., & Koutchmy, S., 1996, Solar Phys, 165, 115

[113] Lottermoser, R. F., and M. Scholer, J., 1997, Geophys. Res., 102, 4875

[114] Mackay, D. H., Karpen, J. T., Ballester, J. L., Schmieder, B., & Aulanier, G. 2010, Space Sci. Rev., 151, 333

[115] Madjarska, M. S., & Doyle, J. G., 2002, A&A, 382, 319

[116] Madjarska, M. S., & Doyle, J. G., 2003, A&A, 403, 731

[117] Madjarska, M. S., Doyle, J. G., Hochedez, J.-F., & Theissen, A., 2006, A&A, 452, L11

[118] Madjarska, M. S., Doyle, J. G., & de Pontieu, B., 2009, ApJ, 701, 253

[119] Malyshkin, L. M., Lindé, T., Kulsrud, R. M., 2005, Phys. Plasmas, 12, 102902

[120] Mandt, M.E., et al. 1994, Geophys. Res. Lett., 21, 73

.2

[121] Martínez-Sykora, J., De Pontieu, B., Hansteen, V., & McIntosh, S.W., 2011, ApJ, 732, 84

[122] Martnez Gonzlez, M. J., Asensio Ramos, A.,Manso Sainz, R., et al. 2011, ApJ,730, L37

[123] Masuda, S., T. Kosugi, H. Hara, S. Tsuneta, and Y. Ogawara,1994, Nature, London, 371, 495

[124] McEwan, M. P., Donnelly, G. R., Díaz, A. J., & Roberts, B., 2006, A&A, 460, 893

[125] McEwan, M. P., Díaz, A. J., & Roberts, B., 2008, A&A, 481, 819

[126] McLaughlin, J.A., Ofman, L., 2008, ApJ, 682, 1338

[127] Meirovitch, L., 1970, Methods of Analytical Dynamics, McGraw-Hill, Michigan, USA

[128] Moreno-Insertis, F., Galsgaard, K, & Ugarte-Urra, I., 2008, ApJ, 673, L211

[129] Moreton, G.E., Ramsey, H.E., 1960, Astron. Soc., 72,357

[130] Morton, R. & Erdélyi, R., 2009, A&A, 502, 315

[131] Morton, R.J., Hood, A.W. & Erdélyi, R., 2010, A&A, 512, 23

[132] Morton, R. & Ruderman, M.S., 2011, A&A, 527, 53

[133] Morton, R., Ruderman, M.S. & Erdélyi, R., 2011, A&A, 534, 27

[134] Mozer, F.S., et al. 2002, Phys. Rev. Lett., 89, 015002

[135] Mulu-Moore, F.M., Winebarger, A. R., Warren, H. P., & Aschwanden, M.J, 2011, ApJ, 733, 59

[136] Murray, M. J., van driel-Gesztelyi, L, & Baker, D., 2009, A&A, 494, 329

[137] Murawski, K. & Musielak, Z. E., 2010, A&A, 518, 37

[138] Musielak, Z. E. & Ulmschneider, P. 2003b, A&A, 406, 725

[139] Nagayama Y, Yamada M, Park W, Fredrickson ED, Janos AC, et al. 1996. Phys. Plasmas 3:1647

[140] Nakariakov, V. M., Ofman, L., Deluca, E. E., Roberts, B., & Davila, J. M., 1999, Science, 285, 862

[141] Nakariakov, V. M., Ofman, L., 2001, A&A, 372, 253

[142] Nakariakov, V. M., Melnikov, V. F., & Reznikova, V. E., 2003, A&A, 412, L7

[143] Narukage, N., Hudson, H. S., Morimoto, T., et al. 2002, ApJ, 572, L109

[144] Ofman, L., Aschwanden, M.J., 2002, ApJ, 576, L153-L156

[145] Ofman, L. & Wang, T. J., 2008, A&A, 482, 9

[146] Ogrodowczyk, R., & Murawski, K., 2007, A&A, 467, 311

[147] Okamoto, T. J., Nakai, H., & Keiyama, A., 2004, ApJ, 608, 1124

[148] Oieroset, M., Lin, R. P, Phan, T. D., Larson, D. E., Bale, S. D., 2002, Phys. Rev. Lett, 89, 195001

[149] Orza, B., Ballai, I., Jain, R. & Murawski, K., 2012, A&A, 537, 41

[150] Orza, B. & Ballai, I., 2013, Astron. Nachr., 334, 948-951

[151] Owen, N. R., De Moortel, I., & Hood, A. W., 2009, A&A, 494, 339

[152] Parker, E.N., 1955, ApJ, 122, 293

[153] Parker, E.N., 1957, J. Geophys. Res., 509-520

[154] Parker, E. N. 1979, ApJ, 234, 333

[155] Parker, E.N., 1988, ApJ, 326, 407

[156] Patsourakos, S., & Vial, J. C., 2002, A&A, 385, 1073

.2

[157] Patsourakos, S., & Klimchuk, J. A., 2006, ApJ, 647, 1452

[158] Patsourakos, Spiros, Vourlidas, Angelos, 2009, ApJLetters, 700,L182

[159] Peter, H. 2001, A&A, 374, 1108

[160] Peter, H. 2010, A&A, 521, A51

[161] Petschek, H.E., 1964, AAS-NASA Symposium on the Physics of Solar Flares. (NASA Spec. Publ. SP-50, Washington), 425439

[162] Pilkelnér, S.B., 1969, Azh, 46, 328

[163] Pintér, B., Jain, R., Tripathi, D., & Isobe, H., 2008, ApJ, 680, 1560

[164] Phan T. D., et al. 2006, Nature, 439, 175

[165] Porter, J. G., Moore, R.L., Reichman, E.J., Engvold, O., & Harvey, K.L., 1987, ApJ, 323, 380

[166] Priest, E.R., 1978, Sol. Phys., 58:57-87

[167] Priest, E. R., 1982, Solar Magnetohydrodynamics, D. Reidel, Holland

[168] Priest, E. R. and Forbes, T. G., 1986, J. Geophys. Res. 91, 55795588

[169] Priest, E. R. and Demoulin, P., 1995, J. Geophys. Res. 100, 23,44323,463

[170] Priest, E. R. and Titov, V. S., 1996, Phil. Trans. Roy. Soc. Lond. 355, 29512992

[171] Priest, E.R., 1998, Astro Space Sci., 264, 77

[172] Priest, E.R., & Forbes, T., 2000, *Magnetic Reconnection*, Cambridge University Press

[173] Priest, E. R., Hornig, G., and Pontin, D. I., 2003, J. Geophys. Res. 108, A7, SSH 6.16.8

[174] Priest, E. R. and Hornig, G., 2009, Living Reviews in Solar Physics

[175] Priest, E. R. and Pontin, D. I., 2009, Phys. Plasmas 16, 122101

[176] Rae, I. C. & Roberts, B., 1982, ApJ, 256, 761

[177] Ramsey, H.E., & Smith, S. F., 1966, *AJ*, 71, 197

[178] Reale, F., Bocchino, F. and Peres, G., 2002, A&A, 383, 952971

[179] Reale, F., 2003, Adv. Space Res., 32, 10571066

[180] Ren, Y., et al. 2003, Phys. Rev. Lett, 95, 055003

[181] Roberts, W.O., 1945, ApJ, 101, 136

[183] Roberts, B., 1981a, Sol. Phys., 69, 27

[183] Roberts, B., 1981b, Sol. Phys., 69, 39

[184] Roberts, B., Edwin, P. M., & Benz, A. O., 1984, ApJ, 279, 857

[185] Roussev, I., Galsgraad, K., Erdélyi, R., & Doyle, J. G., 2001, A&A, 370, 298

[186] Roussev, I., Galsgraad, K., Erdélyi, R., & Doyle, J. G., 2001a, A&A, 275, 228

[187] Roussev, I., Galsgraad, K., Erdélyi, R., & Doyle, J. G., 2001b, A&A, 380, 719

[188] Roussev, I., and Galsgraad, K., 2002, A&A, 657-705

[189] Roussev, I., and Galsgraad, K., 2002, A&A, 685-696

[190] Ruderman, M. S., & Roberts, B., 2002, ApJ, 577, 475

[191] Ruderman, M. S., Verth, G., & Erdélyi, R., 2008, ApJ, 686, 694

[192] Ruderman, M. S., & Erdélyi, R., 2009, Space Science Rev., 149, 199

[193] Ruderman, M. S. 2010, Sol. Phys., 267, 377

[194] Ruderman, M. S., 2011, Sol. Phys., 271, 41

.2

[195] Ruderman, M. S. 2011b, A&A, 534, 78

[196] Ryutov, D. A., & Ryutova, M. P., 1976, Soviet Phys. JETP, 43, 491

[197] Sakurai, T., Ichimoto, K., Raju, K. P., & Singh, J., 2002, Sol. Phys., 209, 265

[198] Saro, L. M., Erdélyi, R., Doyle, J. G., & Perez, M. E., 1999, A&A, 351, 721

[199] Schindler, K., Hesse, M., and Birn, J., 1988, J. Geophys. Res. 93, 55475557

[200] Schmidt, J. M. & Ofman, L., 2011, ApJ, 739, 75

[201] Secchi, A., 1877, Le Soleil, 2, Gauthier-Vollars, Paris

[202] Selwa M., Murawski K., Wang, T. J., & Shumlak, U., 2006a, A&A, 454,653

[203] Shay, M. A. and Drake, J. F., 1998, Geophys. Res. Lett. 25, 37593762

[204] Shay, M. A., Drake, J. F., Swisdak, M., Rogers, B. N., 2004, Phys. Plasmas, 11, 2199

[205] Shibata, K., S. Masuda, M. Shimojo, H. Hara, T. Yokoyama, S. Tsuneta, T. Kosugi, and Y. Ogawara, 1995, ApJ, 451, L83.

[206] Sobotka, M. 2006, Diss. Doctor Scientiarum, Acad. Sci. Czech Republic

[207] Solanki, S. K. 2003, A&ARev., 11, 153

[208] Soward, A. M. and Priest, E. R., 1977, Phil. Trans. Roy. Soc. A284, 369417

[209] Spruit, H. C., 1982, Sol. Phys., 75, 3

[210] Sweet, P. A., 1958a, Cambridge University Press, 124134

[211] Taroyan, Y., 2008, IAU Symp. 247, Cambridge Univ. Press, 184

[212] Tajima, T., Sakai, J., Nakajima, H., Kosugi, T., Brunel, F., Kundu, M.R., 1987, ApJ, 321, 1031-1048.

[213] Takeuchi, A., & Shibata, K., 2001, ApJ, 546, L73

[214] Teriaca, L., et al. 2005, A&A, 427, 1065

[215] Tian, H., Marsch, E., Curdt, W., & He, J. 2009, ApJ, 704, 883

[216] Thompson, B.J., Gurman, J.B., Neupert, W.M., Newmark, J.S.,Dellaboudiniére, J.-P., St., Gyr, O.C., Stezelberger, S.,Dere, K.P., Howard, R.A., Michels, D.J., 1999, ApJ, 517, L151

[217] Tomczyk, S., McIntosh, S.W., Keil, S. L., et al. 2007, Science, 317, 1192

[218] Tsuneta, S., 1996, ApJ, 456, 840

[219] Uchida, Y., 1969, PASJ, 21, 128

[220] Uchida, Y., 1970, Astron Soc. Japan, 22, 341

[221] Ugai, M., & Tsuda, 1997, T., Plasma Phys., 17131, 337

[222] Ugarte-Urra, I., Warren, H.P. and Brooks, D.H., 2009, ApJ, 695, 642651

[223] Ugarte-Urra, I., Winebarger, A. R., & Warren, H. P. 2006, ApJ, 643, 1245

[224] Uzdensky, D. A., and Kulsrud, R. M, 2000, Phys. Plasmas, 7, 4018

[225] Vaivads, A., et al. 2004, Phys. Rev. Lett. 93, 105001

[226] Van Doorsselaere, T., Nakariakov, V. M., & Verwichte, E., 2007, A&A, 473, 959

[227] Van Doorsselaere, T., Ruderman, M.S., & Robertson, D., 2008, A&A, 485, 849

[228] Van Doorsselaere, T., Birtlill, D,C,C., & Evans, G. R., 2009, A&A, 508, 1485

[229] Vernazza, J. E., Avrett, E. H., & Loeser, R. 1981, ApJS, 45, 635

[230] Verth, G., Van Doorsselaere, T., Erdélyi, R., & Goossens, M., 2007, A&A, 475, 341

.2

[231] Verth, G., & Erdélyi, R. 2008, A&A, 486, 1015

[232] Verth, G., Erdélyi, R., & Jess, D. B., 2008, Astrophys. J. Lett., 687, L45

[233] Verwichte, E.; Nakariakov, V. M.; Ofman, L.; Deluca, E. E., 2004, Sol. Phys., 223, 77

[234] Verwichte, E., Aschwanden, M.J., Van Doorsselaere, T., Foullon, C, & Nakariakov, V. M., 2009, ApJ, 698, 397

[235] Viall, N. M., & Klimchuk, J. A. 2011, ApJ, 738, 24

[236] Volkmer, R., Kneer, F., & Bendlin, C. 1995, A&A, 304, L1

[237] Warren, H. P, Winebarger AR, and Hamilton, 2002 PS, ApJ, 579, L41

[238] Warren, H. P., Ugarte-Urra, I., Doschek, G.A. et al. 2008, ApJ, 686, 131

[239] Weiss, N. O., Brownjohn, D. P., Hurlburt, N. E., & Proctor, M. R. E. 1990, MNRAS, 245, 434

[240] Weiss, N. O. 2002, Astron. Nachr., 323, 371

[241] Wilhelm, K., 2000, A&A, 360, 351

[242] Wills-Davey, M.J., Thompson, B.J., 1999, Sol. Phys., 190, 467

[243] Winebarger, A. R., Warren, H. P., & Seaton, D.B, 2003, ApJ, 593, 1164

[244] Winebarger, A. R., & Warren, H. P. 2005, ApJ, 626, 543

[245] Yamada M, Levinton F, Pomphrey N, Budny R, Manickam J, Nagayama Y. 1994. Phys. Plasmas 1:3269

[246] Yamada, M., et al. 2006, Phys. Plasmas, 13, 052119

[247] Yeh, T., 1976, ApJ, 207, 837

[248] Yokoyama, T., & Shibata, K., 1995, Nature, 375, 42

[249] Yokoyama, T., & Shibata, K., 1996, PASJ, 48, 353

[250] Zaitsev, V.V., Stepanov, A.V., Urpo, S., Pohjolainen, S., 1998, A&A, 337, 887-896

[251] Zaqarashvili, T.V. & Erdélyi, R., 2009, Space Science Reviews, 149, 355-388

[252] Zwaan, C., 1987, ARA&A, 25, 83